Università degli Studi di Ferrara

DOTTORATO DI RICERCA IN SCIENZE DELL'INGEGNERIA
Ciclo XXV

COORDINATORE PROF. STEFANO TRILLO

Energy Harvesting Techniques for Small Scale Environmentally-Powered Electronic Systems

Dottorando
Dott. Davide Carli

Tutore
Prof. Massimiliano Ruggeri

Settore Scientifico Disciplinare ING-INF/01 – Elettronica
Anni 2010–2012

Università degli Studi di Ferrara

DOTTORATO DI RICERCA IN SCIENZE DELL'INGEGNERIA
Ciclo XXV

Coordinatore Prof. Stefano Trillo

Energy Harvesting Techniques for Small Scale Environmentally-Powered Electronic Systems

Settore Scientifico Disciplinare ING-INF/01

Dottorando
Dott. Davide Carli

Tutore
Prof. Massimiliano Ruggeri

Anni 2010–2012

Sed fugit interea, fugit inreparabile tempus,
singula dum capti circumvectamur amore.

— Publius Vergilius Maro

To Chiara, the spice of my life, and to my loving parents.

ACKNOWLEDGMENTS

The successful outcome of the Ph.D. course ending with this dissertation owes much to the guidance, help and support of many people, that I would like to acknowledge here.

Foremost, I would like to express my sincere gratitude to my advisor Massimiliano Ruggeri, for his wise supervision throughout the whole course, his valuable advices, and especially for getting me in touch with many of the people I collaborated with. Gianluca Poli and Fabio Fochi; Marco Cerigato and Elisa Iuculano; Denis Dondi, Alessandro Bertacchini and Luca Larcher; Michele Bottarelli and Massimo Mazzer: I'm very grateful to all of you for your precious support and contributions.

Furthermore, I wish to express a special thanks to Davide Brunelli and Luca Benini, who first introduced me to the world of academic research, teaching me the basics and providing me a vivid insight of the attractiveness of authentic research profession.

I would like to earnestly thank my fiancée Chiara for her love, encouragement and understanding when I have needed it the most. Thank you with all of my heart!

Finally, I owe a warm thanks to my mom and dad, for giving me their wholehearted support throughout everything.

Ferrara, March 2013. *Davide Carli*

CONTENTS

ACRONYMS

ac	alternating current
BIPV	building-integrated photovoltaic
CAN	controller area network
CMOS	complementary metal–oxide–semiconductor
COTS	commercial off-the-shelf
dc	direct current
DCM	discontinuous current mode
DSP	digital signal processor
FF DCM	fixed-frequency discontinuous current mode
FPGA	field-programmable gate array
GSHP	ground-source heat pump
HAWT	horizontal-axis wind turbine
HVAC	heating, ventilation and air conditioning
IC	integrated circuit
IGBT	insulated-gate bipolar transistor
Li-ion	lithium-ion
MEMS	micro-electro-mechanical system
MOSFET	metal-oxide-semiconductor field-effect transistor
MPP	maximum power point
MPPT	maximum power point tracking
NiMH	nickel-metal hydride
PCB	printed circuit board
PFC	power factor correction
PTO	power take-off

PV	photovoltaic
PZT	lead zirconate titanate
rf	radio-frequency
RMS	root-mean-square
SoC	system-on-chip
VAWT	vertical-axis wind turbine
WSN	wireless sensor network

INTRODUCTION

The term *energy harvesting* describes the ability of a low-power electronic system to obtain all the electrical energy it needs to operate, or part of it, directly from the surrounding environment[1].

This capability is required in an increasing number of spatially-distributed computing applications, notably in the fields of remote sensing and ubiquitous computing. These applications often require the placement of low-power electronic systems in locations where a wired connection to them is physically impossible, or would be considerably uneconomic. The absence of this connection makes necessary to find different ways to both power these systems and to communicate with them. Usually these needs result in the following requirements for the remote electronic systems: to be self-sufficient from an energetic point of view, and to be able to communicate wirelessly. While present technology provides many alternatives to fulfill the latter requisite, the most widespread solution to meet the former is to equip the system with a battery pack. It should however be noted that batteries are energy reservoirs with finite capacity: in order to keep the powered system operational for an indefinite time, periodic maintenance to recharge or replace the battery pack is required. Nevertheless, the same difficulties encountered in reaching the remote systems with cables often arise again with regard to the maintenance interventions, which can likewise prove to be highly impractical for physical or economic reasons.

It is precisely in these situations that the implementation of energy harvesting techniques can make a key contribution in enabling the self-sustainability of these remote systems. If the electronic system is capable of collecting the energy it needs directly from the surrounding environment, it can potentially achieve an unlimited operating life time. Compromise solutions are also possible: if there are no physical impediments preventing the execution of maintenance interventions, the system can collect from the environment just a portion of the overall energy it requires to operate, drawing the missing part from a battery. In this way the battery load can be heavily reduced, as well as the frequency of the required maintenance actions.

---

[1] Expressions such as *energy scavenging* or *power harvesting* can also be found in literature to convey the same concept. Nevertheless, the usage of *energy harvesting* has become prominent over time, and this is currently the most widespread form.

In a world where electronic systems are becoming more and more pervasive and untethered, and considering the increasing demand of remote sensing infrastructures to improve the monitoring and the control of novel scenarios, the implementation of energy harvesting techniques is instrumental in enabling many high business potential applications. This is undoubtedly one of the reasons for the research on this topic gaining momentum over the last decade. Similarly, the offer by many electronic components manufacturers of products and solutions expressly designed for energy harvesting applications has grown noticeably, in the same time span.

The most investigated issues in this field address in the first instance the optimization of energy harvesting systems (so-called *energy harvesters*) according chiefly to the metrics outlined below.

POWER GENERATION AND EFFICIENCY

The energy harvester must be able to collect the largest possible amount of energy from the ambient energy sources, for the widest possible range of expected operating conditions, while meeting the application requirements in terms of size and cost. This often leads to a barely positive overall energy budget: this explains why the power management circuits, besides keeping their own power consumption as low as possible, must ensure the maximum possible efficiency during the processing and the temporary storage of the harvested energy.

RELIABILITY

Considering that the ultimate goal of an energy harvester is to make an electronic system operate indefinitely, it must ensure both a high availability on the short term, and a high durability on the long one. The former is often jeopardized by the mismatch between the power generation and consumption profiles, caused by the significant and unpredictable variations peculiar of many ambient energy sources, which lead to a power outage probability greater than zero. An adequate level of local energy buffering allows to preserve the service level provided by the harvester, whereas the choice of using maintenance-free components improves its durability.

FLEXIBILITY

The design of an energy harvester is often tailored to the requisites of a specific use case. However, to boost the widespread adoption of a harvesting solution, it is best if it provides a minimum level of modularity and configurability, letting the user to set it to work in an optimal way with a certain range of transducers, of load systems, and in presence of ambient sources with various characteristics.

Furthermore, there is a strong interest in investigating the applicability of energy harvesting systems, or just of the principles and design strategies typical of this technology, to pioneering application scenarios.

During the Ph.D. research activity, we have tackled all the issues listed above, and have proposed solutions to improve the current state of the art in these respects. The specific contributions are presented and discussed in the following.

- We have designed and implemented a novel airflow energy harvester, in collaboration with the Microelectronics Research Group of the University of Bologna, with the purpose of obtaining power generation capabilities comparable to those of similar systems described in literature, but with a substantially smaller size. The power density of a number of different miniature wind generators has been measured to select the best performing transducer, and particular attention has been devoted to the optimization of the power management circuit in terms of efficiency and power saving, under the vast majority of operating conditions.

- To fulfill a collaboration request coming from the ISTEC-CNR institute and from its spin-off company IPECC, both active in the research on piezoceramic materials, we have implemented a vibrational harvester building upon the architecture of the previous system. This has proven to be very flexible in accommodating a wide range of piezoceramic transducers and vibration characteristics, while still guaranteeing the maximum power generation. Moreover, the harvester has been made fully autonomous through the addition of an expressly designed cold-booting circuit.

- As part of the EU FP7 ICT-AGRI STRATOS European research project, we have investigated the applicability of self-powered wireless sensor nodes to heavy duty and agricultural machinery, a topic seldom addressed even in recent scientific literature. The energy budget which could be reached by these devices in such environment has been analyzed, with the support of original experimental data on the vibration spectra available on the spot, and supposing to employ commercial off-the-shelf vibrational transducers.

- Since many remote monitoring applications often set strict requirements on the minimum availability of each wireless sensing node, we have designed and implemented an energy harvesting system which permits to achieve a very low outage probability. The proposed modular architecture, developed during a collaboration with the Microelectronics Research Group of the University of Bologna, can collect energy from an arbitrary number of hot-pluggable harvesting subsystems in a concurrent and independent way, allowing each subsystem to harness a different ambient source. Besides, the energy buffering capabilities of the system have been extended by means of a rechargeable battery, to provide additional protection against long periods of ambient energy shortage. A simulation framework has been expressly developed to analyze the behavior of this multi-source harvester under real-world operating conditions.

- To fulfill a collaboration request coming from the IMEM-CNR institute, active in the research on semiconductors for photovoltaic applications, we have applied the principles and design strategies typical of multi-source harvesters to design a power supply system capable of maximizing the self-consumption of locally generated photovoltaic electricity to supply a single appliance, while providing the same reliability of a conventional grid-connected power supply. In particular, we focused on ground-source heat pump systems as target appliances, and thus investigated the effectiveness of the proposed design through the analysis of original data on the typical power consumption of these systems, obtained by means of a simulation framework provided by the Department of Architecture of the University of Ferrara.

The remainder of the dissertation is organized as follows. The first Part collects the Chapters dealing with harvesters harnessing a single energy source. Chapter 1 gives an overview about energy harvesting systems, illustrating their principal features and the key design challenges still open. The airflow energy harvester developed in the first part of my research activity is presented in Chapter 2. With an overall volume of just $300\,\mathrm{cm}^3$, it features a miniature horizontal-axis turbine, and a clever control circuit cutting down power consumption in absence of airflow. This architecture lays the foundations of the vibrational energy harvester described in Chapter 3, introducing an original cold-booting circuit to achieve full autonomy. The analysis on energy harvesting from vibrations continues in Chapter 4, which presents attractive results on the applicability of vibrational harvesters to power wireless sensor nodes placed on-board agricultural machinery. The Chapters belonging to the second Part discuss instead systems with multiple energy sources as input. Chapter 5 tackles the problem of collecting energy from multiple harvesting subsystems at the same time, and illustrates the design of a scalable multi-source architecture for applications with strict availability requirements. The application of classic energy harvesting design principles to larger scale systems leads to the grid-assisted photovoltaic power supply proposed in Chapter 6, expressly designed to improve the self-sustainability of ground-source heat pumps. Finally, conclusions are drawn, reporting the main research contributions that have been discussed throughout this dissertation.

1 ENERGY HARVESTING — AN OVERVIEW

The increasing availability of computing and sensing solutions based on miniature, very low power electronic devices has played an instrumental role in the rise of a steadily growing number of remote sensing applications. The coming decade will see the rapid diffusion of distributed standalone embedded systems, where devices are required to operate unattended for decades, and users should just *deploy and forget* about them.

However, the demand for more and more pervasive sensing systems, to be deployed in hardly reachable locations (sometimes even embedded inside solid structures), comes up against the problems affecting conventional battery-based supply strategies, which require periodic maintenance: limited lifetime, self-discharge, limited number of recharge cycles, and long-term environmental impact. The need for completely autonomous systems to employ in such high-market-potential application areas has fostered research activity on alternative power supply solutions, and in recent years *energy harvesting* has been acknowledged as one of the most promising technologies to achieve this goal.

Underlying energy harvesting techniques is the idea of obtaining the energy needed to power an electronic device directly from its operating environment, through the conversion of some form of ambient energy to electrical energy.

The first markets for this technology are applications where direct energy supply from the power grid is not possible (or would be strongly limiting for the application) and the periodic replacement of batteries would be too expensive, such as building and home automation, military and avionic devices, communication and location devices. Harvesting will facilitate the diffusion of sensing solutions based on small, low-power embedded systems, such as wireless sensor networks [1, 2]. In these situations, relying on energy sources freely provided by the operating environment and available on the spot is highly desirable.

1.1 AMBIENT ENERGY SOURCES

Depending on the operating environment and on the application scenario, different energy sources can be available, and different energy conversion techniques can be adopted to harness them. For example, considering wearable applications, body heat, vibrations and human movement can be appropriate for the purpose [3], whereas sunlight and wind can provide enough energy for almost all outdoor applications [4]. Every energy source has distinctive characteristics in terms of controllability, predictability and magnitude: all these factors are relevant for the choice of the most suited source for a certain application [5]. In particular, the magnitude can be expressed in terms of harvestable power surface density, i.e. the harvestable power per unit of area of the harvesting device. A tabular comparison of different energy harvesting methods on the basis of this parameter can be found, for instance, in [6].

1.2 HARVESTING SYSTEMS ARCHITECTURE

Energy harvesters can usually be modeled with the diagram shown in Figure 1.

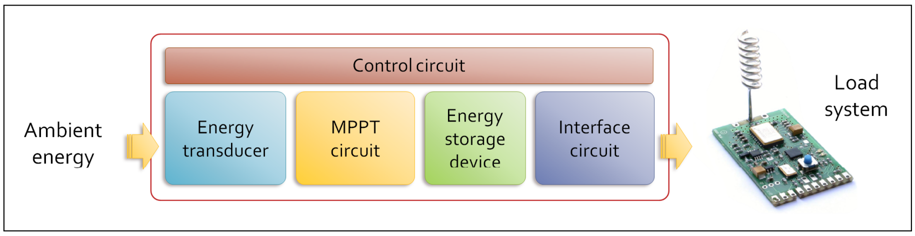

Figure 1. Typical architecture of a standalone energy harvesting system.

ENERGY TRANSDUCER
A device performing the conversion from a particular kind of ambient energy (kinetic, electromagnetic, thermal, etc.) to electrical energy.

MAXIMUM-POWER-POINT TRACKING (MPPT) CIRCUIT
A circuit which adjusts dynamically the operational parameters of the conversion device in response to the variations of the available energy level, in order to let it convert the maximum possible amount of power in every condition. At the same time, it transfers the harvested energy to the energy storage device.

ENERGY STORAGE DEVICE
A device which stores the generated electrical energy, and act as an energy buffer between the ambient source and the load system.

INTERFACE CIRCUIT
A circuit providing a stable, regulated and (as long as possible) uninterrupted voltage to the electronic system to be supplied, to ensure its correct operation.

CONTROL CIRCUIT
A circuit which supervises the operation of each subcircuit, and manages the transitions between operating modes.

1.3 DESIGN CHALLENGES

An energy harvester can be considered as an interface between one or several energy suppliers (the renewable ambient energy sources) and one or several energy consumers or loads, i.e. the systems to be powered. The real challenge in the design of energy harvesting systems is to provide a continuous and stable power supply to the load in spite of the adverse availability characteristics of the energy sources, while keeping at the same time the harvester size and cost as low as possible.

1.3.1 Power generation and efficiency

Energy density, efficiency, size and cost of the harvester are the primary design metrics to compare each solution. In fact, to satisfy the power needs of the embedded system while keeping the harvesting device as small as possible, the optimization of the harvesting process becomes crucial.

Another critical issue is to address the variability of environmental energy sources. Indeed, for every input energy level, the electrical load of the harvesting device which maximizes the generated power can in general be different. The direct connection of the harvesting device to the energy storage device often does not provide the maximum harvesting efficiency, therefore the harvesting system should continually perform a maximum power point tracking (MPPT), by adjusting the operating point (i.e. the impedance measured at the harvesting device output terminals) to maximize the power generation at every working condition. The design of the MPPT circuit requires the characterization of the harvesting device output impedance for different input energy levels and the choice of the technique to modify the load shown at its terminals. The MPPT algorithm, then, can be implemented in hardware, through an expressly designed analogue circuit, or executed as a piece of software by a microcontroller or a digital signal processor (DSP).

Furthermore, the power conversion and transfer from the energy transducer to the load system should be performed with the maximum efficiency and the least possible power overhead in most conditions, through the optimization of each power processing block and of the whole architecture. In particular, the circuits which convey the power from a section of the system to another one (e.g. dc/dc converters) should lose the least possible amount of energy during the transfer, and the power consumption of the control circuitry should be negligible when compared to the power delivered to the load.

1.3.2 Reliability

The harvesting system should comprise a properly sized energy storage device, working as a buffer between the variable power consumption of the load system and the wide dynamic range and discontinuous nature of the ambient source, without the need for periodic maintenance. This requires the harvester to store the collected energy in devices working as energy reservoirs, to be filled as much as possible when the ambient sources are available and to be slowly emptied to power the load when they are not.

Different devices can be used for storing the harvested energy: supercapacitors and rechargeable batteries are the typical options. The choice should consider the estimated power budget of the whole system (given by the power requirements of the embedded system, the characteristics of the exploited energy source and the efficiency of the harvesting system) against the desired level of service continuity.

The absence of predefined charge and discharge profiles and thus their higher power density, the possibility of precisely estimating the state-of-charge from the voltage across them, and their high maximum recharging cycle life time, make the supercapacitors the best choice for this task [7]. However, when compared to batteries, they still provide a much lower energy density: this can be a limiting factor if the harvester is expected to continue powering the load even during long periods of ambient energy shortage, or if maximum operational reliability is required. The adoption of batteries comes at the cost of additional circuitry, to protect them from overcharging or undercharging.

1.3.3 Flexibility

Several aspects must be taken into account for the design of an energy harvester: the load system average power consumption, the desired level of service continuity, possible constraints on size and cost, the typical availability level and magnitude of the relevant energy source at the expected deployment place, etc. As a consequence, the application strongly affects the design choices: however, in order to reduce as much as possible the design effort for systems to be employed in similar applications, the harvester should be designed with some degree of flexibility and modularity, allowing for slight changes of some of its parts or in its operating conditions.

Part I

SINGLE-SOURCE HARVESTING SYSTEMS

2 AIRFLOW ENERGY HARVESTER

2.1 INTRODUCTION

This chapter focuses on airflow as a feasible energy source to meet the energy needs of a small autonomous embedded system. A novel wind energy harvester is presented, featuring an overall volume smaller than $300\,\mathrm{cm}^3$. It consists of a small turbine-based wind generator and a highly efficient maximum power point tracking (MPPT) circuit, based upon a dc/dc buck-boost converter expressly designed for the purpose. The generated energy is stored in a supercapacitor and an additional buck-boost converter is used to provide a constant dc output voltage. This harvester has been designed as a module of the multi-source energy harvester described in Chapter 5 on page 77, so the analogue control circuitry of the harvester has been thought to be powered by a secondary battery with 3.6 V nominal voltage. Experimental results show that the wind generator boosts efficiency over a wide range of operating conditions.

The remainder of the chapter is organized as follows. In the next Section 2.2 we review the related works, whereas Section 2.3 lists the contributions and innovations that this work proposes. The description of the chosen wind generator, its characterization and modeling, and its performance are reported in Section 2.4. The MPPT circuit is the subject of Section 2.5, which details the design process we followed to optimize the efficiency of the buck-boost converter and presents the architecture of the control circuit. Section 2.6 illustrates the testing procedure of the implemented harvester and shows the experimental results thus obtained, which prove to be very adherent to those expected on the basis of computer simulations. Finally, Section 2.7 concludes the chapter.

2.2 RELATED WORKS

Although the design of self-powered embedded systems is a recent challenge, the research activity in this area is very active and several harvesters using various environmental sources have been proposed. For example, [8] reviews the latest progress in kinetic energy harvesting for wearable and mobile applications, [9] designs integrated microgenerators exploiting micro-electro-mechanical systems (MEMSs), whereas [10] presents a compact and wearable photovoltaic scavenger for indoor applications.

2.2.1 Wind energy harvesting

Small scale wind energy harvesting is still quite unexplored and few wind-flow harvesters with a size in the order of 1 dm^3 have been presented in literature, even though research in this field can leverage on the experience in designing energy generators with large and medium turbines, which is almost consolidated [11]. First prototypes were proposed in [12], where piezoelectric bimorphs elements are used to generate electricity through the rotation of three horizontal-axis wind turbines with a diameter of 12.7 cm each. Although they partially overlap, the whole system occupies a volume greater than $25\,\mathrm{cm} \times 18\,\mathrm{cm} \times 7\,\mathrm{cm}$. The authors state that it can generate continuously 5 mW with an average wind speed of 16.1 km/h, and that the cut-in speed of the windmill is of about 8.7 km/h. The energy density in [12] is lower in comparison with the results presented in this work. The authors of [13] try instead to extend the battery life in a wind speed sensing application exploiting the same cup anemometer used to perform the measurements, connecting to its shaft an axial-flux brushless generator. The two round plates making up the latter have a diameter of 7.6 cm, while the cup anemometer is probably larger. Also at high speed winds (more than 30 km/h) the generated power remains below 1 mW. This poor result is mainly due to the low efficiency of the cup anemometer as a wind generator.

Ambimax [14] is a multi-source energy harvester equipped with a wind energy harvesting subsystem. Its authors employ a commercial off-the-shelf (COTS) wind turbine, called Windlab Junior [15]. This horizontal-axis turbine-based generator is 38.5 cm high, 38.5 cm wide and 21 cm deep, and is capable of generating 0.5 W at 2000 rpm; from the paper it can be deduced that it is expected to generate 200 mW with a wind speed of 36 km/h. This considerable power level is probably due to the large area swept by the relatively long blades and to the favorable test conditions. However, the optimization of the efficiency of the wind energy harvesting subsystem is not thoroughly addressed in this work.

Another multi-source harvesting solution featuring a small-sized wind generator is the one presented in [16]. This system exploits a Savonius wind turbine with a swept area of 120 cm^2, capable of generating about 36 mW at a wind speed of 16.8 km/h, in maximum power point (MPP) conditions.

Finally, an interesting commercial wind harvesting solution is microWindbelt [17] by Humdinger. This wind generator bases its functioning on the aeroelastic flutter principle, instead of using a turbine: this allows the whole system to be very small, with a size of just 13 cm × 3 cm × 2.5 cm. At the generator terminals, before the ac/dc power conditioning stage, power levels of 0.2 mW and 2 mW have been measured with wind speeds of 12.6 km/h and 19.8 km/h, respectively. Although the losses due to the following power stage are not included, these power levels are rather relevant though, if we take into account the very small size of the device. The cut-in speed of microWindbelt is 10.8 km/h.

2.2.2 Maximum-power-point tracking

With specific regard to the design methodology, there are several works dealing with the problem of maximizing the power generated by a harvesting device through the optimization of each stage of the circuit. Modeling the energy generator is one of the most difficult steps and it is important for any kind of environmental energy transducer. For example, the authors of [18] achieved vibrational energy harvesting with very low power dissipation starting from a small-deflection model of the vibrating piezoelectric cantilever. In the same way, [19] presented a compact and accurate model of small-size photovoltaic cells to maximize the efficiency of solar harvesters for self-powered systems. The model allowed the authors to propose a design methodology for scavenging circuits.

Maximum power point trackers and dc/dc circuits are also very important optimization targets. Much effort has been invested in dynamically matching the impedance at the generator output, to maximize the energy converted with minimum energy loss. The work [20] has been one of the firsts to address this issue. It proposes to implement the MPPT through a dc/dc switching converter operating in fixed-frequency discontinuous current mode (FF DCM), and a control circuit capable of varying some of the converter parameters. In this way it is possible to adjust the converter input resistance, setting its value as a function of the power level generated by the harvesting device. Whereas in this work the authors use a DSP-based power greedy control circuit to track the MPP and change the input resistance, in a following paper [21] they manage to obtain the same functionalities with a lower-consumption dedicated analogue circuit.

In some favorable cases, the output resistance of the harvesting device does not change significantly when the environmental power level varies, so a fixed load resistance is sufficient to achieve the impedance matching in every condition. This enables an additional simplification of the converter control circuit, which does not have to track the MPP and requires one-time calibration. This situation characterizes works [22–25], and will be encountered in the present work as well.

In particular, [22] contains a brief survey of the suitability of different converter topologies (buck-boost, boost, and buck) to achieve the desired matching. This work highlights how the boost (or buck) converter operating in FF DCM is valuable only when the input voltage is much smaller (larger) than the output voltage, whereas the buck-boost converter can provide true resistor emulation independently of the input and output voltage. Therefore, the choice of the most suitable converter topology depends on the voltage characteristic of the particular application. In [23, 25], e.g., a buck-boost converter is selected, whereas in [20, 21] a buck converter is used. In [22] a comparison between the boost and the buck-boost topologies is also performed.

2.3 CONTRIBUTIONS

The aim of the work presented in this chapter is to develop a very-small-size wind energy harvester providing a highly effective solution to collect freely available wind power. To achieve this goal, this chapter presents the following contributions.

- We thoroughly characterize and model the wind generator performance, to identify the conditions which maximize power generation. The selected turbine can generate up to 10 mW with a wind speed of 16 km/h, despite having a smaller size than [12] and [13]. The cut-in speed is lower than 8.6 km/h.

- We expressly design and optimize a buck-boost converter based MPPT circuit, to emulate at the wind generator output the resistive load which maximizes its performance. The adopted design methodology enhances the solution proposed by [22] and is aimed to the minimization of the power losses of the operating devices. After the selection of the components with the most suitable characteristics to build the converter, the values of other converter parameters are chosen through extensive computer simulations and the comparison of the resulting efficiency plots. This procedure allows to make the best design choices on the basis of the expected operating conditions of the harvester.

- The architecture of the circuit controlling the converter operation is carefully designed to minimize the power consumption as well, while using COTS components. An ultra-low-power comparator is used to disconnect the oscillator circut from the power supply when the wind is absent, avoiding the converter to continue switching when it is not needed.
- The results of the tests carried out on the implemented harvester attest the effectiveness of the applied design methodology, as they are very similar to those obtained through the numerical simulations. The measured efficiency of the converter is always greater than 81 % for output voltages above 0.8 V, with peaks of 87 %.

2.4 WIND GENERATORS CHARACTERIZATION

With the expression *turbine-based wind generator* we identify a device capable of converting the kinetic energy of an airflow into electrical energy by means of a turbine. We focused on the permanent-magnet version, the most suitable for low power levels. The characteristics of both the electrical generator and the mechanical turbine play an important role in determining the wind generator overall performance, in terms of efficiency, reliability and cost.

For micro-size systems as the one we present, we considered basically two types of wind turbines, namely *horizontal-axis* and *vertical-axis* generators. Horizontal-axis wind turbines (HAWTs) are generally more efficient than vertical-axis wind turbines (VAWTs), nevertheless VAWTs are simpler and can be found with several rotor designs (e.g. Darrieus, Savonius, . . .). Savonius rotors, for example, present some advantages over HAWTs, such as they do not need to move on the horizontal plane when the wind shifts.

2.4.1 Savonius generators

In the first instance, we investigated the suitability of small Savonius turbines (like the one displayed in Figure 2a) for our purpose. We used a little three-phase motor as electrical generator (Figure 2b), and a three-phase rectifier bridge with Schottky diodes to get a dc voltage from the ac waveforms (Figure 2c). Then we tested their perfor-

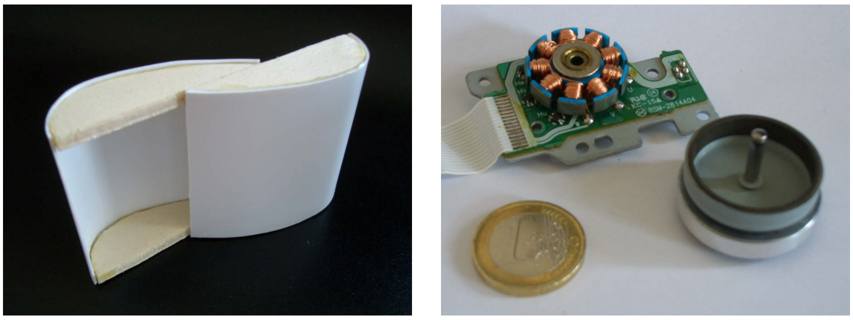

(a) Plastic Savonius turbine **(b)** Disassembled motor

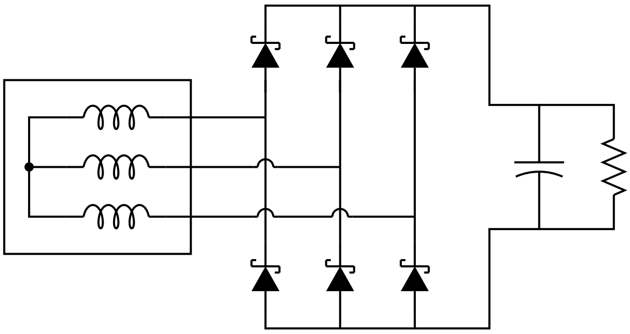

(c) Rectifier circuit

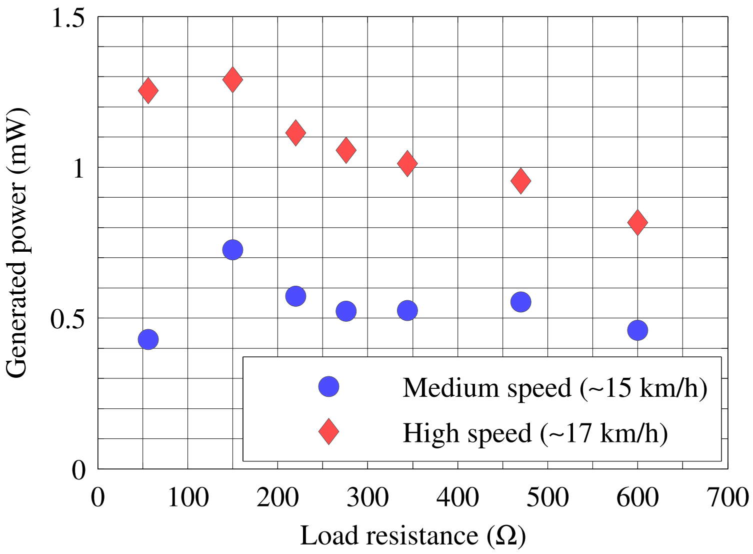

(d) Test results

Figure 2. On the first row: the self-built small vertical-axis wind turbine, and the inrunner brushless generator coupled with it. On the second row: the three-phase bridge rectifier employed to obtain a dc voltage from the ac waveform provided by the generator. On the third row: outcome of the tests executed on a self-built vertical-axis wind turbine with a size below 1 dm^3. A maximum power of about 1.3 mW has been obtained, with an airflow speed of 17 km/h.

mance as wind generators at different wind flow speeds, varying several times the resistive load at the rectifier output.

The results of the tests are reported in Figure 2d. As the plot shows clearly, we managed to obtain an output power of 1.3 mW with an airflow speed of about 17 km/h. Moreover, the condition for the maximization of the generated power seems to be the presence of a load of about 150 Ω at the output of the rectifier.

2.4.2 Horizontal-axis wind turbine

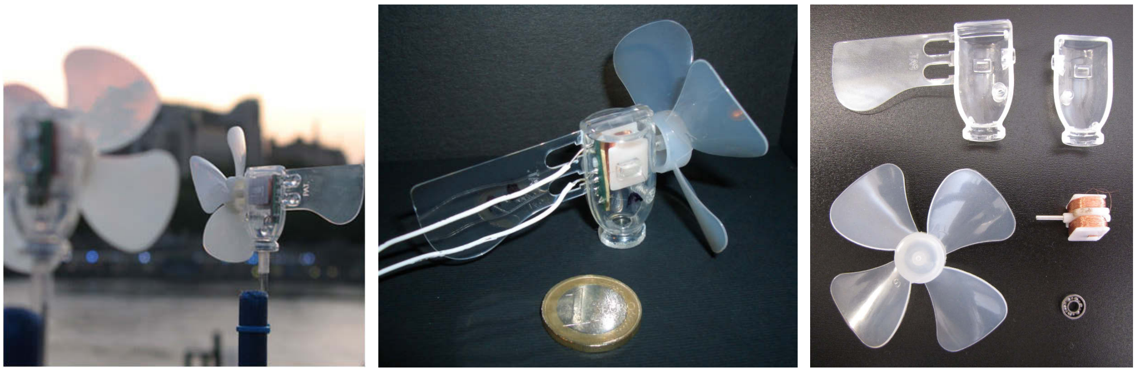
(a) Deployment example **(b)** Close-up **(c)** Disassembled view

Figure 3. The miniature four-blade plastic horizontal-axis wind turbine tested during the turbine selection phase of the harvester design.

Afterwards, we focused on a HAWT model, a four-blade plastic turbine with a diameter of just 6.3 cm, shown in Figure 3. The generator is composed of a single-phase coil, which encloses the magnets integral with the rotating shaft attached to the turbine.

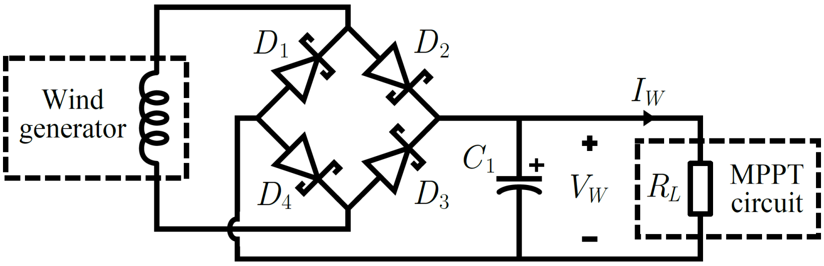

Figure 4. Circuit diagram of the single-phase full-wave rectifier used to convert the wind generator output voltage from ac to dc.

The circuit used to convert the generated ac supply voltage to a dc voltage is a typical single-phase full-wave rectifier, with a diode bridge followed by a filter capacitor (Figure 4). BAT47 Schottky diodes have been selected for the bridge, in order to minimize voltage drop and power losses. The filter capacitor value (220 µF) is the result of a tradeoff between the minimization of the voltage ripple and the ability of the output voltage to follow closely enough the wind speed variations. This last requirement is important if one wants to use the rectifier output voltage as the feedback signal for the MPPT circuit: the latter should modify its operation according to actual environmental energy level, so a delay in the feedback chain is undesirable.

For the characterization of the wind generator we used three airflow speeds as reported in the second column of Table 1. The measurements, made at the rectifier output port, take automatically into account the power losses caused by the diode bridge, and their variations in response to different input power levels.

Table 1. Data regarding the characterization and modeling of the wind turbine used for our harvester.

Cases	Airflow speed (km/h)	$P_{W,\max}$ (mW)	$p_1 = R_{L,\text{opt}}$ (V/A = Ω)	p_2 (V)
Low speed	8.6	2.02	715	2.40
Medium speed	15.1	7.93	559	4.21
High speed	16.8	9.95	549	4.68

The outcome of the measurements on the HAWT model is displayed in Figure 5. This plot reports the experimental samples of the wind generator V-I characteristics, parametrized by the level of input power which depends on the airflow speed. Generally, for a fixed airflow speed, there is a load value that maximizes the power supplied by the wind generator. Notice that with an airflow speed of about 17 km/h, it's possible to generate up to about 9.7 mW: this power level is well above those obtained by [12, 13]. To summarize, the HAWT model can generate up to 7 times more power with respect to the vertical one we built, using the same wind speed. Thus we continued the design of the harvester considering this model of turbine.

The results we have obtained with this generator, first disclosed in [C1], have been taken into account in a later independent review article, which has compared them to the performance of other airflow generators in literature [26]. The comparison outcome is reported in Figure 6. It can be observed that our generator performance in terms of power density (power per unit cross-sectional area) is among the best ones, with an efficiency C_P very close to the best-performing turbine based device ([27], $C_P = 0.1$). Efficiency C_P is defined as $C_P = P_0/P_\text{r}$,

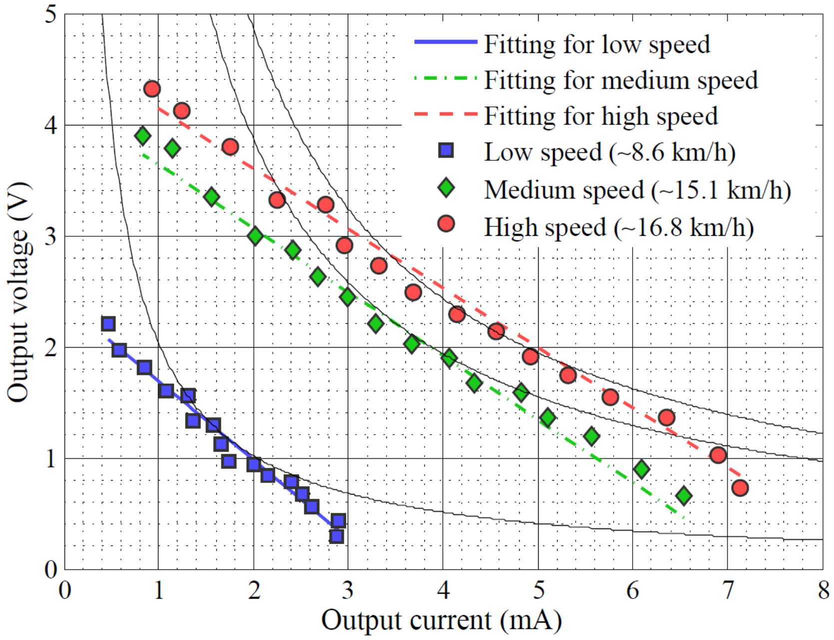

Figure 5. The data obtained from the characterization of the HAWT displayed on a V_W-I_W plot, together with the fitting curves resulting from the proposed analytic model. The solid black curves represent constant power levels: from left to right, the power levels associated to the three curves are 2.02 mW, 7.93 mW, and 9.95 mW (see Table 1).

where P_0 is the available power of the airflow hitting the cross-sectional area, whereas P_r is the electric power generated by the device (and subtracted to the airflow). It can be shown that a maximum value $C_P = 0.593$ exists, which takes the name of *Betz limit* [28]. However, the comparison in Figure 6 is not completely fair, because the same graph reports both the performance of generators comprising a rectifier circuit (like ours), and those of generators with a not-yet-rectified, ac output voltage (like [26]). This means that the actual efficiency C_P of our generator is higher than the one plotted in Figure 6, because it should not be calculated using the P_W power values listed in Table 1 (which take into account the power losses of the rectifier). It should be calculated instead from P_r power values taken directly at the ends of the brushless generator, in absence of a rectifier circuit.

Focusing back on Figure 5, the rectilinear position of the three groups of data points on this plot suggests the possibility of modeling the generator behavior at a fixed input power level with a linear model of the following type:

$$V_W = -p_1 I_W + p_2 \,, \tag{1}$$

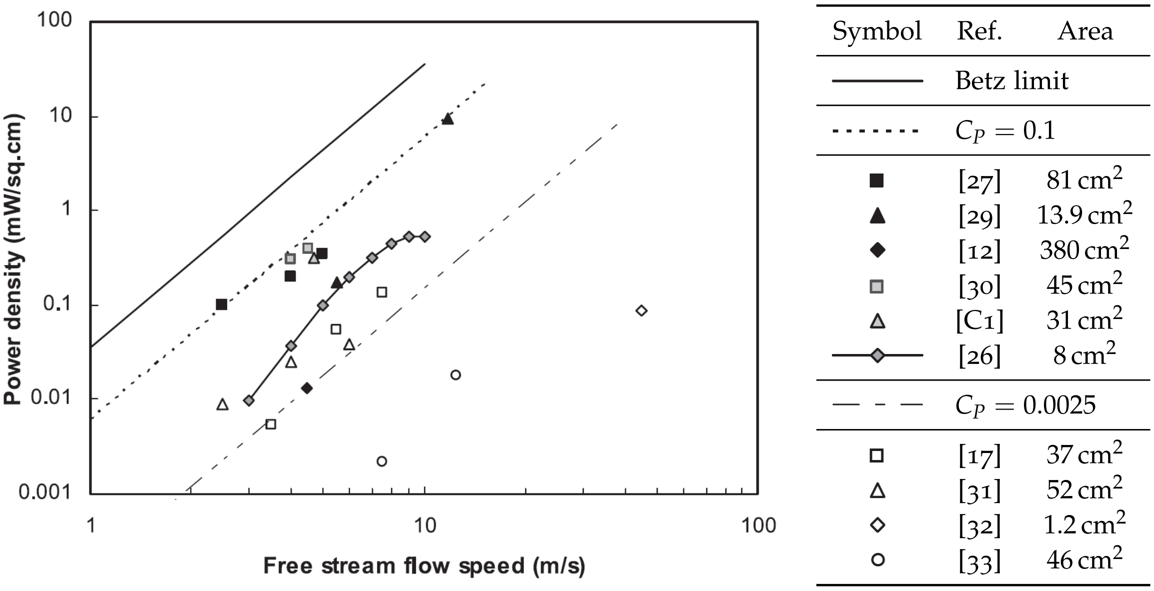

Figure 6. Performance comparison for airflow generators reported in the literature, plotted as electrical output power per unit cross-sectional area as a function of free stream flow speed. Both turbine-based (solid symbols) and non-turbine (open symbols) designs are included. In all cases the area used is the entire cross-sectional area presented to the flow. Source: [26].

where V_W and I_W are the output voltage and current of the wind generator, whereas p_1 and p_2 are two fitting parameters whose values are dependent on the input power level, hence on the wind speed. After performing a least mean squares fitting, we obtain the values reported in Table 1 for parameters p_1 and p_2 and the lines in Figure 5, superimposed on the experimental data points.

Now, it's possible to use the model to get a better estimate of the resistance value which optimizes the power generation at a fixed airflow speed. Knowing that the output power is given by $P_W = V_W I_W$ and using Equation (1), we obtain that:

$$P_W = -p_1 I_W^2 + p_2 I_W \,. \tag{2}$$

Differentiating the previous equation it's easy to determine the current value which maximizes the output power, and consequently the expression of the maximum achievable power:

$$I_{W,\mathrm{opt}} = \frac{p_2}{2\,p_1}\,; \tag{3}$$

$$P_{W,\max} = P_W(I_{W,\mathrm{opt}}) = \frac{p_2^2}{4\,p_1}\,. \tag{4}$$

Hence the load value which optimizes the power generation is:

$$R_{L,\mathrm{opt}} = \frac{P_{W,\mathrm{max}}}{I^2_{W,\mathrm{opt}}} = p_1\,. \tag{5}$$

Another interesting result synthetically describing the dependence of the generated power on the ambient energy level (through p_1 and p_2 values) and the load resistance can be found putting Equation (2) in a system with $P_W = R_L\, I_W^2$:

$$P_W = \frac{R_L\, p_2^2}{(R_L + p_1)^2}\,. \tag{6}$$

Table 1 reports the values of $P_{W,\mathrm{max}}$ and $R_{L,\mathrm{opt}}$ corresponding to the a wind flow speeds used to characterize the turbine. It is immediate to observe that the optimal load resistance value lies between $549\,\Omega$ and $715\,\Omega$ for all the tested airflow speeds. The narrowness of this range implies that, if a fixed load resistance value is chosen within this range, the the power generated for any input power level will be close to the maximum one.

The choice of the exact value for the load resistance is based on which operating condition one wants to optimize. The trend noticeable in Table 1 is a slight decrease in $R_{L,\mathrm{opt}}$ when the airflow speed increases: considering that our characterization stops at an airflow speed corresponding to a "gentle breeze" in the Beaufort scale [28], we expect the $R_{L,\mathrm{opt}}$ value to further decrease at higher wind speeds. Our tradeoff choice is thus a resistance value of $550\,\Omega$ for the load of the rectifier: it allows the generation of nearly the maximum possible power with light winds (which are also the most frequent ones) without penalizing too much the harvesting at higher wind speeds.

2.5 MPPT CIRCUIT

Considering the model of the wind turbine used in our harvester, the condition which maximizes the power supplied by the wind generator (rectifier included) is approximated assuming the presence of a fixed load resistance of about $550\,\Omega$. The transfer of the energy to the selected storage device is independent on the level of energy already stored into it.

Note that in such case there is no real "tracking" of the maximum power point, because the condition for the maximization of the generated power is only slightly dependent on the input power level. This particularity brings some advantages. In the first place, the absence

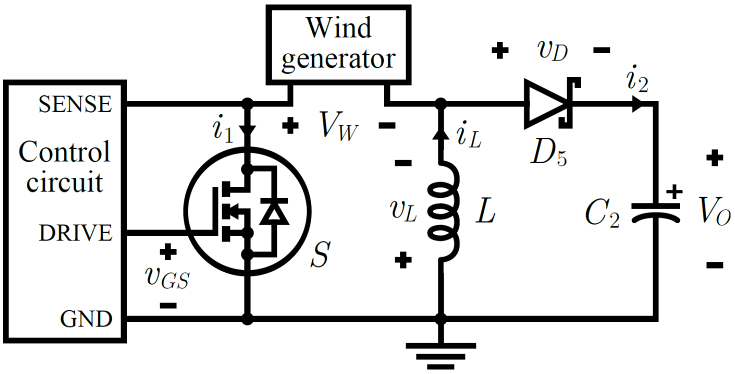

Figure 7. Circuit diagram of the considered buck-boost converter.

of feedback control circuitry reduces the system complexity and the implementation costs. Moreover, this means no additional power consumption too. If a more sophisticated MPPT circuit, able to modify precisely its input resistance in response to operating conditions variations, were employed, it would consume more power than that earned thanks to its more accurate form of tracking (with respect to the approximate condition we have chosen). Indeed, even if we consider the case of worst mismatch between $R_{L,\text{opt}}$ and the chosen value of 500 Ω (happening with the lowest airflow speed, see Table 1), the power lost because of the mismatch is just the 2 % of the $P_{W,\max}$ value, quantifiable in 40 µW. The power consumption of a more sophisticated MPPT circuit would hardly be below this power level.

In Section 2.2 we reviewed some works dealing with the emulation of a constant resistance. They all adopt a dc/dc converter operated in fixed-frequency discontinuous current mode (FF DCM), and this solution seems suitable to our case as well. In our context, both input and output voltages can reach about the same level. The converter input voltage is the output voltage of the rectifier, which can be of some volts as soon as the wind strengthens, whereas the converter output voltage is the voltage across the supercapacitor, which can range from 0 V to 5 V according to the amount of energy already stored. For these reasons, we have chosen to employ a buck-boost converter operated in FF DCM to satisfy the condition for the maximization of the power supplied by the wind generator.

2.5.1 Buck-boost converter

The circuit diagram of the considered buck-boost converter is shown in Figure 7. The qualitative waveforms of all relevant electrical quantities

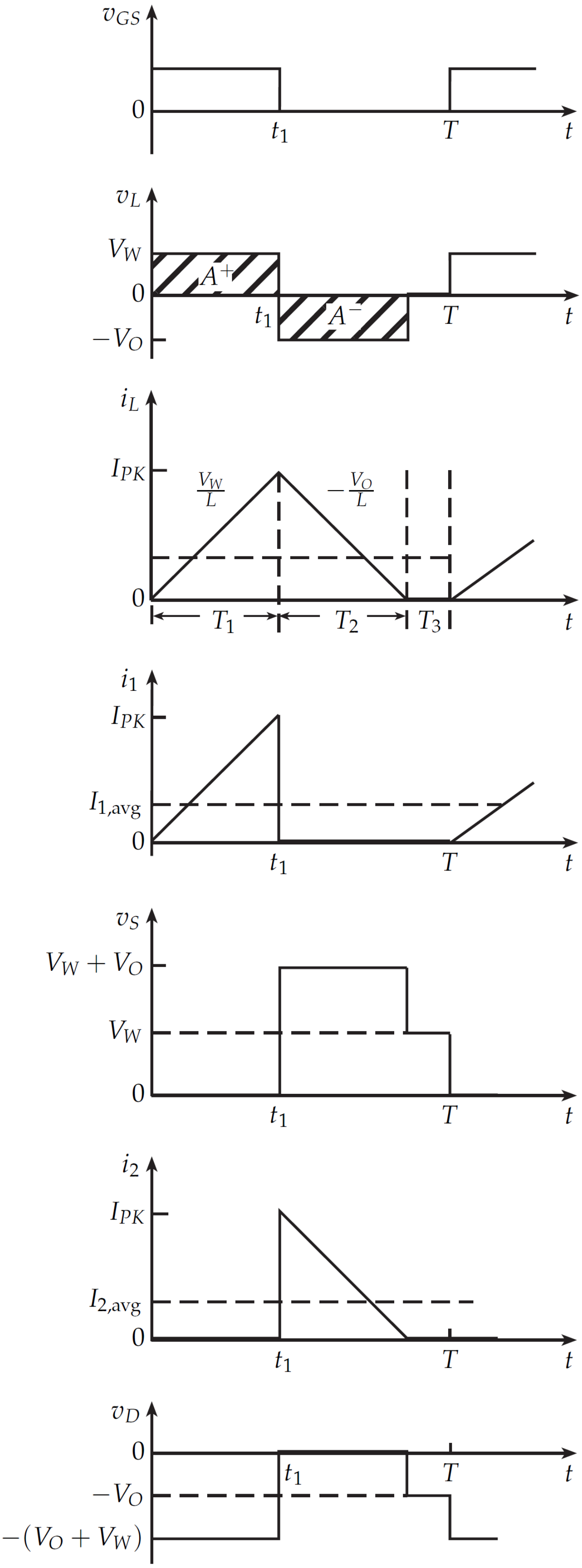

Figure 8. Qualitative waveforms of all relevant electrical quantities of the dc/dc buck-boost converter shown in Figure 7, when operating in fixed-frequency discontinuous current mode (FF DCM).

of the converter operating in FF DCM are reported in Figure 8. For a thorough investigation of converter operation in this mode, see [34].

Referring to Figure 8, T_1 is the time interval in which the metal-oxide-semiconductor field-effect transistor (MOSFET) is in conduction, T_2 is the time it takes to the inductor to transfer all the energy stored during T_1 to the supercapacitor while the MOSFET is off, and T_3 is the remaining time before the start of the next period. The overall period length is denoted by T.

Modeling the MOSFET and the diode as ideal switches and integrating the basic relation $v_L = L\frac{di_L}{dt}$ regarding the converter inductor, it's possible to obtain the following expression for the peak current in the inductor:

$$I_{PK} = \frac{V_W}{L} T_1 = \frac{V_O}{L} T_2 \, . \tag{7}$$

The waveform of the current i_1, drawn from the rectifier at the end of the wind generator, is equal to that of i_L during T_1, but it's zero during the intervals T_2 and T_3. The expression of its average value is then:

$$I_{1,\mathrm{avg}} = \langle i_1(t) \rangle_T = \frac{1}{T} \int_{t_0}^{t_0+T} i_1(\tau)\, \mathrm{d}\tau = \frac{T_1 I_{PK}}{2T} \, . \tag{8}$$

The average power entering the converter is given by $P_{IN,\mathrm{avg}} = V_W I_{1,\mathrm{avg}}$. Utilizing Equations (7) and (8), this formula can be rewritten as follows:

$$P_{IN,\mathrm{avg}} = V_W \left[\frac{T_1}{2T} \left(\frac{V_W}{L} T_1 \right) \right] = V_W^2 \left(\frac{T_1^2}{2\,L\,T} \right) . \tag{9}$$

Indicating with $R_{IN,\mathrm{eq}}$ the equivalent input resistance of the converter, this quantity verifies the equation:

$$P_{IN,\mathrm{avg}} = \frac{V_W^2}{R_{IN,\mathrm{eq}}} \, ; \tag{10}$$

from the comparison of this expression with Equation (9), it's immediate to obtain:

$$R_{IN,\mathrm{eq}} = \frac{2\,L\,T}{T_1^2} \, . \tag{11}$$

We have demonstrated that the buck-boost converter operating in FF DCM shows a fixed average input equivalent resistance, only dependent on the inductance value and on two time parameters which wholly characterize the waveform of the gate drive signal. This feature is illustrated also by classic textbooks on power electronics, as [35], as well as by [22, 23].

Design for maximum efficiency

The possibility of choosing the values of L, T_1, and T corresponds to having three degrees of freedom. However, there is only the following relationship to satisfy:

$$R_{IN,\mathrm{eq}} = R_{L,\mathrm{opt}} = 550\,\Omega\,; \tag{12}$$

this implies that two of these parameters can be arbitrarily set by the designer. A good way to take advantage of this possibility is to choose for L, T_1, and T the values which minimize the power losses due to the components comprising the converter, thus maximizing its efficiency. This approach is used also by [22].

To evaluate the conduction losses of the MOSFET, the inductor, and the diode, and the switching losses of the MOSFET, respectively, the following equations can be used:

$$P_{S,\mathrm{cond}} = R_{\mathrm{on}}\, I_{1,\mathrm{rms}}^2 = R_{\mathrm{on}}\, I_{PK}^2 \left(\frac{T_1}{3\,T}\right) \tag{13}$$

$$P_{L,\mathrm{cond}} = R_{\mathrm{esr}}\, I_{L,\mathrm{rms}}^2 = R_{\mathrm{esr}}\, I_{PK}^2 \left(\frac{T_1 + T_2}{3\,T}\right) \tag{14}$$

$$P_{D,\mathrm{cond}} = \frac{n\, V_t\, L\, I_{PK}^2}{2\,T\, V_O} \left[\ln\left(\frac{I_{PK}}{I_S}\right) - \frac{1}{2}\right] \tag{15}$$

$$P_{S,\mathrm{sw}} = \frac{1}{T}\, C_{\mathrm{oss}} \frac{V_W^2}{2} \tag{16}$$

where R_{on} is the drain-source on-state resistance of the n-channel MOSFET, R_{esr} is the parasitic equivalent series resistance of the inductor, n is the ideality factor of the diode, V_t is the thermal voltage, I_S is the reverse bias saturation current of the diode, and C_{oss} is the MOSFET output capacitance. The expression indicated for $P_{D,\mathrm{cond}}$ has been obtained considering the waveform of the current through the diode (see Figure 8 during the time interval T_2) and the consequent waveform of the forward voltage, given by the classic Shockley equation $v_D(t) = n\, V_t \ln\left(\frac{i_D(t)}{I_S} + 1\right)$; some terms have then been neglected because $I_S \ll I_{PK}$. The full derivation of Equation (15) is detailed in Appendix A.

Note that in the expression of the MOSFET switching losses $P_{S,\mathrm{sw}}$, the power consumed by the MOSFET driving circuit to charge the gate capacitance at every cycle hasn't been included. Indeed this power is provided by the secondary battery and not by the converter input port, so it's not relevant to the conversion efficiency we are considering.

As Equations (13) to (16) shows, the losses depend on the three parameters we must choose as well as on quantities characterizing the used components. Hence, also the devices must be selected carefully

Table 2. Relevant electrical characteristics of the components selected to implement the buck-boost converter.

Component	Features
n-channel MOSFET	$R_{\mathrm{on}} = 65\,\mathrm{m\Omega}$ at $V_{GS} = 3.6\,\mathrm{V}$, $I_D = 2\,\mathrm{A}$ $Q_{\mathrm{g}} = 2.4\,\mathrm{nC}$ at $V_{GS} = 3.6\,\mathrm{V}$, $I_D = 4\,\mathrm{A}$ $C_{\mathrm{oss}} = 80\,\mathrm{pC}$ at $V_{GS} = 0\,\mathrm{V}$, $V_{DS} = 6\,\mathrm{V}$
Schottky diode	$V_D = 0.25\,\mathrm{V}$ at $I_D = 60\,\mathrm{mA}$ $I_R = 10\,\mathrm{\mu A}$ at $V_R = 5\,\mathrm{V}$

to maximize the efficiency. The inductor should have the smallest possible R_{esr}: this requires a thicker conductor, which makes the inductor quite larger. The MOSFET should have both a low R_{on} and a low C_{oss}: a tradoff between the two is mandatory, as lower R_{on} can be achieved widening the transistor, therefore increasing the parasitic capacitaces and the gate charge Q_{g}. The diode should have the smallest possible forward voltage at the I_{PK} current level: this is often associated with higher reverse bias leakage currents, which is undesirable.

After a thorough comparative research, we selected the components listed in Table 2. Both the MOSFET and the Schottky diode are integrated in the same package, the NTMD4884NF by On Semiconductor. Note that at this design stage it's not possible to choose a particular inductor only on the basis of its R_{esr}: in fact the R_{esr} value of an inductor is strictly related to its inductance value, so the choice of the inductor must consider both features at the same time. The next paragraph will explain how this can be accomplished.

Simulation

The selection of the best values for parameters L, T_1, and T has been performed through computer simulations. Equations (13) to (16) have been implemented in a Matlab script and their sum, giving the total power loss, has been calculated assigning many different couples of values to parameters L and T_1; each time, the value of T has been obtained from the condition summarized by Equation (12), using Equation (11). Many simulations have been carried out varying the input power level and the voltage considered for the output supercapacitor. This allows to evaluate the efficiency performance of the converter for the widest possible range of operating conditions. At each change of the inductance value L, also the R_{esr} value has been modified according to a table containing the L–R_{esr} correspondances for a wide selection of the best inductor families available on market.

The result of some of these simulations are shown in Figure 9. It can be easily observed that on the right side the plot stops abruptly: this is because the values of L and T_1 corresponding to the points in the lower rightmost triangular area of the plot wouldn't allow the converter to operate in discontinuous current mode (DCM), making $T_1 + T_2 > T$.

Changing the operating conditions (V_O and P_{IN}), the borderline between DCM and non-DCM operation moves, as does the maximum efficiency point, denoted by the star symbol. In any case, however, the maximum efficiency point is always quite near to the borderline. Therefore, the choice of the best values for L and T_1 should correspond to a point as near as possible to the area where the maximum efficiency point lies more often, but remaining on the left of the borderline for the widest possible range of operating conditions. In general, the risk of crossing the borderline is higher in presence of great input power levels and a low voltage across the output supercapacitor.

After the comparison of a large set of plots obtained from the simulation of several different operating conditions, the tradeoff values of 330 µH and about 6.5 µs have been chosen for L and T_1, respectively. To satisfy the condition of Equation (12), a period $T = 35.2\,\mu\text{s}$ is required, corresponding to $f = 1/T = 28.4\,\text{kHz}$. The selected inductor is the ELC11D331F by Panasonic, which features an R_{esr} of just 350 mΩ.

Once the circuit has been physically implemented, only the adjustment of parameters T and T_1 remains possible, because L is the indutance value of an untunable inductor and thus it's fixed. In this situation, just one of the three degrees of freedom initially available remains, as we have now two conditions to satisfy: Equation (12) and $L = 330\,\mu\text{H}$. Therefore, it's actually possible to modify arbitrarily just one of the two parameters T and T_1, because the other must be tuned accordingly to Equation (12). Supposing to change the value of T while adjusting accordingly T_1, it's possible to obtain through a computer simulation the plot shown in Figure 10. It displays how the estimated conversion efficiency changes with respect to the operating frequency and the voltage across the supercapacitor, assuming again the lowest airflow speed. Checking the position of $f = 28.4\,\text{kHz}$ on this plot, we can observe that it's in the middle of the range of frequencies which maximize the efficiency-increase-to-voltage-increase ratio: this means that this choice of f allows on average to reach better efficiencies at lower output voltages.

Picturing the plot of Figure 10 in 3D and slicing it by a fixed frequency value, we would obtain a 2D plot showing the conversion efficiency as a function of the output voltage, for a given input power level and operating frequency. Considering an f value around 30 kHz,

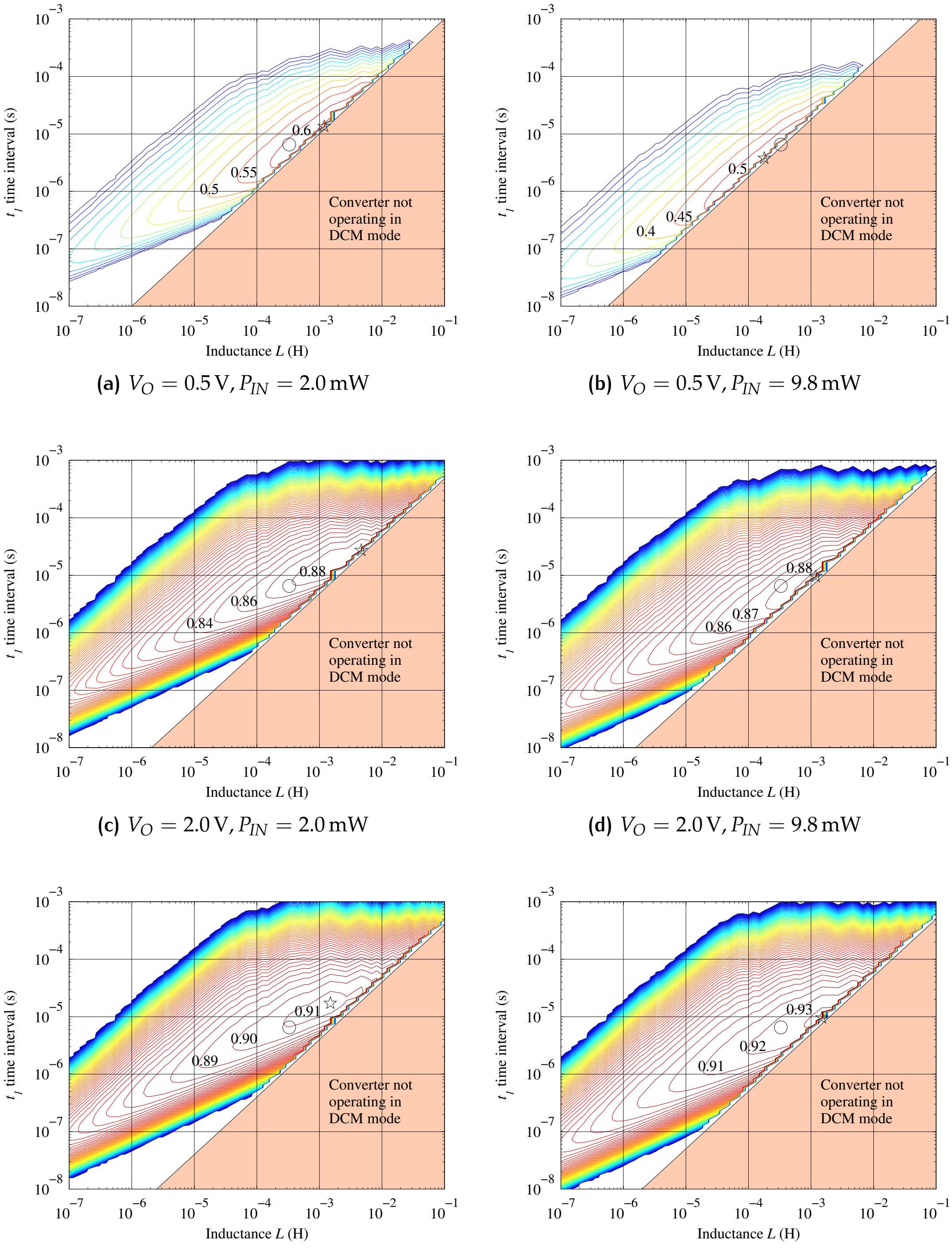

(a) $V_O = 0.5\,\mathrm{V}, P_{IN} = 2.0\,\mathrm{mW}$

(b) $V_O = 0.5\,\mathrm{V}, P_{IN} = 9.8\,\mathrm{mW}$

(c) $V_O = 2.0\,\mathrm{V}, P_{IN} = 2.0\,\mathrm{mW}$

(d) $V_O = 2.0\,\mathrm{V}, P_{IN} = 9.8\,\mathrm{mW}$

(e) $V_O = 3.5\,\mathrm{V}, P_{IN} = 2.0\,\mathrm{mW}$

(f) $V_O = 3.5\,\mathrm{V}, P_{IN} = 9.8\,\mathrm{mW}$

Figure 9. Simulation results of the efficiency performance of the converter for the a wide range of operating conditions (V_O and P_{IN}). The maximum efficiency point of each plot is denoted by the star symbol. The efficiency achieved by the final implementation (which uses $L = 330\,\mu\mathrm{H}$ and $T_1 = 6.5\,\mu\mathrm{s}$) is denoted by a circle.

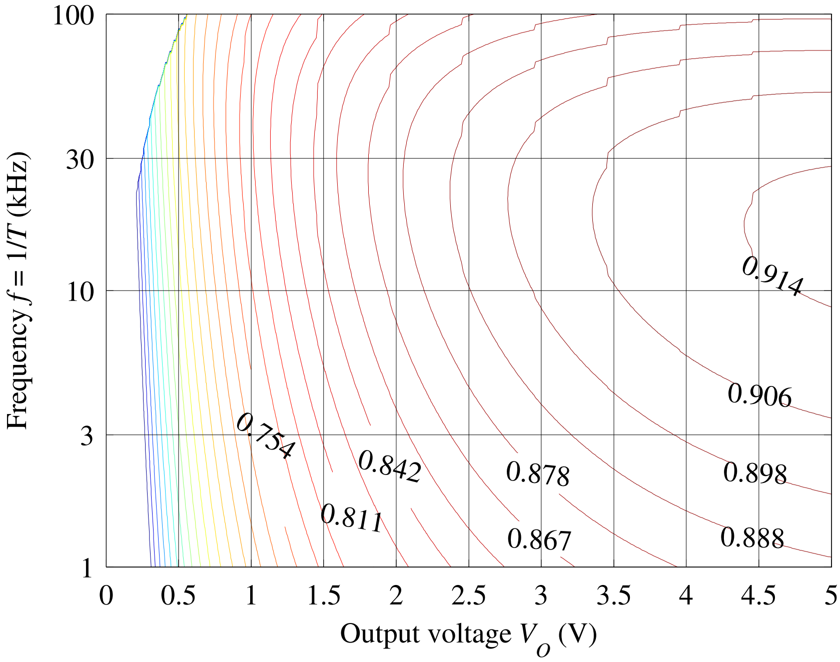

Figure 10. Contour plot of the conversion efficiency corresponding to different values of f and V_O, once $L = 330\,\mu\text{H}$ has been chosen. For this simulation we supposed $P_{IN} = 2.0\,\text{mW}$, obtainable with the lowest speed used for our tests and with $R_L = R_{IN,\text{eq}} = 550\,\Omega$.

we can see that the simulated conversion efficiency is greater than 75 % already at $V_O = 1\,\text{V}$; it exceeds 90 % at about $V_O = 3\,\text{V}$.

2.5.2 Control circuit

The converter requires a circuit driving the gate of the MOSFET with a voltage square wave of period T and duty cycle equal to T_1/T. To maximize the harvester overall efficiency, this circuit should consume the least possible power. Besides an accurate design of the circuit itself, an architectural-level strategy to cut down its power consumption is to cut its power supply every time that the speed of the airflow is not high enough to make the turbine turn, i.e. during wind calms.

The main problem arising in the implementation of this solution is how to sense the voltage at the output of the rectifier, which signals clearly whether the turbine is spinning or not. As Figure 7 shows, indeed, the voltage V_W is *floating*, i.e. none of the two electric potentials to which it is referred is the ground one. For this reason it's not possible to use a comparator powered by a ground-referred supply to directly compare this voltage to a threshold.

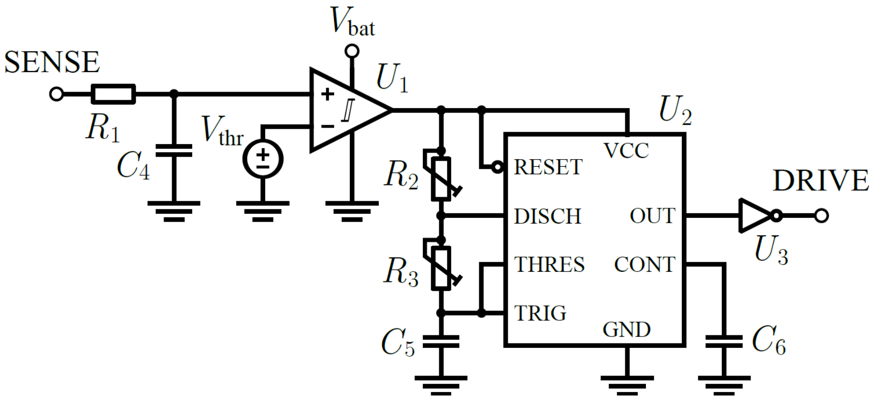

Figure 11. Qualitative diagram of the circuit which controls the operation of the buck-boost converter.

A simple and clever solution to this difficulty comes from a feature of the circuit in Figure 7. Applying the Kirchhoff's voltage law to the mesh including the MOSFET, the inductor and the rectifier output, we obtain that:

$$v_{DS} + v_L = V_W \tag{17}$$

where v_{DS} is the drain to source voltage of the MOSFET. The first two quantities are denoted lowercase because they vary during each cycle of the converter, whereas V_W remains practically constants over consecutive cycles, on the short term. If we average the previous equation on a period T, we get:

$$\langle v_{DS} \rangle_T + \langle v_L \rangle_T = \langle V_W \rangle_T = V_W \tag{18}$$

Remembering that in presence of periodic waveforms the average voltage across an inductor is zero, we obtain the following result:

$$V_{DS,\text{avg}} = \langle v_{DS} \rangle_T = \frac{1}{T} \int_{t_0}^{t_0+T} v_{DS}(\tau)\, \mathrm{d}\tau = V_W \tag{19}$$

It's thus possible to measure V_W performing an average of the drain-source voltage. The simplest way to implement this feature is through a low-pass filter connected between the MOSFET drain and the ground. The cutoff frequency of the filter must be quite smaller than the switching frequency of the converter (of the order of 10 kHz), but high enough to allow the filter output voltage to follow the airflow speed variations (around some hertz) without a substantial delay. A value in the range 10 Hz to 100 Hz should be suitable for the cutoff frequency of this filter.

This is exactly the function of the R_1-C_4 network positioned at the beginning of the control circuit we designed, shown in Figure 11. As

Figure 7 displays, the SENSE input is connected to the drain of the MOSFET. Through this filtering stage, the voltage V_W is reproduced at the non-inverting input of U_1. The output of U_1 becomes high when V_W is greater than a threshold voltage V_{thr} of about 200 mV; this value is high enough to protect against unwanted noise-induced commutations. For the integrated circuit (IC) U_1 we used an ultra-low power comparator with integrated reference voltage, the LTC1440 by Linear Technology. It consumes less than 3.7 µA over its full temperature operating range, but its output stage is capable of sourcing up to 40 mA. For these reasons it's the ideal device to monitor the presence of the wind and to power accordingly the oscillator stage which drives the MOSFET gate terminal.

The oscillator circuit is schematically represented on the right side of Figure 11. From a functional point of view, it's based on a 555 timer connected for astable operation. The frequency and the duty cycle of the square wave generated at the output port are determined by the values of R_2, R_3, and C_5 through the equations reported, e.g., in the datasheet [36]. Choosing a convenient fixed value for C_5, the possibility of setting just the R_2 and R_3 values is sufficient to achieve the desired range of frequencies and duty cycles. In the implementation, we used for U_2 an ICM7555 by Intersil, which is a complementary metal–oxide–semiconductor (CMOS) (hence lower-power) version of the classic 555 IC.

One limit of this 555-based solution is that it constrains the duty cycle to be greater than 50 %, whereas we need lower values. A possible workaround to solve this problem is to put a simple CMOS inverter at the output of the 555 timer, which also acts as a buffer to provide a smooth driving waveform to the converter MOSFET.

Overall, the only device of the control circuit independently powered is the comparator U_1. It receives the needed energy from the secondary battery belonging to the architecture of the multi-source energy harvester which comprises the present wind energy harvester (see Chapter 5).

2.6 EXPERIMENTAL RESULTS

The assembled multi-source energy harvester is displayed in Figure 12. The whole printed circuit board (PCB) area is of just 9.7 cm × 5.7 cm. After checking the smooth functioning of all the present sub-circuits, we carried out some tests to evaluate the real performance of the de-

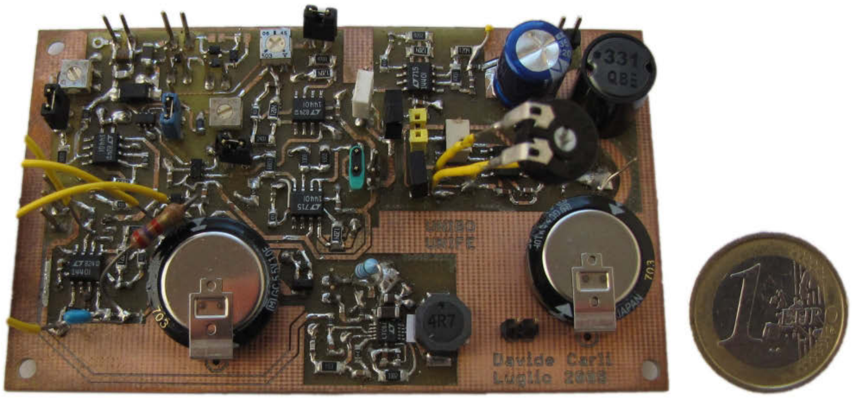

Figure 12. Picture of the assembled multi-source energy harvester. The wind energy harvesting section is on the rightmost side: from top downwards, the radial electrolytic capacitor C_1, the radial inductor L, the trimmer R_3 and the supercapacitor C_2 are clearly recognizable.

signed MPPT circuit and thus to verify the accuracy of the expectations provided by the simulations.

The aim of these tests is to measure the efficiency η of the converter for different values of its output voltage V_O, i.e. the voltage across the supercapacitor C_2. To obtain these data, we start discharging completely C_2. Then we apply at the input port of the converter a fixed voltage $V_{W,1}$, provided by a dc power supply previously set to simulate the presence of the wind generator hit by the airflow. In this way the converter begins its operation and C_2 starts charging. Afterwards, at known time instants, we measure the output voltage.

We use a dc power supply connected to the rectifier input instead of the real wind generator to avoid shifts of the operating conditions due to the turbulence of a fan-generated airflow, which would alter the experiment results. The dc voltage of the power supply has been set to obtain at the rectifier output, loaded with $R_{L,\text{opt}}$, the voltage:

$$V_{W,1} = \frac{R_{L,\text{opt}}\, p_{2,1}}{R_{L,\text{opt}} + p_{1,1}} = 1.04\,\text{V}\,; \tag{20}$$

the previous equation can be found using Equation (1) together with $V_W = R_L\, I_W$. $p_{1,1}$ and $p_{2,1}$ are the values of p_1 and p_2 corresponding to the lower speed used in our tests (see Table 1).

From the knowledge of the voltage V_O at two time instants t_0 and $t_1 = t_0 + \Delta t$ (so that $t_1 > t_0$), and using the well-known relation $E_C(t) = (1/2)\, C\, v_C^2(t)$ which expresses the energy stored in a capacitor of capacity C, it is possible to determine the average power supplied by the converter to C_2 during Δt through the following equation:

$$P_O(t^*; V_O^*) = \frac{\Delta E_C}{\Delta t} = \frac{C_2}{2\,\Delta t}\left[V_O^2(t_1) - V_O^2(t_0)\right]. \tag{21}$$

With t^* and V_O^* we denote the time instant or the output voltage to which one wants to relate this specific value of P_O: e.g., t^* could be assumed equal to $(t_1 + t_0)/2$, but also to t_1 or t_0, on the basis of the convention adopted. We were interested in the $\eta(V_O)$ relationship, so we linked each time the average output power to the voltage $V_O^* = [V_O(t_1) + V_O(t_0)]/2$.

Once $P_O(V_O^*)$ has been determined, it is possible to obtain the efficiency of the converter for output voltages around V_O^* using the equation:

$$\eta(V_O^*) = \frac{P_O(V_O^*)}{P_{IN}}, \tag{22}$$

where P_{IN} is calculated as $R_{IN,\mathrm{eq}}\, V_{W,1}^2$.

Through the calculation of $\eta(V_O^*)$ for some V_O^* values, corresponding to consecutive time intervals, it is possible to obtain a sampling of the real $\eta(V_O)$ curve. In theory, a more frequent measure of V_O should permit a better approximation of the $\eta(V_O)$ curve, but in practice this can lead to a more jagged progression of the data due to transitional deviations in the converter operation and in the supercapacitor behavior.

We executed several tests of this kind, changing each time the switching frequency of the converter, and adjusting accordingly T_1 to satisfy Equation (12), to verify the converter performance forecast by Figure 10. The results of some of these experiments are summarized by Figure 13. As expected, when C_2 is less charged the efficiency is lower but increases more quickly than when V_O is above 1 V. The switching frequency that makes the converter perform better for most voltages approaches the one we identified on the basis of the simulations, i.e. 28 kHz.

Despite this slight mismatch between simulated and experimental results, the efficiency with $f = 28\,\mathrm{kHz}$ remains satisfying for the whole tested V_O range: it's always above 81 % when V_O is higher than 0.8 V, with a maximum value of 87 %, which is very near to that expected from the simulations.

These data have been confirmed by field experiments. With an average wind speed of 16 km/h, the harvester can continuously generate an average power of 8.3 mW, with a conversion efficiency around 84 %.

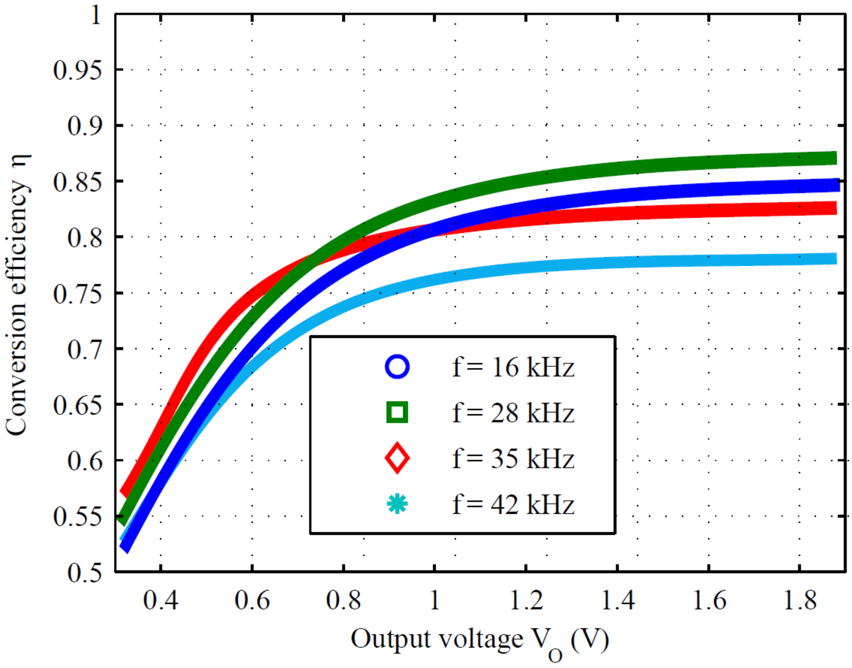

Figure 13. Plot of the measured efficiency in function of the measured output voltage, for different values of the switching frequency of the implemented converter. The power level applied at the converter input port during the tests is equal to the one obtainable using the lowest wind-flow speed used in our tests.

2.7 CONCLUDING REMARKS

A highly efficient energy harvester which exploits a micro wind turbine has been discussed in this chapter. It outperforms the ones proposed by similar works: it is able to supply up to 10 mW with an airflow speed of about 16 km/h, despite a turbine diameter of just 6.3 cm. A detailed design methodology, aimed at the minimization of its power losses, has been presented to achieve a fully analogue, highly efficient, very-small-scale wind scavenger. The plots resulting from the numerical simulations have been validated through experimental tests executed on the implemented harvester. Considering the expected operating conditions, designers can be aided by simulation results to evaluate all the relevant tradeoffs and to tailor the harvester to the application specific requirements.

3 VIBRATIONAL ENERGY HARVESTER

This chapter presents a self-autonomous piezoceramic energy harvesting system, capable of efficiently collecting vibrational energy from the operating environment and providing a dependable power supply to a wireless sensing node. Such nodes allow to build autonomous wireless sensor networks (WSNs) which are particularly suited to perform monitoring tasks in a number of different application areas, such as structural health, machine condition, traffic and railway condition monitoring for safety purposes [2, 37, 38]. The circuit architecture outperforms similar solutions available in literature in terms of standby power consumption, cold-starting ability and in-the-field customization, to accommodate a wide range of operating conditions and piezoelectric transducers. The soundness of the design has been experimentally assessed on the harvester prototype with a thorough analysis of the efficiency of all the circuits involved in the power processing chain.

3.1 INTRODUCTION

Several piezoelectic energy harvesters appeared in recent literature, each addressing a particular fraction of the wide application range of this technology, which can be broken down according to various criteria: size, achievable output power, integration level, piezoelectric transducer characteristics, expected source for the mechanical excitation, etc. [39]. With regard to the interface towards the operating environment, the present system takes advantage of the piezoelectric properties of a custom built ceramic cantilever beam to perform the electromechanical energy conversion. Electromagnetic and electrostatic principles can be applied for this purpose as well: the choice of the most suitable transducer technology is strongly affected by the characteristics of the specific application [40, 41]. Section 4.3.1 on page 54 will review the main features of piezoelectric and electromagnetic generators.

As for the electronic portion of the harvester, the circuit has been designed to operate reliably and efficiently in a wide range of operating conditions and to support different system configurations, with the aim of overcoming the limitations of similar systems recently proposed in literature, which will be discussed shortly [23, 25]. By means of two simple hardware tuning controls, the user can set up the harvester to work at its maximum efficiency with various piezoelectric or piezoceramic devices and in presence of several vibration levels, thus accommodating many different applications and deployment sites through in-the-field configuration capabilities. A clever bootstrap circuit enables the system to cold-start even after the exhaustion of energy reserves, coping with possible long periods of ambient energy shortage. A completely analogue control circuit, based on few ultra-low-power components, permits to keep both parasitic power consumption and implementation costs as low as possible. Finally, the use of a supercapacitor as system energy reservoir instead of a battery is another key point in rendering this harvester a flexible, self-contained, highly durable solution to supply any low power embedded system requiring a dc voltage under 5 V.

3.2 SYSTEM ARCHITECTURE

The schematic diagram of the proposed harvesting system is shown in Figure 14. The following subsections will give more details on the role of each functional block.

3.2.1 Front-end

The conversion of mechanical energy available in the operating environment to electrical energy is performed by a piezoelectric or piezoceramic device (*piezo device* from here on). When this device is subjected to vibrations, it generates an ac voltage, which is then rectified by a full wave Schottky diode bridge. Compared to other possible implementations (some alternatives are discussed in [9, 18, 25]), this rectifier provides a good efficiency without the added cost, complexity and power consumption overhead of other solutions.

In order to determine the load conditions maximizing the front-end output power, some tests must be performed at the output port of this block with varying load resistance R_L, at some fixed vibration levels. These measurements usually show that, for each excitation level, there is a load resistance value $R_{L,\text{opt}}$ which maximizes the generated power. According to the type of piezo device, the optimal resistance values for different excitation levels can turn out to be significantly different (as in the present case, see Section 3.3) or approximately equal (as in [23]). For convenience, we will refer to these two behaviors as *type D*

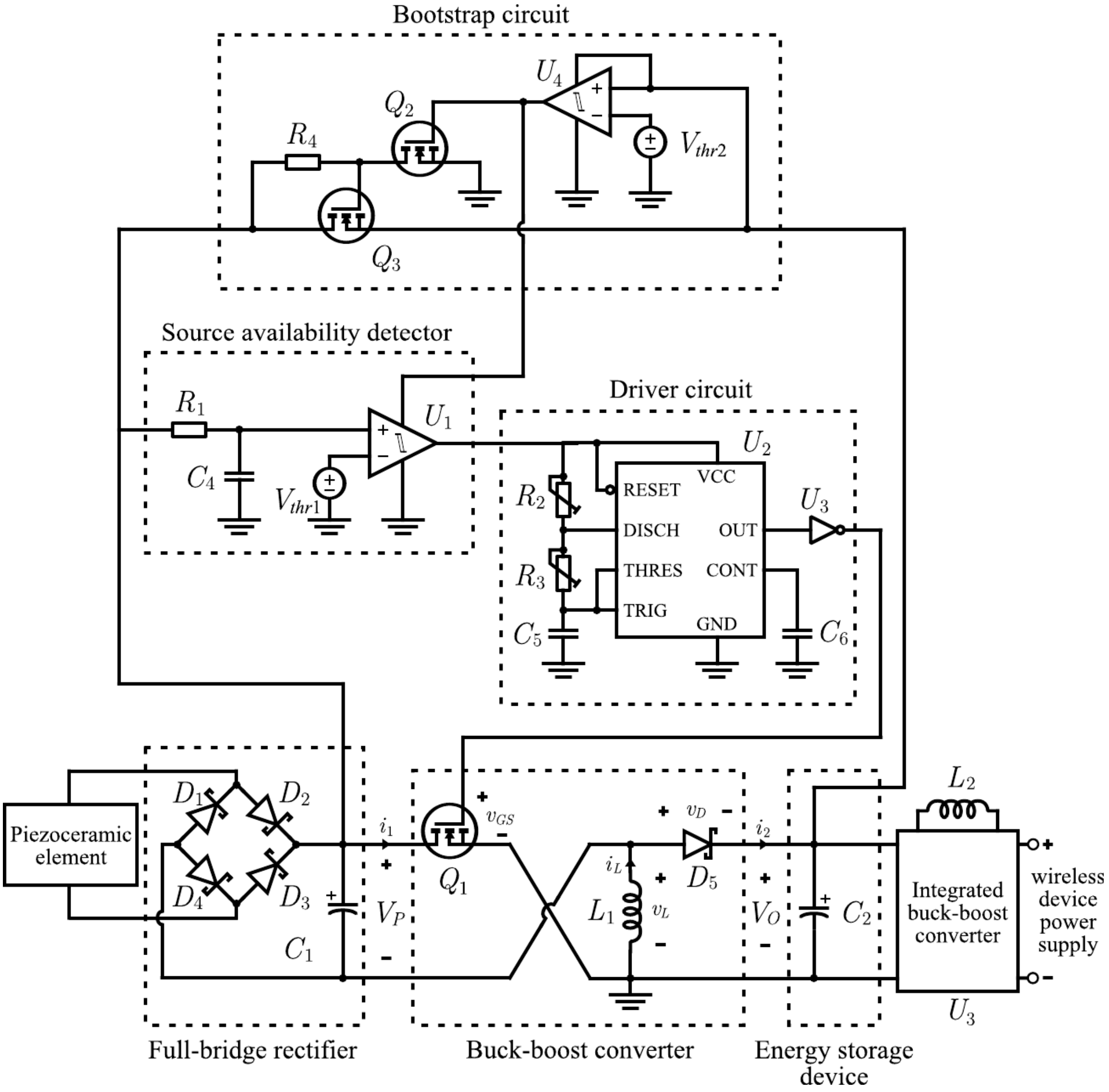

Figure 14. Architecture of the piezoceramic energy harvester, complete with the implementation of each functional block.

and *type E* front-ends, respectively. The fact that transducer devices can present either one of these behaviors is a well-known issue in the field of energy harvesting, and has been introduced in Section 2.2 on page 15.

3.2.2 Resistance matching circuit

The resistance matching block has basically two tasks: 1) to ensure that the front-end generates the maximum possible power under most of the expected operating conditions, and 2) to transfer the energy from the front-end to the energy storage device with the highest possible efficiency. On the grounds of the front-end characterization, the fulfillment of the first point requires this block to show a particular input resistance value when a certain vibration level is present.

Recalling the contents of Section 2.5.1 on page 26, such requirements can be accomplished by using of a dc/dc converter. Among the possible converter topologies, the buck-boost one has the inherent advantage of being able to emulate a specific input resistance value independent from input and output voltages, when operated in DCM [35]. For this reason the resistance matching circuit has been implemented through a buck-boost converter — a solution already adopted for the harvester presented in Chapter 2.

The average input resistance emulated by this converter can be expressed as

$$R_{IN,\mathrm{avg}} = \frac{2\,L_1 f}{D^2}\,, \tag{23}$$

while the condition guaranteeing its operation in DCM is

$$V_P < V_{P,\max} = \frac{1-D}{D}\,V_O\,, \tag{24}$$

where D and f are the duty cycle and frequency of the square waveform which drives Q_1, respectively. In order to maximize the front-end output power, D and f must be properly set to make $R_{IN,\mathrm{avg}}$ equal to the desired $R_{L,\mathrm{opt}}$ value, determined through the front-end characterization. The actual converter components (and especially L_1 value, concurring to set $R_{IN,\mathrm{avg}}$) have been selected through the procedure described in Section 2.5.1 on page 26, for the purpose of maximizing the circuit efficiency and flexibility with respect to $R_{IN,\mathrm{avg}}$ choice.

The converter output is connected to supercapacitor C_2, which constitutes the energy storage device of the harvesting system. It supplies the harvester control circuit, as well as the load embedded system by means of the integrated buck-boost converter U_3 (an LTC3530 by Linear Technology), which offers an adjustable output voltage and a very high efficiency (usually greater than 85 %).

3.2.3 Control circuit

The control circuit plays a major role in the harvester design, as it enables the other functional blocks to operate at their maximum efficiency in a wide range of operating condition, while keeping its own power consumption as low as possible.

During normal operation, when V_O is high enough to reliably power the control circuit, the detector circuit supplies the driver only when some vibrational energy is available. If there is no ambient energy at the harvester input, then the only components drawing some current from the supercapacitor are two ultra-low-power comparators with reference (LTC1540 by Linear Technology), which determine an overall current consumption of just 1 µA.

The bootstrap circuit recovers the system operation when the supercapacitor is completely empty, a condition which can occur after a long period of ambient energy shortage. When V_O is lower than $V_{thr_2} = 2\,\mathrm{V}$, all other control subcircuits are not powered, and the supercapacitor gets connected to the rectifier output. In this way the incoming energy recharges directly the energy storage device, restoring the minimum energy level required by the control circuit to work properly. The ability to recover from the condition of completely depleted energy reservoir, usually known as *cold start*, makes this harvester a completely autonomous supply system.

The driver circuit, drawing on the one described in Section 2.5.2 on page 33, is built upon a low-power version of the popular 555 timer, based on CMOS technology, connected to operate in astable mode. In this configuration, the frequency f and duty cycle D of the square waveform driving the converter are set by R_2, R_3 and C_5 values, through the relationships reported in the data sheet of the device. Since R_2 and R_3 are implemented by two potentiometers, the control circuit allows the user to tune the converter parameters, especially $R_{IN,\text{avg}}$, at any time.

This feature increases noticeably the flexibility of the proposed harvesting system in comparison with similar solutions currently available in literature. The authors of [25] do not provide any detail on the circuit employed to drive the converter, while in [23] the driving waveform is generated by a low power crystal clock, which definitively sets the values of f and D. According to Equation (23), this last implementation enables the emulation of a single $R_{IN,\text{avg}}$ value, so it can match the output resistance of a previously selected type E front-end or the output resistance of a generic type D front-end when subjected to a particular vibration amplitude level, if there is a fortuitous match with the only value emulated by the converter. In contrast, the present driver is able to match the output resistance of whatever type E front-end, or that of any type D front-end subjected to a freely selectable vibration amplitude, without employing any dynamic maximum power point tracking (MPPT) technique. Once the piezo device has been defined and the prevailing amplitude of the vibrations in the deployment site has been measured, the $R_{IN,\text{avg}}$ which maximizes the front-end efficiency can be easily set through R_2 and R_3 potentiometers. The same procedure can be applied to accomodate possible changes regarding the piezo device or the deployment site, which may be needed during the system life span. Figure 15 reports the diagram of this procedure.

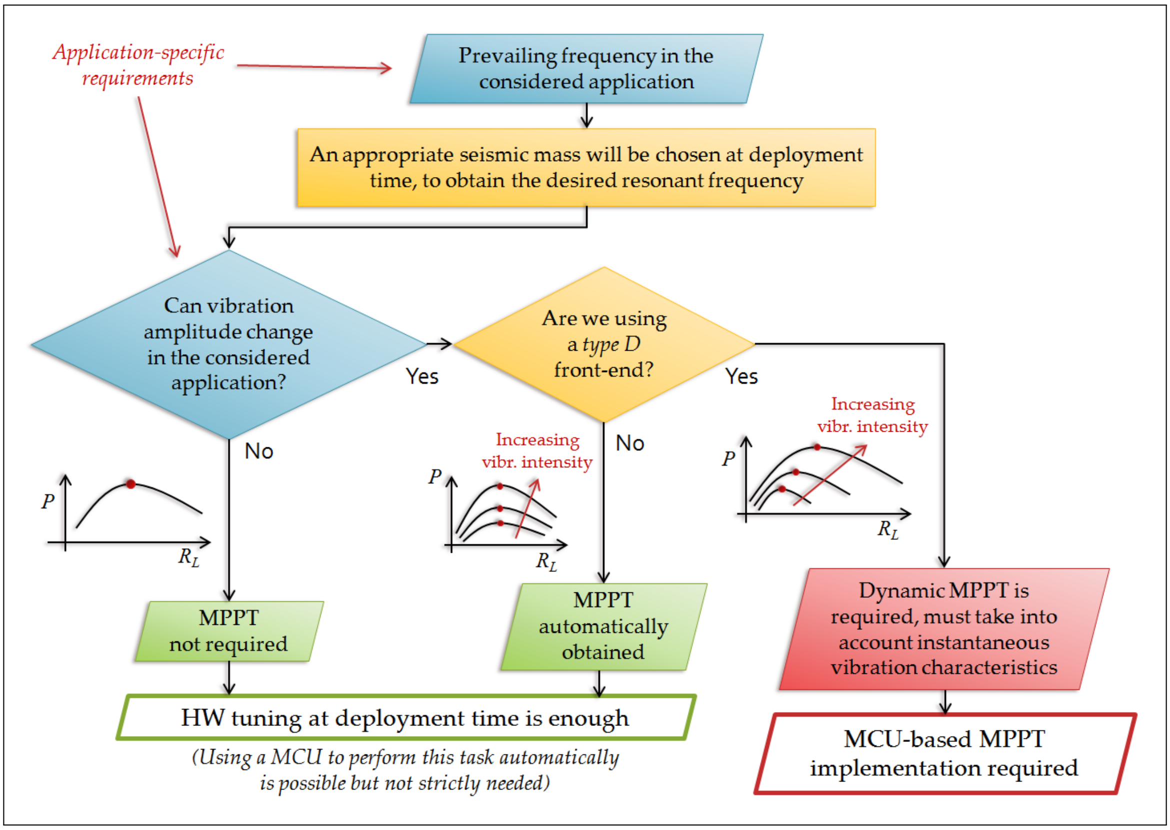

Figure 15. Design flow for the choice of the most suitable maximum power point tracking (MPPT) policy according to the characteristics of the specific application.

The flexibility of the proposed driver is further enhanced by the possibility of ensuring the DCM converter operation for a large range of excitation levels. To ensure a certain $V_{P,\max}/V_O$ ratio, Equation (24) can be solved to determine the needed value for D; then, considering the desired $R_{IN,\text{avg}}$, the solution of Equation (23) gives the value of f. The opportunity to set both $R_{IN,\text{avg}}$ and $V_{P,\max}$ at the same time brings another advantage over the solution adopted in [23], where fixed $D = 45\,\%$ guarantees DCM operation only when $V_P < 1.2\,V_O$.

3.3 EXPERIMENTAL RESULTS

3.3.1 System prototype

The prototype shown in Figure 16 implements the system described in Section 3.2, and has been employed to assess the performance of the proposed architecture.

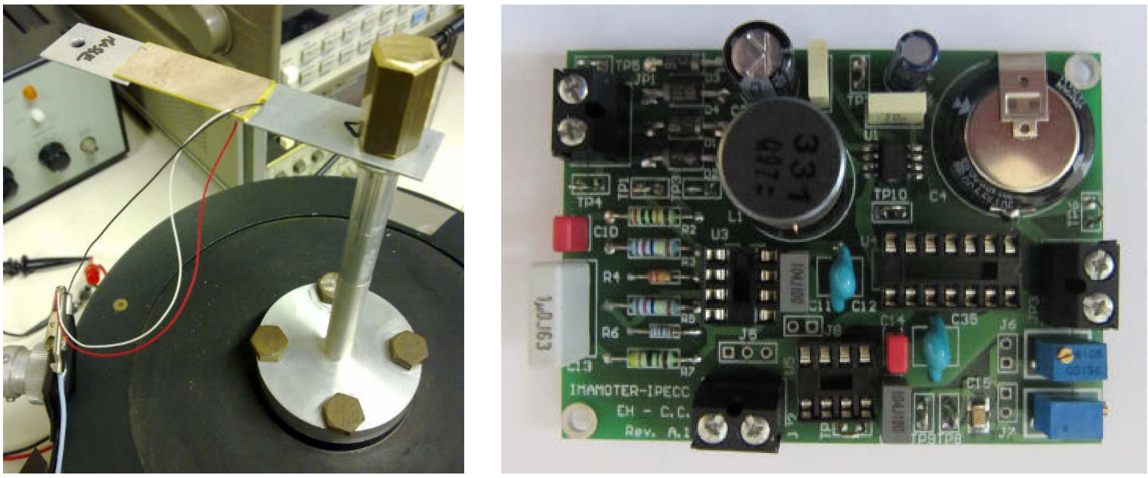

(a)

(b)

Figure 16. Prototype of the proposed energy harvester, composed of: (a) the custom piezoceramic cantilever beam, and (b) the electronic circuit board.

The mechanical-to-electrical energy conversion is performed by the cantilever beam of Figure 16a. It is a custom trimorph piezoceramic device, composed of two 300 µm thick layers of soft lead zirconate titanate (PZT) material separated by a 150 µm thick passive layer in-between. The global device size is 40 mm × 16.5 mm × 0.75 mm, and its resonance frequency is equal to 337 Hz. The electronic circuit in Figure 16b, corresponding to the schematic depicted in Figure 14, has been designed with testability and ease of assembly in mind, rather than miniaturization: this is why it features several through-hole components, which lead to an overall size of 75 mm × 55 mm.

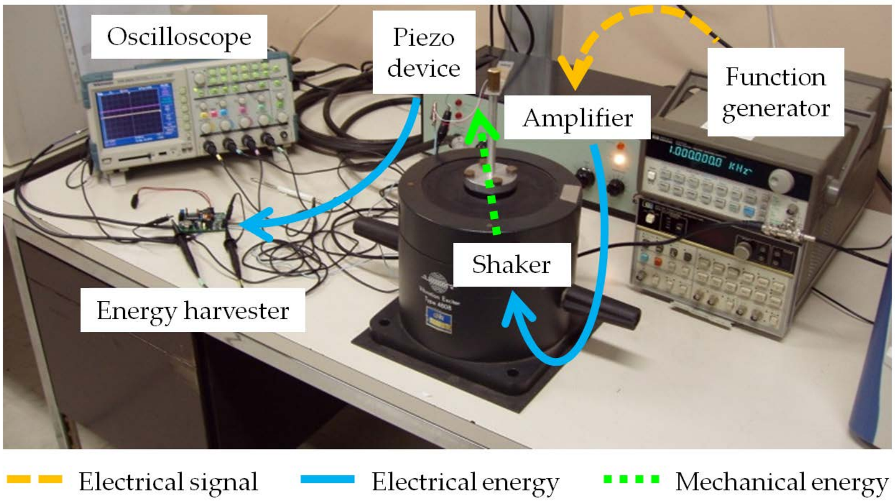

Figure 17. The test bench used to check the prototype operation and to measure its harvesting performances.

3.3.2 Test setup

The experiments have been conducted with the aid of the equipment shown in Figure 17. Apart from the oscilloscope (a measurement device) and the harvester prototype (the device under test), the purpose of all other instruments is to generate a mechanical excitation with selectable and repeatable characteristics, to provide the harvester with a well-known energy source. The function generator (HP 33 120A) produces a sine voltage waveform, with a frequency equal to the resonance frequency of the piezoceramic device, and a selectable peak-to-peak amplitude V_S. This low-power voltage signal is fed into the power amplifier (Brüel & Kjær 2712, set to provide constant voltage characteristics and maximum gain), which in turn drives the shaker (Brüel & Kjær 4808) with a higher-power version of the original sine wave. In this way, the oscillatory movement that the shaker transmits to the piezoceramic cantilever beam (constrained by one end to the threaded shaft of the shaker) has the same frequency of the function generator output waveform, and a variable amplitude dependent on V_S setting.

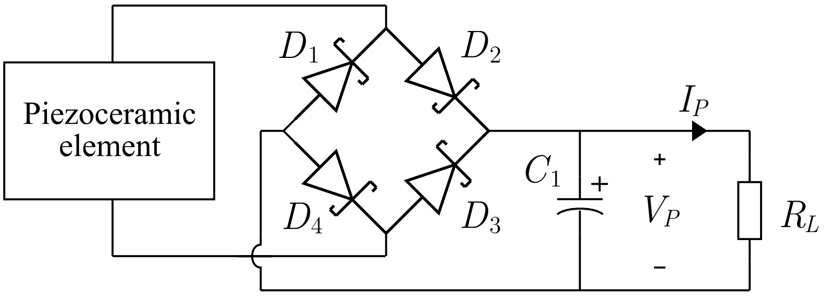

Figure 18. Circuit for the characterization of the front-end power generation capabilities under varying excitation and load conditions.

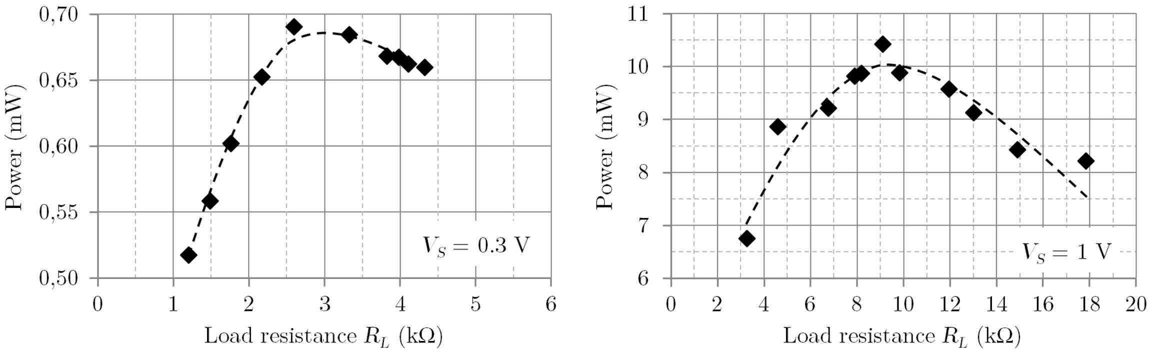

(a) (b)

Figure 19. Front-end output power plotted as a function of the load resistance R_L, and measured for two different excitation levels: (a) $V_S = 0.3\,\text{V}$, and (b) $V_S = 1\,\text{V}$.

3.3.3 FRONT-END POWER GENERATION

The first measurements have addressed the front-end characterization, to investigate its power generation capabilities and how they are affected by shifts in operating conditions. Using the circuit shown in Figure 18, the power dissipated on R_L has been measured with varying excitation levels (obtained through different V_S settings) and R_L values. The outcome of these experiments is reported in Figure 19, for two different vibration amplitudes. It can be easily observed that the generated power increases noticeably with the vibration amplitude, and that in both cases there is a load resistance value which maximizes the generated power: $R_{L,\text{opt}} = 2.6\,\text{k}\Omega$ when $V_S = 0.3\,\text{V}$, and $R_{L,\text{opt}} = 9.1\,\text{k}\Omega$ when $V_S = 1\,\text{V}$. Since the optimal load resistance changes considerably for different excitation levels, the front-end featuring the custom piezoceramic device can be categorized as type D. The comparison between these data and the results of similar experiments, with the load resistance directly connected to the ends of the piezo device, has provided an indirect measurement of the rectifier efficiency, which lies around 70 % in most conditions. The front-end characterization, if performed with the expected vibration amplitude at the actual deployment site, provides the $R_{IN,\text{avg}} = R_{L,\text{opt}}$ value that the resistance matching circuit should emulate to obtain the highest possible power.

3.3.4 Resistance matching circuit efficiency

The subsequent measurements have been focused on the custom designed buck-boost converter, and follow the approach already outlined in Section 2.6 on page 35. Beyond serving as the resistance matching circuit, this block plays a central role in the power path (it relays the energy from the front-end to supercapacitor $C_2 = 1\,\text{F}$), therefore the maximization of its efficiency is of paramount importance. In order to achieve the best performance in this respect, some experiments have been carried out to fine-tune the converter operating parameters, i.e. the timings of its driving waveform, which can be set adjusting R_2 and R_3. By changing each time the switching frequency f (and adjusting the duty cycle D accordingly to maintain the desired $R_{IN,\text{avg}}$ value, as required by Equation (23)), it is possible to obtain the converter efficiency figures for different frequency options. The results of such measurements are reported in Figure 20, for two different vibration amplitudes.

The first interesting thing to notice is that the efficiency drops slightly at the higher excitation level, regardless of the switching frequency and output voltage. This can be easily explained considering that in this case the current flowing from the front-end to the supercapacitor is larger, and remembering that the conduction losses of all converter components (Q_1, L_1, and D_5) are proportional to the square of the peak inductor current (see Equations (13) to (16) on page 29). Secondly, for both excitations, the efficiency increases with the output voltage: in all probability this is due to the inversely proportional relationship between D_1 conduction losses and V_O. Thirdly, it can be observed that the switching frequency ensuring the higher efficiency for most V_O values is around $f = 30\,\text{kHz}$, in both situations: so this seems to be the setting which provides the best converter performance over a wide range of operating conditions.

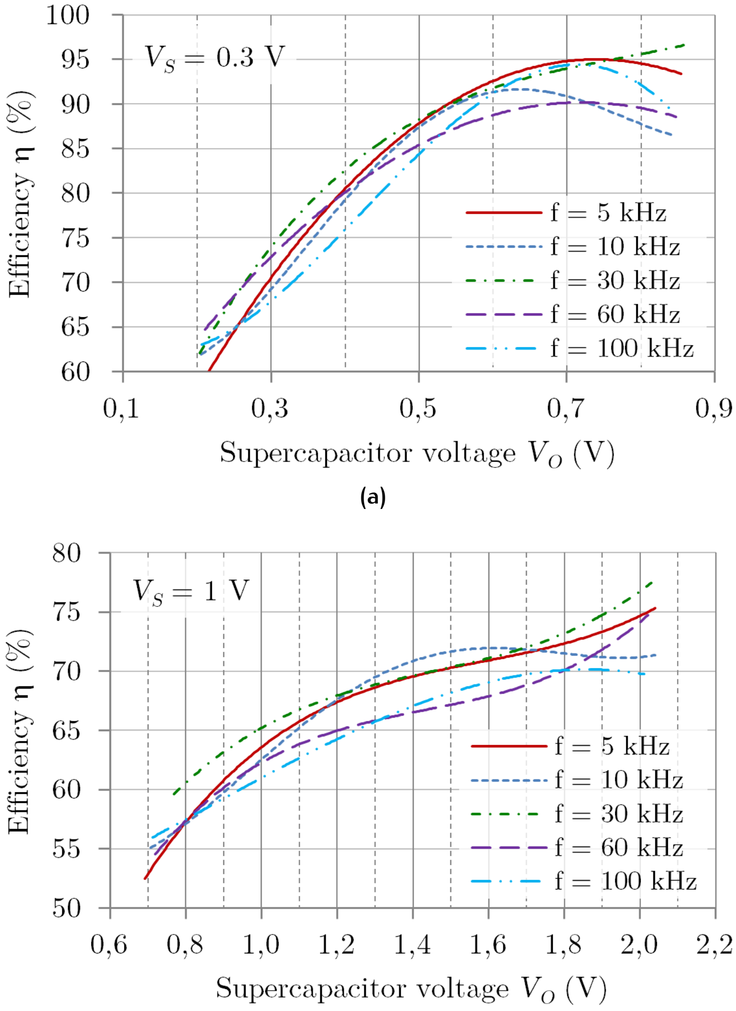

(a)

(b)

Figure 20. Efficiency η of the custom-designed buck-boost converter plotted as a function of the converter output voltage V_O (across supercapacitor C_2), and measured for some converter switching frequency values f in the range 5 kHz to 100 kHz and for two different excitation levels: (a) $V_S = 0.3\,\text{V}$, and (b) $V_S = 1\,\text{V}$.

3.4 CONCLUDING REMARKS

The system presented in this chapter fulfils many of the typical requirements for an energy harvester. Its architecture implements effective power saving strategies, and the choice of a supercapacitor as the energy storage device ensures a potentially unlimited lifetime. The cold-starting capability provided by the original bootstrap circuit makes the system truly autonomous, even when there is no stored energy left.

In addition to these core features, the circuit offers great flexibility and customization options. In particular, it can be configured to operate effectively with any piezoelectric transducer and to supply any low power electronic system, once their characteristics are known. The experiments on the prototype have proven that the design choices made to guarantee this flexibility do not affect the global performance of the harvester, which exhibits very good efficiency figures for vibrations of moderate amplitude — the most commonly found in real applications.

In order to further enhance the adaptability of the circuit to excitations with unpredictable characteristics, research activity on this harvesting architecture is still ongoing, with the aim of providing the system with dynamic maximum power point tracking (MPPT) capabilities.

4 SELF-POWERED SENSORS FOR AGRICULTURAL MACHINERY

Performance request, needs for fleet management, vehicle safety and diagnosis control strategies, ask for a continuous increase in vehicle functionalities and work variables observability and controllability. Self-powered wireless sensors, capable of collecting the power they consume directly from the vibrations available on the spot, could play a key role in enabling the sensorization of all those parts of heavy duty machines and trailed vehicles which cannot be connected through wires. This chapter investigates the applicability of self-powered wireless sensor nodes to heavy duty machinery by analyzing the energy budget which can be reached by these devices in such operating environment. A survey of possible sensor design is presented, to examine the energy requirements for signal transduction and wireless data transmission, and to highlight most relevant design issues affecting power consumption. Two representative case studies are then considered, to estimate with the support of original experimental data the amount of energy that can be generated by placing state-of-the-art off-the-shelf energy transducers on the gearbox of a baler and on the rear chassis of a tractor. By comparing the amounts of generated and required energy, the feasibility of self-powered wireless sensors in the context of heavy duty machines is demonstrated.

4.1 INTRODUCTION

Sensors constitute today the fundamental building block of many techniques aiming at improving the safety, performance, efficiency of heavy duty and agricultural machines, such as fleet management and precision farming. However, despite the ever-increasing advancements in this field, the placement of sensors on heavy duty and agricultural machinery is often still bound to those spots which can be reached by a cable. The use of wireless sensors instead of wired ones can play a key role in enhancing and widening the vehicle observability and controllability [42, 43].

Wireless communication technologies enable new solutions in terms of sensorization of drivelines, chassis, trailed vehicles and mountable working equipment, for both heavy duty machines and agricultural machines and equipment. This sensorization technique would simplify the connection between the machine and the trailer or the equipment, but primarily would allow the sensorization of elements that are traditionally non sensorized, like shafts and other rotating parts, and all other elements difficult to be connected through wires. Last but not least, this technique would permit the retrofit of existing vehicles too, increasing the control paradigm, the diagnosis (both local and remote) and the performance of existing fleets. Major advantages stemming from the adoption of such technology encompass enhanced condition monitoring and process control, increase in machine operational safety, reduction of machine break-downs and maintenance costs thanks to distributed diagnostics, reduction in cabling costs.

One of the major hindrances to the adoption of this sensorization solution is the issue of the power supply of wireless nodes. Each node needs a dedicated power source, which is usually a disposable battery, and thus needs periodic replacement. Besides the significant maintenance costs, this requires the wireless sensor node to be installed in a spot easily accessible to the operator, limiting heavily the freedom in the placement of the device. This problem can be widely mitigated or even fully solved by using self-powered wireless sensors, able to generate by themselves the energy they need to operate, collecting it from the environment.

On board heavy duty and agricultural machinery there is plenty of dispersed energy in the form of vibrations [44]. This energy could be easily converted to electrical energy by means of expressly designed transducers, capable to generate a current if stimulated by vibration sources in a definite range of frequencies (see Chapter 3 for an example). Due to known vibration frequency ranges of engines, gearboxes and transmissions, and due to vibration frequencies of chassis of off-road and, more in general, heavy duty vehicles, it is possible to design series of sensors capable to self-sustain their needs from the energetic point of view.

This chapter investigates the applicability of self-powered wireless sensor nodes to heavy duty machinery by analyzing the energy budget which can be reached by these devices when operating in such environment. A survey of applicable transducers is presented, along with some data on their performance when employed in similar applications, as reported by relevant related works. The design of very low power wireless sensing platforms is addressed as well, to examine the energy requirements for signal acquisition and wireless data transmission, and to highlight most relevant design issues affecting power consumption, such as those related to the wireless protocol. Two representative case studies are then considered, to estimate with the support of original experimental data the amount of energy that can be generated by placing state-of-the-art energy transducers on the gearbox of a baler and on the rear chassis of a tractor. The feasibility of the sensorization solution is finally evaluated by comparing the level of generated energy with that of consumed energy.

4.2 SYSTEM ARCHITECTURE

Taking into account the power consumption constraints affecting sensor nodes and the limited area which must be covered by the network, the wireless network topology best suited for the comprehensive sensorization of vehicles, implements and equipment working together is the star topology.

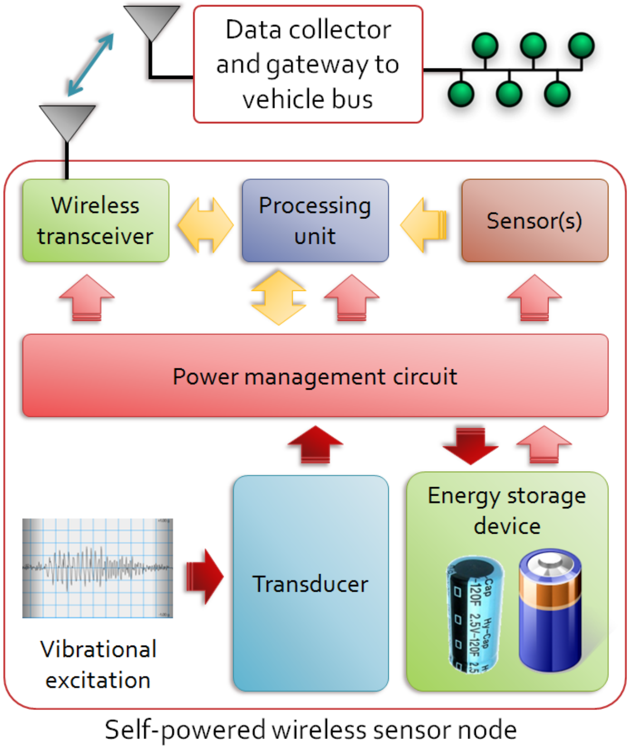

Figure 21. Architecture of a self-powered wireless sensor node. Red arrows denote the power path, whereas yellow arrows show the path of data signals.

As shown in Figure 21, the system is thus composed of the following devices: 1) a group of self-powered sensor nodes, which acquire the sensor information and transmit measured data via a wireless link at fixed time instants, and 2) a unique central data collector, placed on the main vehicle and powered from the battery of the latter, which collects the data sent by the sensor nodes and forwards them over the vehicle communication bus, which is usually a controller area network (CAN) bus.

4.3 DESIGN GUIDELINES FOR SELF-SUSTAINABILITY

In order to actually ensure the autonomous operation of a self-powered wireless sensor node, the design of each subsystem must be done in a power-aware fashion, taking into account every aspect which could affect the overall power consumption of the node. This section analyzes the energy requirements of each subsystem, addressing relevant design issues and highlighting the tradeoffs between lowering the power consumption and meeting the application requirements.

4.3.1 Energy transducer

The environment on board agricultural machines, trailed implements and working equipment typically provides several energy sources which could be harnessed to generate electric power, e.g. sunlight, temperature differences, and vibrations. Among these alternatives, vibrations represent the source with the best availability and predictability characteristics in this environment [44], and thus the choice of exploiting vibrations to power the sensor nodes is the most convenient one.

According to recent literature on kinetic energy harvesting, the most effective mechanisms to generate electricity from vibrations are piezoelectric transduction and electromagnetic transduction [1, 40]. The former technique takes advantage of the piezoelectric properties of some materials, able to generate electrical charge in response to the deformation and the consequent mechanical strain induced by the vibrations. The transducer discussed in Chapter 3 takes advantage of this technology. The latter technique exploits instead the electromagnetic induction principle, so the transducer utilizes the change in the relative displacement of a permanent magnet with respect to a conductor coil to generate an electric current.

Inertial generators are the best suited mechanical systems to maximize the coupling between the vibration energy source and the transduction mechanism. Such systems possess a resonant frequency, which can be designed to match the characteristic frequency of the application environment. Devices performing the electromechanical conversion by means of piezoelectric or piezoceramic materials are commonly utilized in applications featuring a predominant vibration frequency in the 1 Hz to 200 Hz range. A cantilever structure with piezoelectric material attached to the top and bottom surfaces is usually employed for this kind of conversion: it provides a low resonant frequency, which can be further reduced by adding a mass at the end of the beam. On the other hand, electromagnetic transducers are often used to convert vibrations at frequencies between 10 Hz and 10 kHz [40].

Off-road machines, trailers and working equipment provide many vibration sources, such as engine, power transmission system, axles, hydraulic circuit, power take-off (PTO), and chassis as well. Each of these elements generates vibrations with a specific spectrum, i.e. with different amplitudes at different frequencies. Considering that the effectiveness of inertial generators is maximum when they are excited at a specific frequency (their resonant frequency), the most attractive points for the placement of a sensor node powered by an inertial generator are those featuring vibrations with a large amplitude in a narrow frequency bandwidth. Designing the generator so that its resonant frequency lies in the middle of this narrow bandwidth ensures that it will always operate with the maximum efficiency, in that specific place.

There are some works in literature dealing with vibration energy harvesting on agricultural machinery. According to the authors of [45], the vibrations generated by many implements, when connected to different farm tractors, have often frequencies around 1 kHz, and accelerations up to $2\,\mathrm{g_{RMS}}$ (where $\mathrm{g_{RMS}}$ is the root-mean-square (RMS) value of an acceleration expressed in units of standard gravity $g_n = 980.665\,\mathrm{cm/s^2}$). By means of an off-the-shelf piezoelectric transducer, they managed to generate 724 µW at $2.0\,\mathrm{g_{RMS}}$, 167 µW at $1.0\,\mathrm{g_{RMS}}$, and 32 µW at $0.5\,\mathrm{g_{RMS}}$. The authors of [46] generated an average power of 200 µW from vibrations at a frequency of 60 Hz, with a piezoelectric transducer (rectifier circuit included) attached to the rear end of a forage wagon.

4.3.2 Hardware architecture

The hardware architecture of the self-powered wireless sensor node is strongly affected by both the application requirements and the availability characteristics of the vibrations on the spot, and should be tailored accordingly.

The simplest case is when the sensor is required to operate only when the vibrations are present. In such situation there is no need to include a rechargeable battery in the design: only short-term energy buffering is needed, so a supercapacitor can be chosen as the only energy storage device. This solution brings significant advantages in terms of lifetime of the node, because the maximum number of charge and discharge cycles borne by a supercapacitor is much higher than that of a rechargeable battery. However, this solution requires the power management block to include a bootstrap circuit, to be able to resume operation even when the supercapacitor is completely empty, after a long period of absence of vibrations. The harvesting system described in Chapter 3 provides a good example of this kind of architecture.

If instead the sensor node must remain operational even when the vibrations are not available, then the energy density provided by a supercapacitor alone could not suffice to the system needs: it depends on how long it should operate in absence of the ambient energy source, and on how strong the vibrations are when they are present. In this case a rechargeable battery could be added as energy storage device. In order to reduce the maintenance interventions to replace the battery as much as possible, the power management system should be designed to limit the number of recharge or discharge cycles, letting them take place only when the supercapacitor is completely empty or completely full, respectively. An implementation of this kind is presented in [45].

Aside from the policy implemented by the power management circuit and the available energy storage devices, also the processing and sensing units affect the system power consumption. As far as the application requirements allow it, the sensing unit should be implemented with the technology consuming the least possible amount of power, while keeping the sensor performance above an acceptable threshold. The processing unit, usually implemented by a microcontroller, or a system-on-chip (SoC) including the radio transceiver as well, can instead play a key role in overall power saving. Besides entering a sleep mode at fixed time intervals, it can also interface with state-of-the-art power management ICs to selectively enable or disable the power supply to each block of the sensor node, in order to prevent any standby current to flow when it is not needed. It can even implement advanced task management policies, in order to perform different tasks at different rates according to the power level available from the transducers and/or from the energy storage devices.

To provide some examples on the power consumption of state-of-the-art processing and sensing unit, a low-power microcontroller such as the MSP430 by Texas Instruments consumes about 250 µA when running at 1 MHz, and about 500 nA in sleep mode. Instead, a high-precision temperature sensor like the ADT7301 by Analog Devices consumes about 10 µA in active mode, and about 200 nA in power-down mode.

4.3.3 Wireless protocol

The wireless transmission of data packets can affect the overall power consumption of the sensor node in a significant way, because the radio-frequency (rf) transceiver is one of the circuits drawing the largest current in the system. Several parameters are decisive in this respect.

Considering the physical layer of the protocol, the output power setting of the power amplifier should be carefully selected, according to the wireless link budget which ensures a reliable communication between the specific node and the central data collector. Considering the overall size of a heavy-duty vehicle, even if a trailer is attached, the distance between an arbitrarily placed node and the central collector should be within few meters or tens of meters, and so it could be enough for the self-powered node to transmit with a power lower than the maximum allowed one. However, the fading affecting the wireless channel should also be taken into account, especially if the position of the obstacles along the path between the two nodes can change during the working session [47]. Besides, if there isn't the risk of exceeding the bandwidth allowed by regulations for the frequency band of choice, the bitrate should be kept as high as possible, in order to shorten the on-time of the transceiver power amplifier. Keeping transmitted data packet as short as possible also helps in this respect.

The data link layer of the protocol has an effect on power consumption too. The requirements of the application in terms of reliability, fault-tolerance, real-time constraints have a direct impact on the length of data packets, on the number and length of service packets needed to maintain synchronization between the nodes or to acknowledge reception of data, and on the need for the transceiver to remain in receiving mode for some time intervals, beyond transmitting packets. A good overview of these compromises can be found in [46], whereas a detailed review of protocols suitable to low power wireless sensor nodes is presented in [2].

To provide an example of the energy needed for a wireless transmission, a transceiver like the CC2500 by Texas Instruments consumes about $E_{\text{pkt}} = 19\,\mu\text{J}$ to transmit a 9-byte data packet, in the following conditions: supply voltage $V_{\text{cc}} = 1.8\,\text{V}$, bitrate $S_{\text{b}} = 500\,\text{kbps}$, rf output power $-10\,\text{dBm}$, with a self-calibration phase before the beginning of the transmission [46]. Figure 22 reports the profile of the transceiver supply current during the transmission of such a packet, and enables

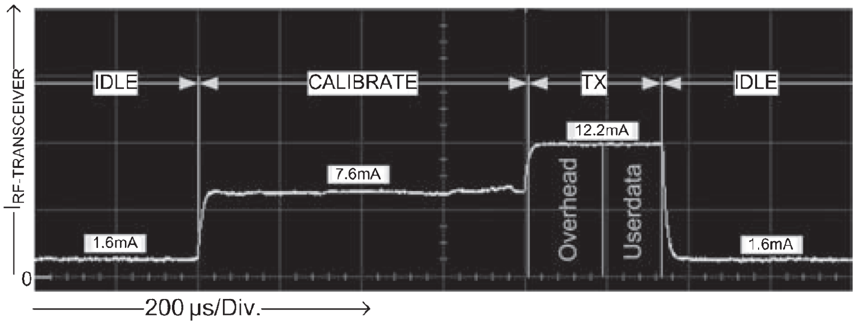

Figure 22. Variation over time of the supply current of the CC2500 rf transceiver, recorded during the transmission of a data packet with a data payload of 9 bytes and an overhead of 12 bytes, given by the preamble bits plus the syncronization word. Operating conditions and transceiver configuration: supply voltage 1.8 V, bitrate 500 kbps, rf output power −10 dBm, with a self-calibration phase before the beginning of the transmission. Source: [46].

to determine the contribution of each portion of the transmission process to the overall per-packet energy consumption. The energy E_b spent by the transceiver for the actual transmission of a single bit is given by

$$E_\mathrm{b} = P_\mathrm{tx}\, T_\mathrm{bit} = \frac{V_\mathrm{cc}\, I_\mathrm{tx}}{S_\mathrm{b}} = \frac{(1.8\,\mathrm{V}) \cdot (12.2\,\mathrm{mA})}{(500\,\mathrm{kbps})} = 43.9\,\mathrm{nJ}$$

where P_tx and I_tx are the power and the current consumed by the transceiver during transmission, respectively, whereas T_bit is the time it takes to transmit a single bit at bitrate S_b. The energy E_pl needed to transmit just the 9-byte user data payload can now be calculated

$$E_\mathrm{pl} = E_\mathrm{b} \cdot 8 \cdot 9 = 3.16\,\mu\mathrm{J}$$

as well as the energetic overhead E_oh spent for the self-calibration phase and the transmission of the preamble bits and the syncronization word

$$E_\mathrm{oh} = E_\mathrm{pkt} - E_\mathrm{pl} = 15.8\,\mu\mathrm{J}$$

Comparing E_pkt with E_oh and E_pl, it can be easily observed that a very large percentage (83 %) of the energy used to transmit a packet is not spent for the actual transmission of user data. This is especially evident for short payloads such as the one considered above; indeed, the energetic efficiency η_tx of the data transmission, given by

$$\eta_\mathrm{tx} = \frac{E_\mathrm{pl}}{E_\mathrm{pkt}} = \frac{E_\mathrm{pl}}{E_\mathrm{oh} + E_\mathrm{pl}} = \frac{8\,N\,E_\mathrm{b}}{E_\mathrm{oh} + 8\,N\,E_\mathrm{b}} \tag{25}$$

increases towards unity with increasing payload length N (in bytes). This holds true regardless of the specific transceiver.

These considerations demonstrate that, from an energetic point of view, it is much more efficient to transmit longer packets less frequently, than transmitting fewer bytes at a time but at a higher pace. If the application has not real-time constraints, it is thus advisable to wait a longer time interval between two consecutive packet transmissions, gathering a larger amount of data to send within each packet. Figure 36 in Section 4.4.4 will show how sending longer packets less frequently allows to increase the average data rate without affecting the average power consumption.

4.4 CASE STUDIES

In order to assess the feasibility of in-vehicle sensorization by means of self-powered wireless sensor nodes, two case studies based on original experimental data are presented in this section.

4.4.1 Baler gearbox

A baler has been considered as an example of trailed implement. Apart from the vibrations induced by the movement of the implement when trailed by the tractor, another attractive vibration source is the gearbox connected to the tractor PTO by means of a drive shaft. This vibration source is available for the whole duration of the implement operation, i.e. as long as the PTO of the tractor is active and the implement is attached to it.

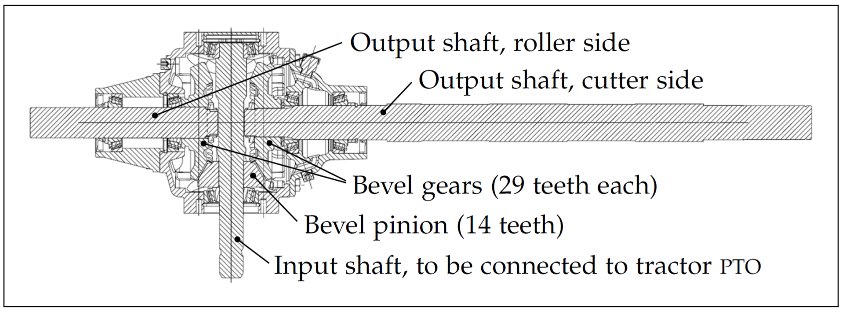

Figure 23. Cross-sectional view of gearbox model no. 292.218.00 manufactured by Comer Industries Spa, designed for baler applications.

To investigate the spectrum of the vibrations generated by such a device, the gearbox model no. 292.218.00 by Comer Industries Spa has been analyzed. The cross-sectional view of this device is displayed in Figure 23. This bevel gearing is composed of a pinion with $N_p = 14$ teeth, which drives two gears with $N_g = 29$ teeth each, normally connected to the roller and the cutter of the baler. The ratio of this gearbox is thus $M_g = N_g/N_p = 2.07$.

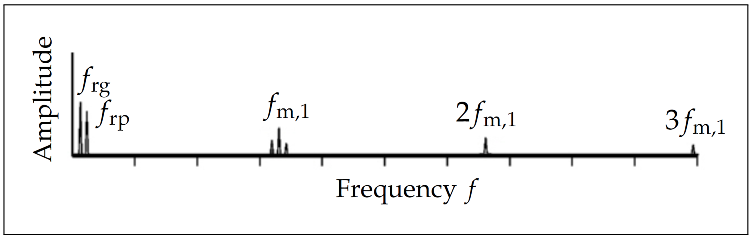

(a) Without gear load

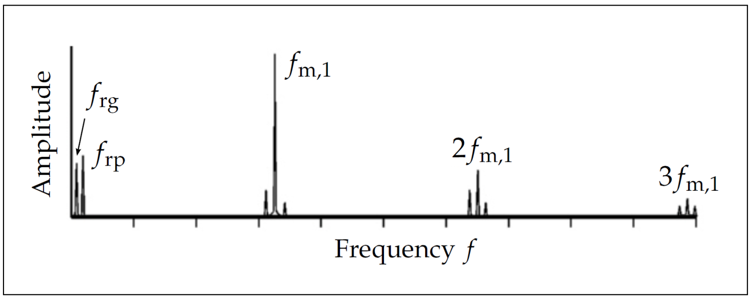

(b) With gear load

Figure 24. Typical vibration spectra of a gearbox, in presence of different load conditions.

The knowledge of these mechanical details and of the pinion speed (equal to the standard PTO rotational speed of 540 rpm) allows to predict the characteristics of the vibration spectrum of this device. According to the classic theory for gearbox vibration analyses [48], some vibrations are expected to appear at the pinion rotational frequency $f_{rp} = 9\,\text{Hz}$ and at the gear rotational frequency $f_{rg} = f_{rp}/M_g = 4.43\,\text{Hz}$, but most of them are expected to occur at the gear mesh frequency $f_{m,1} = f_{rp}\,N_p = f_{rg}\,N_g = 126\,\text{Hz}$ and possibly at multiples of this frequency, as shown in Figure 24a. If the load on the output shafts is increased, a substantial increase in the intensity of vibrations occurring at frequency $f_{m,1}$ is expected (see Figure 24b). It should be noticed that an additional mesh frequency $f_{m,2}$ is present, because in the test setup (described in the next paragraph) each output shaft is connected to an oil pump by means of a roller chain and a sprocket-wheel with $N_s = 26$ teeth: this determines $f_{m,2} = f_{rg}\,N_s = 113\,\text{Hz}$. Figure 25 schematically summarizes the relationships between these quantities, and the expected vibration frequencies.

The test assembly is reported in Figure 26. The gearbox input shaft is driven at the standard PTO rotational speed of 540 rpm by means of

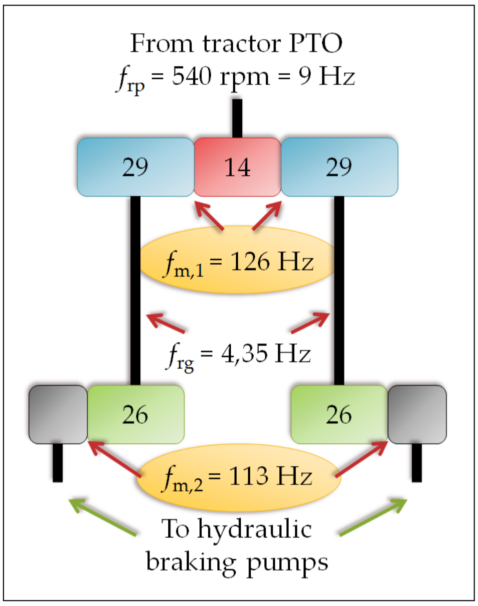

Figure 25.
Diagram of the gearbox assembly, with the detail of the rotational frequency of each part, and of the resulting mesh frequencies. Each gear is represented by a box, reporting the numer of teeth of the gear.

an electric motor, whereas each of the two output shafts is connected to an oil pump, which can simulate a fixed power load by means of hydraulic braking action. As shown in Figure 26b, three accelerometers have been fastened onto the gearbox enclosure, each pointing in one of the three directions set by the conventional three-dimensional reference system. To fully evaluate the spectrum of vibrations under different operating condition, the acceleration measurements have been taken at three load levels, emulated by means of the two oil pumps: 1) no load, 2) 10 kW on an output shaft and 20 kW on the other one (30 kW total), and 3) 20 kW on an output shaft and 40 kW on the other one (60 kW total).

The vibration spectra as measured on the Z axis are plotted in Figure 27. These spectra are very similar to the expected ones (see Figure 24): most vibrations concentrate at few discrete frequencies (so-called *spectral lines*), and the strongest vibrations occur at 113 Hz, which is equal to $f_{m,2}$, one of the two mesh frequencies. At this frequency, the acceleration is around 0.5 g_{RMS} in absence of load, and rises up (as expected) to 0.9 g_{RMS} in presence of a 30 kW total load. The spectra measured on X and Y axes have the same shape of those taken on the Z axis, i.e. they feature the same spectral lines, but the acceleration intensity is lower.

According to the remarks of Section 4.3.1, a kinetic energy harvester can effectively collect the energy of vibrations with such a frequency distribution: it will suffice to choose or design a transducer with a resonant frequency equal to $f_{m,2} = 113\,\text{Hz}$, at which the gearbox generates most vibrations. Besides, this value falls within the typical range of

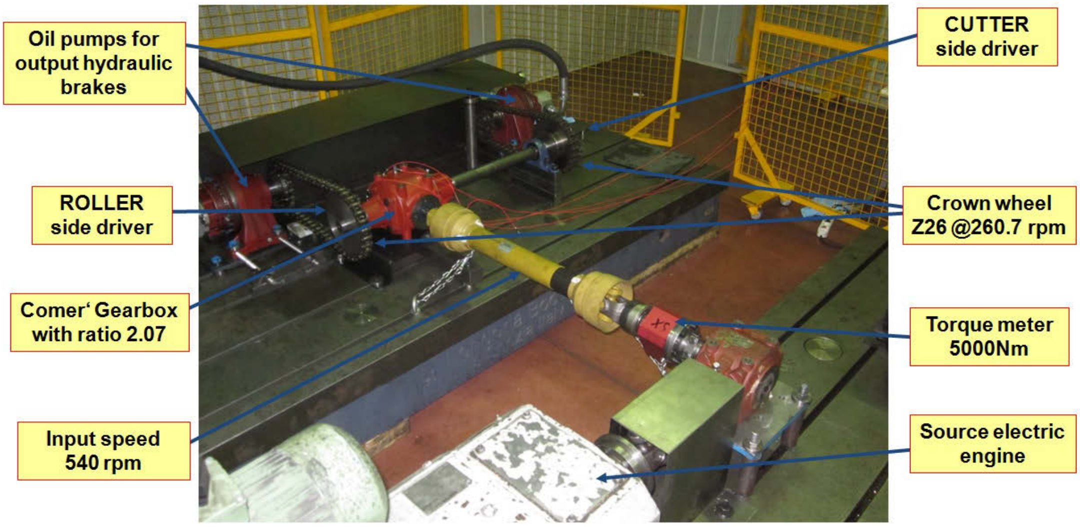

(a)

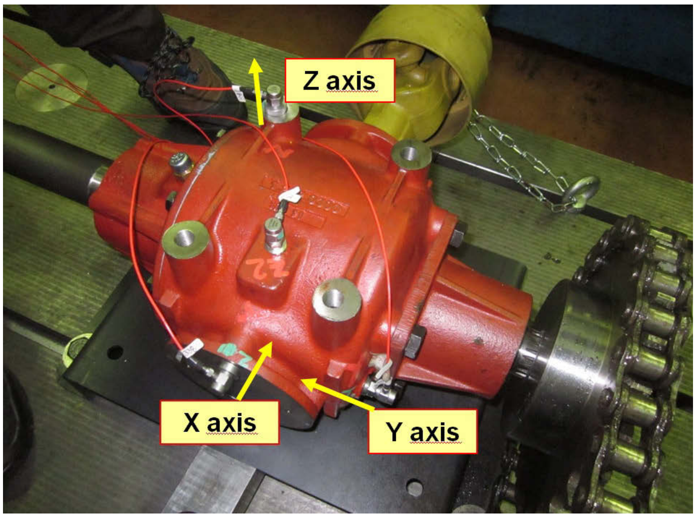

(b) Close-up of the placement of acceleration sensors

Figure 26. Set-up for the measurement of the vibrations generated by a baler gearbox.

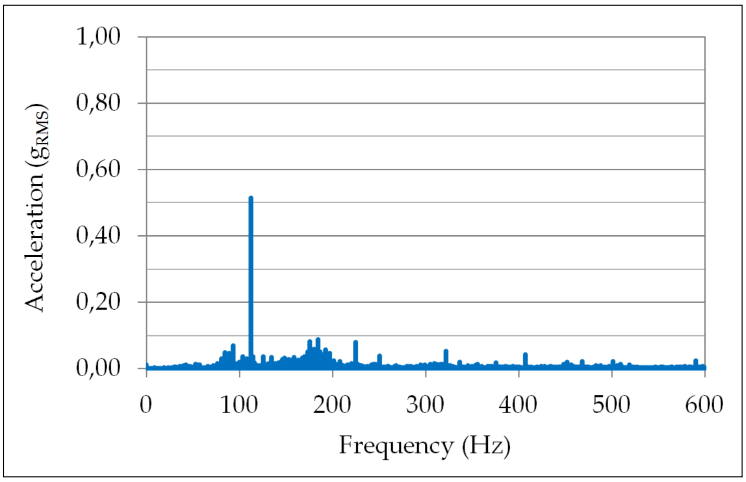

(a) Load: none

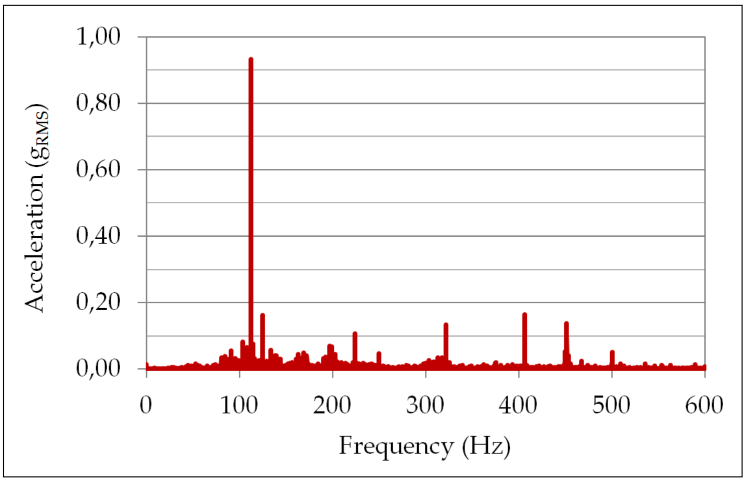

(b) Load: 10 kW on a shaft and 20 kW on the other (30 kW total)

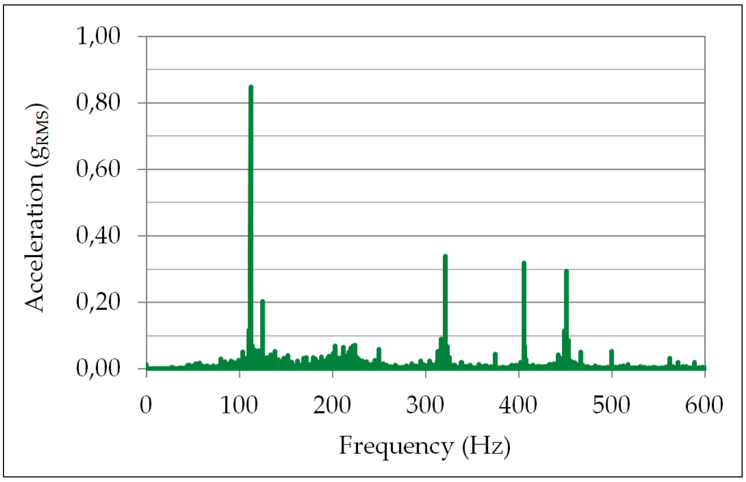

(c) Load: 20 kW on a shaft and 40 kW on the other (60 kW total)

Figure 27. Vibration spectra measured on the baler gearbox along Z axis, at different load conditions.

frequencies addressed by most kinetic harvster, both piezoelectric and electromagnetic ones.

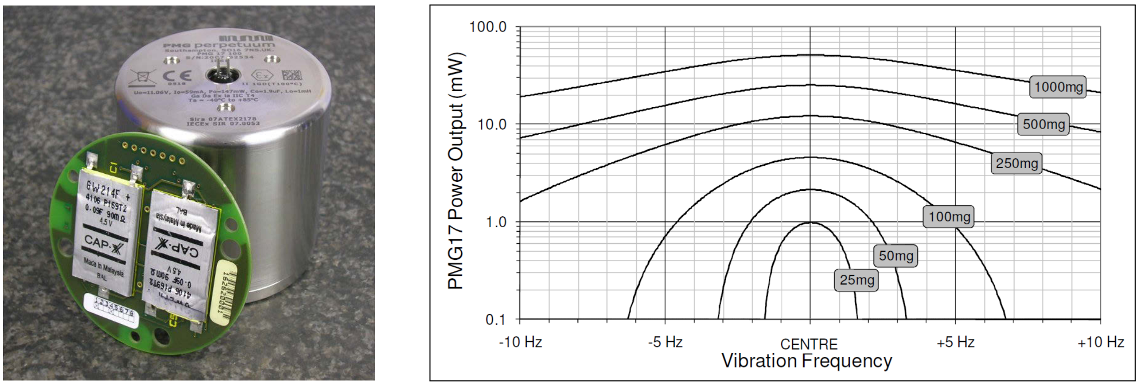

(a)

(b) Power output spectrum

Figure 28. PMG17 vibration energy harvester. Source: [49].

To provide an estimate of how much electric power can be generated by harvesting vibrations with such characteristics, a specific harvester can be considered. Among current state-of-the-art harvester implementations, as proposed in both commercial and research fields, one of the transducers most suited to this application is the PMG17 manufactured by Perpetuum Ltd, shown in Figure 28a. The original purpose of this device is to harness the most prevalent vibrations found on grid-powered electrical machines, which are at twice the line frequency. This explains why the device is marketed in two versions: the PMG17-100 is suitable to be used in countries where the line frequency is 50 Hz, whereas the PMG17-120 resonant frequency is at 120 Hz, i.e. at twice the frequency of a 60 Hz line. The resonant frequency of the latter model is very close to the prevalent vibration frequency measured on the baler gearbox, and so this device is suitable to be employed in the case under discussion. According to the power output spectrum provided by the manufacturer, presented in Figure 28b, the PMG17-120 can generate about 10 mW at (113 Hz; 0.5 g_{RMS}), and about 25 mW at (113 Hz; 0.9 g_{RMS}).

4.4.2 Tractor chassis

To evaluate the characteristics of the vibrations available on these parts, vibration data measured on a John Deere 6910 tractor with suspended front axle have been analyzed. These data, reported in Figure 29, have

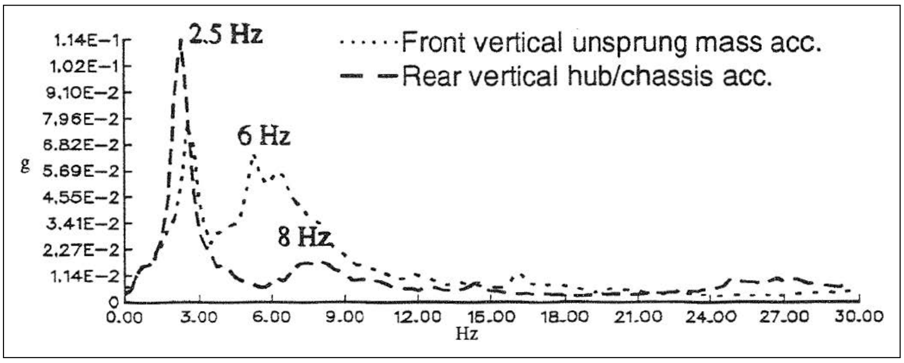

Figure 29. Vibration spectra measured on the chassis of a John Deere 6910 tractor driven at 40 km/h over a smooth artificial test track, as defined by ISO 5008 International Standard (see Figure 30). Courtesy of Deere & Company.

Figure 30. Smooth artificial test track, compliant with ISO 5008 International Standard [50].

been taken with the tractor driven at a speed of 40 km/h over an artificial test track compliant with the provisions of ISO 5008 International Standard [50], which specifies the methods for the measurement of whole-body vibration of the operator. This Standard defines the characteristics of two kinds of artificial test tracks, a smoother one and a rougher one: the spectrum in Figure 29 has been measured with the tractor driven on the smoother one (see Figure 30). These test conditions ensure the repeatability of the measurements and permit the comparison of the results with other data taken in the same conditions.

It can be observed that the vibrations on unsprung elements like the front axle and the rear axle/chassis are quite relevant. In particular, focusing on the data regarding the rear axle/chassis, there is a narrow frequency band around 2.5 Hz where most vibrations concentrate, and where the overall acceleration intensity is higher, with a peak around $0.114\,\mathrm{g_{RMS}}$.

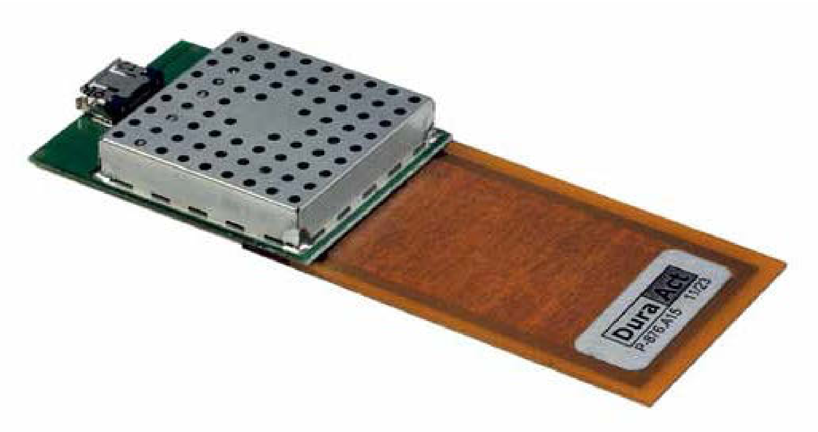

Figure 31. DuraAct piezoceramic patch transducer attached to a sensor board.

According to the remarks of Section 4.3.1, the electromechanical transducers most suited to harvest vibrations at such a low frequency are the piezoelectric ones. In current research literature there are few implementations of piezoelectric or piezoceramic harvesters working at this frequency, and none of them has been characterized with a vibration intensity similar to the one available on the rear axle/chassis of the tractor. To give an estimate of the electrical power which could be collected in such situation, a commercial piezoceramic transducer DuraAct P-876.A12 has been considered, because its manufacturer PI Ceramic GmbH provides the characterization of this device in operating conditions near to those of interest [51]. The transducer is shown in Figure 31.

Recalling the contents of Section 3.2.1 on page 40, the electric power P generated by a piezoelectric transducer is a function of both the vibration characteristics (i.e. vibration frequency f and vibration intensity, which can be expressed as acceleration a or displacement D) and the load impedance R_L: this can be expressed with notations $P(f, a, R_L)$ or $P(f, D, R_L)$. As displayed in Figure 32, the manufacturer provides a set of curves $P(f = 2.0\,\mathrm{Hz}, D_{PP}, R_L)$ for some discrete values of peak-to-peak displacement D_{PP} (Figure 32a), and a set of $P(f, D_{PP} = 5\,\mathrm{mm}, R_L)$ curves for some discrete values of frequency f (Figure 32b). The objective of this study is to determine the maximum of the $P(f = 2.0\,\mathrm{Hz}, a_{RMS} = 0.114\,\mathrm{g_{RMS}}, R_L)$ curve: this information is not directly available inside the plots provided by the manufacturer, but it can be obtain from them through a short analysis.

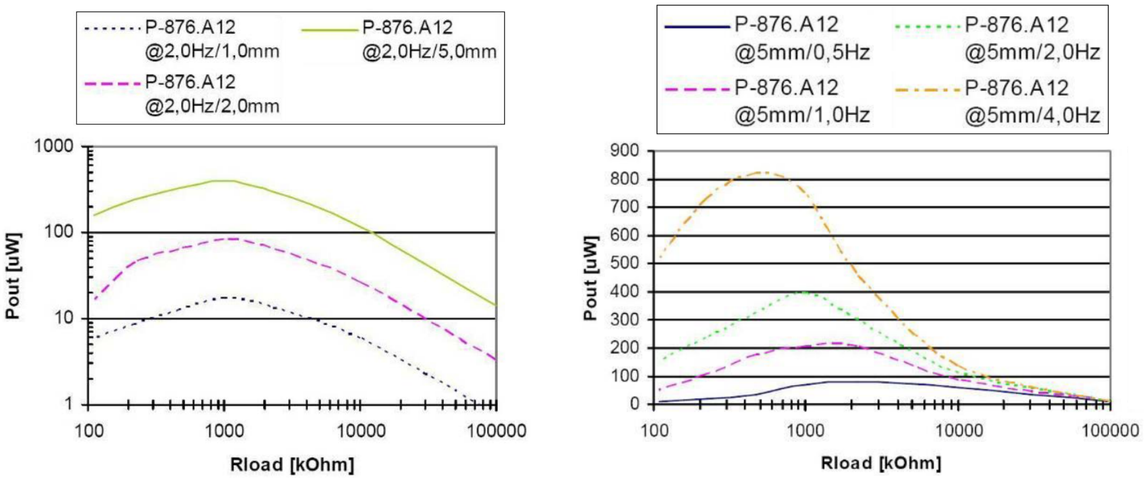

(a) Varying displacement **(b)** Varying frequency

Figure 32. Power generation capabilities of the DuraAct P-876.A12 piezoceramic transducer according to load resistance, and their trends when the displacement amplitude or the vibration frequency changes. Source: [52].

The first step is to calculate the displacement value from the known vibration characteristics. Considering the classic equations which describe a simple harmonic motion, in terms of displacement $s(t)$, speed $v(t)$, and acceleration $a(t)$

$$\begin{aligned} s(t) &= D_P \sin(2\pi f t) \\ v(t) = \dot{s}(t) &= 2\pi f \, D_P \cos(2\pi f t) \\ a(t) = \ddot{s}(t) &= -\underbrace{4\pi^2 f^2 \, D_P}_{=\,a_{PK}} \sin(2\pi f t) = -a_{PK} \sin(2\pi f t) \end{aligned}$$

a first relationship between the peak displacement D_P and the peak acceleration a_{PK} can be found. By taking into account that $D_{PP} = 2\,D_P$ and $a_{RMS} = a_{PK}/\sqrt{2}$, the conversion from a_{RMS} to D_{PP} can be eventually obtained

$$D_{PP} = \frac{a_{RMS}}{\sqrt{2}\pi^2 f^2} = \frac{0.114\,\mathrm{g_{RMS}}}{\sqrt{2}\pi^2 (2.5\,\mathrm{Hz})^2} \cong 12.8\,\mathrm{mm}$$

The value $D_{PP} = 12.8\,\mathrm{mm}$ is above the maximum displacement considered in Figure 32a (5 mm), so an extrapolation based on available data is required in order to obtain a power value for such a displacement. Firstly, it can be observed from Figure 32a that, for $f = 2.0\,\mathrm{Hz}$, an optimum load resistance value $R_{L,\mathrm{opt}}^{2.0\,\mathrm{Hz}} \simeq 1.1\,\mathrm{M\Omega}$ exists which maximizes power generation regardless of displacement. Since the objective is to determine the maximum power that DuraAct P-876.A12 can generate when subjected to the vibrations of a tractor chassis, the dependence of the generated power P on the load resistance R_L can be temporarily overlooked by considering $R_L = R_{L,\mathrm{opt}}^{2.0\,\mathrm{Hz}}$. Focusing on the $P(f = 2.0\,\mathrm{Hz}, D_{PP}, R_L = R_{L,\mathrm{opt}}^{2.0\,\mathrm{Hz}})$ data set, the relationship between P and D_{PP} can be easily explored, and the extrapolation for $D_{PP} = 12.8\,\mathrm{mm}$ can be performed.

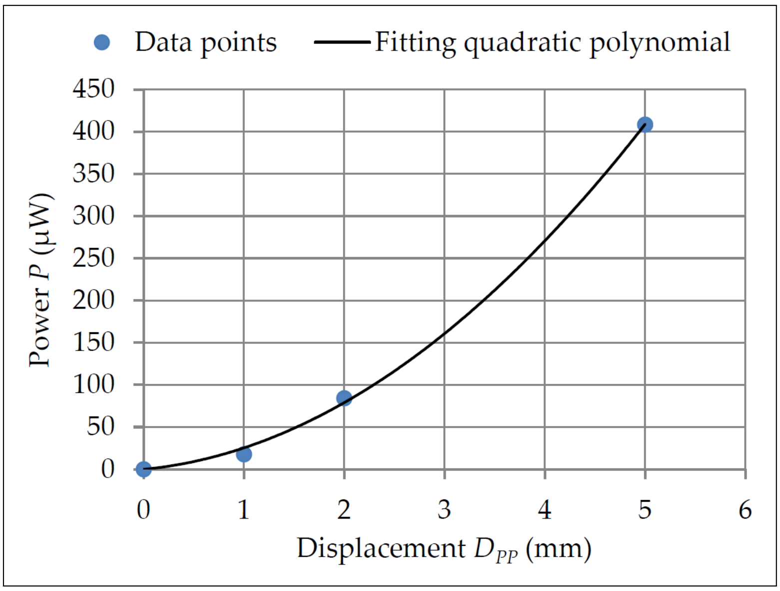

Figure 33. Graph of $P(f, D_{PP}, R_L)$ as a function of D_{PP}, when $f = 2.0\,\mathrm{Hz}$ and $R_L = R_{L,\mathrm{opt}}^{2.0\,\mathrm{Hz}} \simeq 1.1\,\mathrm{M\Omega}$. Except for point $(P, D_{PP}) = (0, 0)$, the plotted data points correspond to the maxima of the three curves shown in Figure 32a.

Reporting the $P(f = 2.0\,\mathrm{Hz}, D_{PP}, R_L = R_{L,\mathrm{opt}}^{2.0\,\mathrm{Hz}})$ data points available from Figure 32a on a P-D_{PP} chart like the one in Figure 33, their placements confirms that a quadratic relationship between the two quantities is very likely to exist [52]. The fitting of these data points by means of a quadratic polinomial leads to equation

$$P(f = 2.0\,\mathrm{Hz}, D_{PP}, R_L = R_{L,\mathrm{opt}}^{2.0\,\mathrm{Hz}}) \cong 14.1\, D_{PP}^2 + 0.0113\, D_{PP}$$

which allows to extrapolate the generated power when $D_{PP} = 12.8\,\mathrm{mm}$

$$P(f = 2.0\,\mathrm{Hz}, D_{PP} = 12.8\,\mathrm{mm}, R_L = R_{L,\mathrm{opt}}^{2.0\,\mathrm{Hz}}) \cong 2.45\,\mathrm{mW}$$

However the vibration on the tractor chassis is not at frequency $f = 2.0\,\mathrm{Hz}$, but instead at $f = 2.5\,\mathrm{Hz}$. The last step is thus to obtain $P(f = 2.5\,\mathrm{Hz}, D_{PP} = 12.8\,\mathrm{mm}, R_L = R_{L,\mathrm{opt}}^{2.5\,\mathrm{Hz}})$ from $P(f = 2.0\,\mathrm{Hz}, D_{PP} = 12.8\,\mathrm{mm}, R_L = R_{L,\mathrm{opt}}^{2.0\,\mathrm{Hz}})$.

It can be observed from Figure 32b that, for a fixed displacement, the maximum power obtainable from the DuraAct P-876.A12 increases linearly with the vibration frequency [52]. So $P(f = 2.5\,\mathrm{Hz},$

$D_{PP} = 12.8\,\text{mm}, R_L = R_{L,\text{opt}}^{2.5\,\text{Hz}})$ can be obtained by means of the proportion

$$\frac{P(f = 2.5\,\text{Hz}, D_{PP} = 12.8\,\text{mm}, R_L = R_{L,\text{opt}}^{2.5\,\text{Hz}})}{2.5\,\text{Hz}} = \\ = \frac{P(f = 2.0\,\text{Hz}, D_{PP} = 12.8\,\text{mm}, R_L = R_{L,\text{opt}}^{2.0\,\text{Hz}})}{2.0\,\text{Hz}}$$

which gives the final result

$$P(f = 2.5\,\text{Hz}, D_{PP} = 12.8\,\text{mm}, R_L = R_{L,\text{opt}}^{2.5\,\text{Hz}}) \simeq 3.0\,\text{mW}$$

Summing up, the DuraAct P-876.A12 piezoceramic transducer can generate about 3.0 mW when working with (2.5 Hz; 0.114 g_{RMS}) vibrations.

4.4.3 Energy budget

Power levels estimated in the two previous case studies refer to the electrical power directly available at the ends of the transducer, which is usually in the form of an ac voltage. Before being usable by the sensing, processing and communication units of the sensor node, this power must undergo some processing in the power management circuit. Since the power conversions taking place in this block have an efficiency lower than unity, the power actually available to the core units of the sensor node is lower than the power generated by the transducer.

In order to give a realistic estimate of the losses occurring in the power management circuit, a typical processing chain like the one presented in Chapter 3 can been considered. Usually the ac voltage at the end of the transducer is first converted to dc by means of a diode rectifier, which can employ either Schottky diodes or silicon diodes in relation to the amplitude of the ac waveform to be rectified. Then, in order to maximize the power output of the transducer, a dc/dc converter is often found, to perform the MPPT function. At this stage, the power can be stored inside the energy storage device. When this power is used to supply the sensing, processing and communication units on the node, an additional dc/dc converter is usually needed to provide a reliable supply voltage to the components.

If this sequence of processing steps is applied to the power levels estimated in the two previous case studies, considering for each step a realistic conversion efficiency value, then the power levels actually available for core electronics of the sensor node can be obtained. The detail of the conversion steps for the two case studies is depicted in

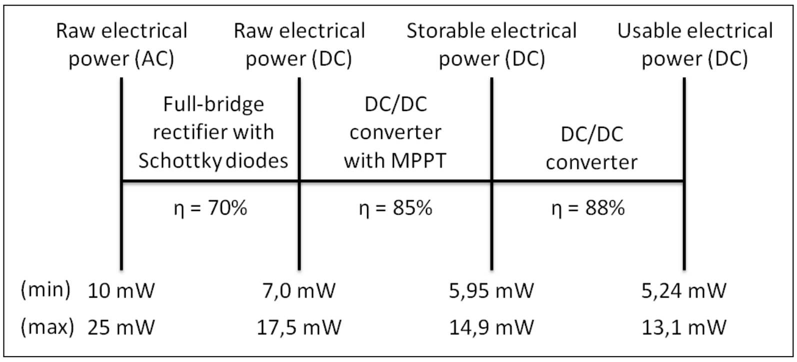

(a) Sensor node placed on the baler gearbox

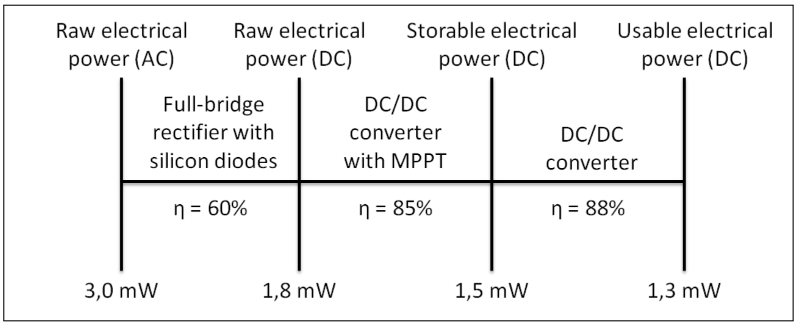

(b) Sensor node placed on the tractor chassis

Figure 34. Line diagram of the power distribution in the sensor node, for the two placement options addressed in this study.

Figure 34. It can be observed that the usable power when harvesting the vibrations on the baler gearbox ranges from 5.24 mW when the gearbox is not loaded, to 13.1 mW when it has a 30 kW power load. When harvesting vibrations from the tractor chassis, the usable power is around 1.3 mW.

Despite a reduction of about 50 % in both cases from the raw power at the ends of the transducer, these levels of usable power are rather higher than those recorded by the authors of [45, 46] on other agricultural machines, and can fully enable the autonomous powering of state-of-the-art wireless sensors.

4.4.4 Wireless data rate

To obtain an estimate of the average wireless data rate obtainable with such power levels, the consumption of a reference wireless sensing platform can be considered. A good example of a state-of-the-art wireless node is provided by [53]. This platform is based on the ICs described in Sections 4.3.2 and 4.3.3, and its architecture is depicted in Figure 35. According to the authors, this system can achieve a power consumption P_{slp} of just 4.73 µW when in sleep mode. Instead, the power consumption of the CC2500 transceiver during the transmission phase has already been discussed in Section 4.3.3.

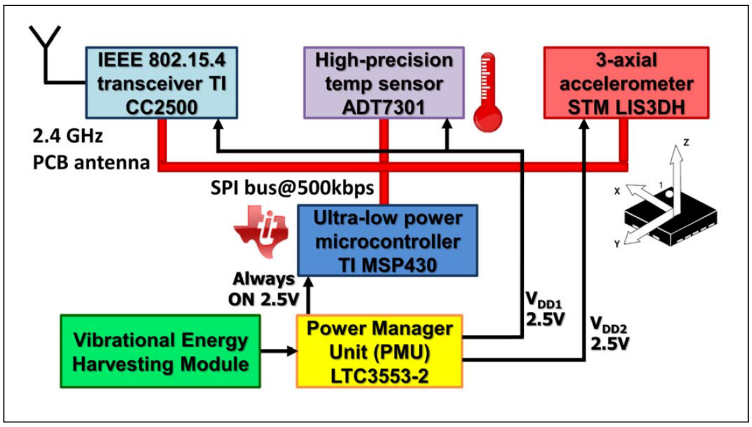

Figure 35. Hardware architecture of the reference wireless sensing platform considered for the estimate of the wireless data rate. Source: [53].

This sensor node is designed to simply transmit periodically a wireless packet containing the latest data measured by the on-board sensors. Therefore its operating cycle (with period T) is composed as follows: the node sleeps for a time interval T_{slp}, then it wakes up, it performs the measurements, it sends the wireless packet with the new data, and then it goes back to sleep for another time interval T_{slp}. The average power consumption P of this node can thus be expressed as:

$$P = \frac{E_{\text{act}} + E_{\text{slp}}}{T} = \frac{E_{\text{meas}} + E_{\text{pkt}} + P_{\text{slp}}\, T_{\text{slp}}}{T_{\text{act}} + T_{\text{slp}}}$$

where $E_{\text{act}} = E_{\text{meas}} + E_{\text{pkt}}$ and T_{act} are the energy and the time that the node spends in active mode, respectively: E_{meas} is the energy used to make the new measurements, whereas E_{pkt} is the energy consumed to send the wireless packet.

Usually the duty cycle of this kind of nodes is very low, so we can consider $T \cong T_{\text{slp}}$ because $T_{\text{slp}} \gg T_{\text{act}}$. Besides, the energy spent for the wireless transmission is much higher than that required to make the measurements, so we can consider $E_{\text{act}} \cong E_{\text{pkt}}$ because $E_{\text{pkt}} \gg E_{\text{meas}}$. Based on these motivations, the previous equation can be reduced to:

$$P \cong \frac{E_{\text{pkt}} + P_{\text{slp}}\, T_{\text{slp}}}{T_{\text{slp}}} = \frac{E_{\text{pkt}}}{T_{\text{slp}}} + P_{\text{slp}} \tag{26}$$

This expression clearly highlights how the average power consumption increases with increasing packet rate ($1/T_{\text{slp}}$), or with increasing per-packet energy, or with increasing sleep mode power consumption. The

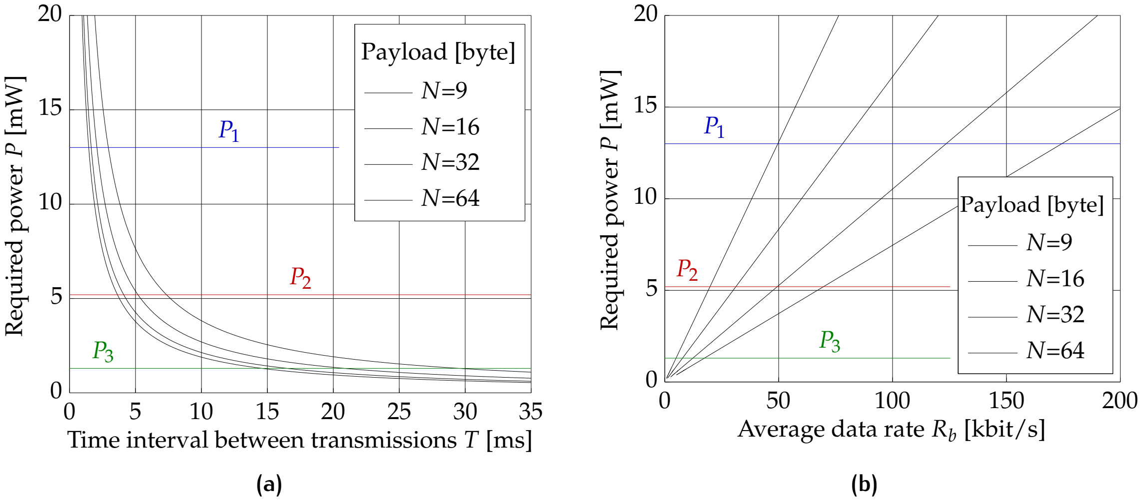

(a)

(b)

Figure 36. Relationships between the average power consumption P of the reference wireless sensing platform, the packet transmission rate, and the payload length, considering the transmission parameters listed in the caption of Figure 22. Power levels P_1, P_2 and P_3 are defined in Table 3.

former of these three relationships is plotted in Figure 36a, for different payload lengths.

Using Equation (25) and the symbols introduced in Section 4.3.3, Equation (26) can be further rewritten as

$$P \cong \frac{E_{\mathrm{oh}} + 8\,N\,E_{\mathrm{b}}}{T_{\mathrm{slp}}} + P_{\mathrm{slp}} = R_{\mathrm{b}} \left(\frac{E_{\mathrm{oh}}}{N} + 8\,E_{\mathrm{b}} \right) + P_{\mathrm{slp}}$$

where $R_{\mathrm{b}} = N/T_{\mathrm{slp}}$ represents the average data transmission rate. The relationship between P and R_{b} is plotted in Figure 36b, for different payload lengths. This graph clearly highlights how sending longer packets less frequently allows to increase the average data rate without bearing on the power consumption.

Supposing now to power the reference wireless sensor with the energy harvesting systems introduced in Sections 4.4.1 to 4.4.3, we obtain the wireless transmission performances listed in Table 3. These results are also highlighted in Figure 36 with the symbols P_1, P_2 and P_3, corresponding to the usable power levels available from three considered placement options (see table).

Table 3. Summary of the information regarding the case studies addressed in this chapter.

Harvester location	Baler gearbox with 30 kW load	Baler gearbox wihout load	Tractor chassis
Vibration frequency	113 Hz	113 Hz	2.5 Hz
Vibration intensity	$0.9\,g_{RMS}$	$0.5\,g_{RMS}$	$0.114\,g_{RMS}$
Proposed transducer	PMG17-120	PMG17-120	DuraAct P-876.A12
Transducer type	Electromagnetic	Electromagnetic	Piezoceramic
Maximum generated power	25 mW	20 mW	3.0 mW
Diode type in proposed full-bridge rectifier	Schottky diodes	Schottky diodes	Silicon diodes
Rectifier efficiency[1]	70 %	70 %	60 %
Global conversion efficiency[2]	52 %	52 %	45 %
Usable power	$P_1 = 13\,\mathrm{mW}$	$P_2 = 5.2\,\mathrm{mW}$	$P_3 = 1.3\,\mathrm{mW}$
Minimum time interval between transmissions[3]	1.5 ms	3.6 ms	15 ms
Maximum achievable average data rate[3]	48 kbit/s	20 kbit/s	4.8 kbit/s

[1] Estimated from available literature.

[2] Considering for each architectural block the efficiency values reported in Figure 34.

[3] Considering packets with a data payload of 9 bytes, and the transmission parameters listed in the caption of Figure 22.

4.5 CONCLUDING REMARKS

This chapter deals with the applicability of self-powered wireless sensors to heavy duty and agricultural machines, addressing many of the tradeoffs relevant to the design and the deployment of this sensorization solution.

This study highlights how the survival of a self-powered device, when placed on a specific part of the equipment, is strongly related to the vibration characteristics in that spot (in terms of spectral distribution, intensity, and variability with the working conditions of the equipment), to the electromechanical transducer employed, and to the power consumption characteristics of the sensing node. To ensure the reliable operation of the wireless sensor node, also in relation to the requirements of the target application, a careful planning of the sensor deployment is required.

Through the analysis of original experimental data on vibration spectra available on a baler gearbox and on a tractor chassis, and the estimation of the electrical power which could be generated in both cases, this work proves the existence of spots on agricultural machinery which provide a substantial amount of vibrations, capable to fully power a wireless sensor node and to let it sustain data throughputs compliant with the requirements of many real-time sensing applications.

Part II

MULTI-SOURCE HARVESTING SYSTEMS

5 MULTI-SOURCE ENERGY HARVESTER

5.1 INTRODUCTION

This chapter presents a multi-source, multi-storage energy harvesting architecture expressly designed to achieve autonomous operation and to constitute a dependable power source for low power applications ($< 100\,\text{mW}$). The proposed architecture is highly modular, supercapacitor-based and supports an arbitrary number of energy harvesting subsystems which can also be hot-plugged. The exploitation of several ambient energy sources in a concurrent and autonomous way improves the system reliability by reducing its dependence on the availability changes of each energy source.

During sustained periods of ambient energy shortage, the system operativeness is guaranteed by the presence of a nickel-metal hydride (NiMH) or lithium-ion (Li-ion) rechargeable battery. The power management circuit is designed to protect both battery types from overcharging and undercharging conditions, and when the battery intervention is required its energy is drawn in a pulsed way: a strategy that helps prolonging the battery autonomy [54]. Besides its flexibility and dependability, the implementation is fully analogue and requires relatively few ultra-low-power components: this minimizes the power consumption of the harvesting system itself, as well as its cost.

An energy harvester implementing the proposed architecture will be presented as well. It is targeted at stationary outdoor applications, and thus features two harvesting subsystems which collect the energy provided by wind flow and solar radiation. To simulate the system behavior and to plan its deployment in a specific site, a useful design framework has been implemented in Matlab simulation environment. It allows an in-depth analysis of the harvester operation under different environmental conditions, and validates the effectiveness of the design.

5.2 RELATED WORKS

While energy harvesting from a single energy source has been often investigated in literature (see [1] for a comprehensive and up-to-date survey, and the first Part of the present dissertation), there are fewer works dealing with the issue of energy collection from several sources at the same time and aimed at powering an electronic system with small average power requirements (around 100 mW or below). An up-to-date comprehensive review on this subject can be found in [55].

A well-known multi-source energy harvester is Ambimax [14]. It is targeted to power a WSN node in an outdoor environment, and relies on solar radiation and wind flow to collect the needed energy. As in our case, the system architecture is rather modular, thanks to a diode-based power ORing strategy. It includes a Li-ion battery as well, performing as backup energy reservoir: however, the continuous connection of the battery to the load during long periods of ambient energy shortage is not optimal, because a pulsed absorption from the battery (like the one implemented in our system) helps prolonging the battery autonomy [54].

Another work addressing WSN nodes in an outdoor environment is [16]. Both solar radiation and wind flow are exploited by this system too, but also the energy coming from water flow is harvested. The energy flow from each energy harvesting subsystem to the battery is controlled by a microcontroller: this brings some advantages, like the possibility of performing periodically a complete charge-discharge cycle to recover the battery after a high number of incomplete ones, but has a negative impact on the system modularity. To add another energy harvesting subsystem, for example, the software run by the microcontroller needs to be updated, and additional control signals must be available.

With regard to the architecture of the power management subsystem, two more works are worth to mention. The first one is presented in [56]: it is still at an early development stage, but contains an interesting idea. The authors of this work propose a multi-source, multi-storage and multi-load energy harvesting architecture based on a single multiple-input and multiple-output dc/dc converter, which automatically collects the energy from the sources and redistributes it among the storage devices and the loads. From a theoretical point of view the system is promising, however the only implementation by the authors relies on an externally powered field-programmable gate array (FPGA): this setup prevents the identification of any possible implementation issue and an analysis on the actual power consumption due to the harvesting system itself.

The second one is the work presented in [57]. Although this harvester relies only on the energy coming from the solar radiation, its storage subsystem features three supercapacitors, to improve the sys-

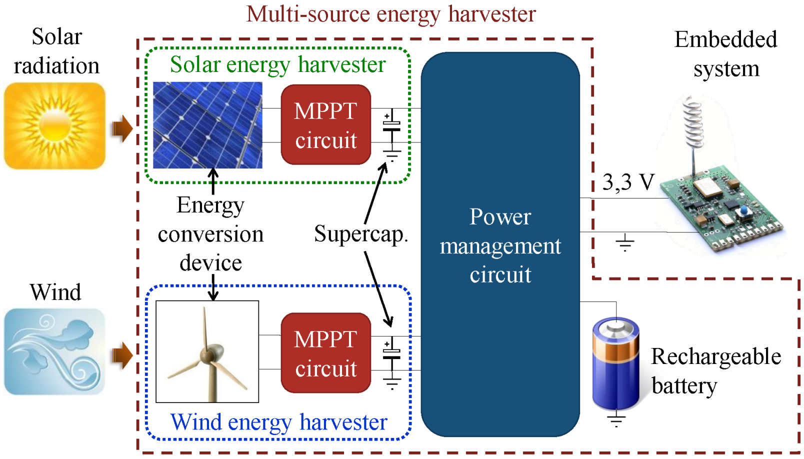

Figure 37. Architecture of the multi-source energy harvester.

tem reliability during the cold booting phase. Here the power path is dynamically managed by a set of MOSFETs, driven by a microcontroller-based control circuit. The MOSFET-based power ORing solution ensures the minimization of the parasitic power consumption along the power path. However, the whole system is quite complex and features also redundant blocks (like four dc/dc converters) which affect considerably power consumption and cost.

Finally, we report the existence of a commercial multi-source energy harvester, the EH-Link™ by MicroStrain, Inc. [58]. It is able to interface with several types of electrical generators (e.g. from vibrations, temperature differences, etc.), but the technical information disclosed by the manufacturer are too few to enable a fair comparison with the works mentioned above. However, at the moment the number of inputs is limited to three, and cannot be extended; besides, it does not seem possible to use the harvesting capabilities of the system for purposes different from the powering of the wireless node integrated in the system.

5.3 SYSTEM ARCHITECTURE

The architecture of the proposed multi-source energy harvesting system is depicted in Figure 37.

5.3.1 Energy harvesting subsystems

The energy harvesters at the first stage of the system provide the capability to convert certain kinds of ambient energy to electrical energy, and to store it temporarily for future usage. Although Figure 37 shows just two energy harvesting subsystems, the proposed architecture supports an arbitrary number of energy harvesters, which can all be connected to the power management circuit in a very straightforward manner, which will be detailed in the following sections.

With regard to stationary outdoor applications, the ones we are interested in, the energy sources most suited to be harnessed are solar radiation and wind, because of their wide availability and high power density [4]. These two sources, besides their property of being renewable, are also complementary to some extent: strong winds occur more frequently during night-time or when the weather is bad, than in sunny days [11]. For these reason, we have chosen to exploit these two ambient energy sources: this choice is in line with works [14, 16] already recalled in Section 5.2.

For the design, the development and the subsequent numerical simulation of the system, we considered as reference energy harvesters the airflow harvester presented in Chapter 2, and the highly optimized solar energy harvester described in [59]. The latter system relies on a small size photovoltaic (PV) panel with an area of just $112\,\text{cm}^2$. The PV panel conversion efficiency is kept as high as possible at any time by a clever MPPT circuit (thoroughly addressed in [60]), which is self-powered by a pilot cell: this allows the harvester to cold boot, i.e. to start working even when the output supercapacitor is empty.

5.3.2 Power management circuit

Through a simple diode-based power ORing strategy, the energy harvesting subsystems operate independently of each other: this also permits to hot-plug additional harvesting subsystems without the need of reconfiguring anything. Still, they can contribute at the same time, all together, to the replenishment of the system energy reservoirs. The main reservoir is a supercapacitor, while the second, optional, is a rechargeable battery. Both NiMH and Li-ion batteries are supported by the overcharge and undercharge protection circuits: however, the charge-discharge profile of NiMH batteries is best suited to the proposed battery control circuit. When the ambient sources provide more power than required by the load, part of the energy stored in the main reservoir is used to recharge the battery. The battery energy is used only when the charge of the main reservoir falls below an adjustable threshold. The embedded system is powered by a buck-boost dc/dc converter, providing a stable output voltage of 3.3 V. The input of this converter is directly connected to the main reservoir. To protect the battery from reaching an undercharging condition, the final dc/dc converter and thus the system are shutdown when the battery voltage falls below an adjustable threshold.

5.4 POWER MANAGEMENT POLICY

A functional scheme of the power management circuit is shown in Figure 38. It should be noted that this diagram is a simplified version of the actual schematic of the circuit: as indicated in the lower part of the figure, many of the used symbols represent the functionality of more complex sub-circuits. This choice has been made to simplify the comprehension of the high level operation of the circuit, without diverting the reader's attention with negligible implementation details. The sub-circuits U_1, U_2, U_3, and U_4 are based on an ultra-low-power comparator, the LTC1440 by Linear Technology; the reference included in this device has been employed to generate the desired threshold voltages V_{oc}, V_{uc}, and V_i, as well as to adjust the hysteresis of the comparator circuit. The logic functions performed by U_5 and U_6 have been implemented through low power, CMOS-based logic gates: in the context of Figure 38, they both operate as AND gates. The symbol associated to U_7 and U_8 represents a circuit operating as a monostable multivibrator. Finally, the switch S_1 has been implemented with an integrated programmable current-limiting switch, while a properly sized, low on-resistance MOSFET implements S_2.

The supercapacitor C_0 plays a key role in the proposed architecture: it works as the energy buffer from which the final dc/dc converter U_9 draws the energy to power the load. Every energy flow present inside the whole energy harvester, goes through this supercapacitor: (i) the one coming from the connected harvesting subsystems, (ii) the one coming from the battery when the environment does not provide a sufficient amount of energy, (iii) the one recharging the battery when the environment provides overabundant power, and finally (iv) the one which actually supplies the load, through the buck-boost converter U_9.

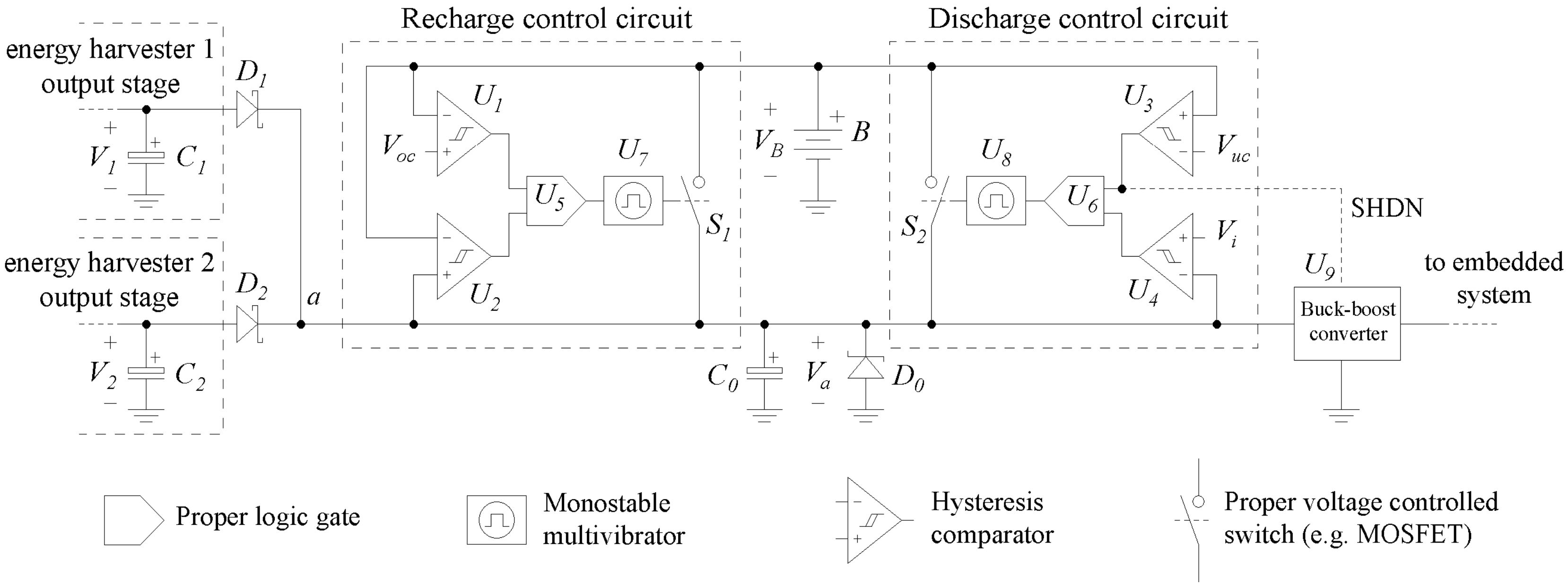

Figure 38. Functional scheme of the power management subsystem.

5.4.1 Harvesting subsystems interface

The power management circuit interfaces to the several energy harvesting subsystems with the diode-based power ORing solution shown on the left of Figure 38. This kind of connection ensures that C_0 is always charged by the harvesting subsystem with the highest output voltage and the presence of a diode on each line prevents the exchange of energy between different harvesting subsystems, and makes each of them completely independent from the others.

With respect to other power ORing solutions based on MOSFETs [61], the only drawback of the diode-based one is the parasitic power consumption caused by the forward voltage drop on the diode, when the current flows from a harvesting subsystem to C_0. To minimize this unwanted power consumption, we use very low forward voltage Schottky diodes to implement the power ORing connection. Considering the low current levels through these diodes (below tens of milliampere), the power overhead is comparable or below the one determined by a MOSFET-based ORing solution, which requires an additional driving circuit as well. Besides, the diode-based solution provides additional advantages, in terms of self-synchronization, low complexity and cost.

A proper sizing of the harvesting subsystem output supercapacitors ($C_1, C_2, \dots$) is required to ensure that each of them equally contributes on average to replenish C_0. For example, considering an architecture with just two energy sources, the value of C_1 and C_2 should satisfy the relationship $P_1/C_1 = P_2/C_2$, where P_1 (or P_2) is the average power generated by the first (or second) harvesting subsystem.

5.4.2 Battery control

The battery can connect to supercapacitor C_0, the main energy reservoir, through one of the switches S_1 or S_2. While S_1 allows C_0 to recharge the battery, S_2 allows the battery to recharge C_0: thus, in each switch, the current always flows in just one direction. As the battery cannot be recharged with a current greater than a certain value, S_1 is current limited with an adjustable limit value, while S_2 is not.

The recharge process is supervised by the *recharge control circuit*, and it starts when the following two conditions are satisfied: (1) the battery voltage V_B is lower than the overcharge threshold voltage V_{oc}, and (2) the voltage across the main reservoir V_a is greater than $V_B + 100\,\text{mV}$. The comparator circuits U_1 and U_2 respectively determine the satisfaction of these conditions: both are configured to have a $100\,\text{mV}$ hysteresis, but while in U_1 the hysteresis is symmetrical, in U_2 it is shifted by a quantity slightly greater than the width of the hysteresis itself. This ensures that the output of U_2 is never asserted when V_a is lower than V_B, otherwise the battery would recharge the supercapacitor. When both conditions are met, also the output of U_5 becomes asserted: this triggers the monostable circuit U_7, which maintains S_1 closed for an adjustable time interval of some seconds.

The role of U_7 is to keep S_1 closed for a time interval long enough to allow the completion of the charge redistribution transient involving C_0 and the battery: indeed, if U_5 drove S_1 directly, the transient would be interrupted too early, because U_5 output remains asserted for a very short time. This behavior is caused by the significant internal parasitic resistance of the supercapacitor, which makes V_a increase steeply when S_1 becomes closed, and this condition leads to the immediate deassertion of U_2 output.

If the overcharge condition is reached, U_1 prevents the battery to charge further. This means that, if the harvested power continues exceeding the power needed by the load, V_a is free to increase proportionally. To avoid V_a reaching the maximum voltage rating of C_0, a Zener diode D_0 is placed in parallel to C_0: when V_a reaches the Zener voltage (around 5 V), it cannot increase further, so the energy in excess coming from the harvesting subsystems is dissipated by D_0. The capacity and the maximum voltage rating of C_0 should be selected to make the reaching of this stage very rare.

The discharge process works very similarly to the recharge one: when (1) the battery voltage V_B is greater than the undercharge threshold voltage V_{uc} and (2) V_a falls below the discharge start threshold V_i, then S_2 remains active for a certain, adjustable time interval. V_i should be set to a level above the minimum input voltage supported by U_9, to ensure its continuous operation. To avoid deep discharging the battery, the output of U_3 is connected directly to the shutdown pin of U_9: if V_B falls below V_{uc} the power going to the load is cut off until the harvester collects enough ambient energy to recharge the battery over the level set by U_3 hysteresis.

5.5 SIMULATION RESULTS

The prototype shown in Figure 39 implements the proposed system. Both solar and wind energy harvesting subsystems have been fully characterized, as reported in [59] and in Chapter 2. The functionality of the power management circuit described in the previous section has been experimentally tested as well.

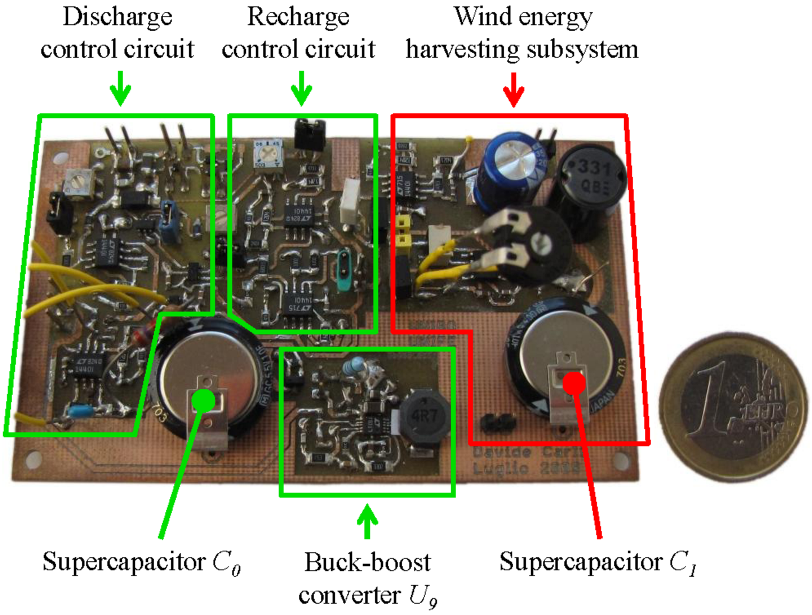

Figure 39. Prototype of the multi-source energy harvester.

To assess the overall harvesting capabilities of the whole multi-source energy harvester, and to verify whether it would be suited to a certain low power application before actually deploying the devices, we have developed a Matlab simulation framework to numerically evaluate the behavior of the harvester. The simulator allows the user to specify the time sequence of the data regarding the environmental variables relevant to the harvesting subsystems (e.g. solar radiation, wind speed, etc.) measured in a certain time interval in the site of interest, as well as the expected power consumption profile of the load system (e.g. a system which periodically becomes active, with a known duty cycle). On the basis of these input data and of the operating parameters specified for the harvesting system (like voltage thresholds, device parameters, etc.), the framework determines the system behaviour together with the current and voltage waveforms in the most relevant nodes of the circuit.

The program is very useful to plan the actual deployment of the harvesting system and it is able to anticipate the harvester performance in a particular operating environment with adequate accuracy, along with the dependencies on system parameters (e.g. the capacity of the supercapacitors, the voltage thresholds in the battery management subcircuits, the connection of an additional harvesting subsystem, etc.).

To aid the reader in understanding the system behavior detailed in the previous section and to report an example of the simulator capabilities, we used the simulation script described above to generate the plots shown in Figure 40.

The meteorological data considered for this simulation have actually been gathered on October 24, 2007 at the Grand-St-Bernard pass, at 2400 m above sea level between Italy and Switzerland. These data and the system parameters have been expressly set to make the simulated system perform the highest possible number of transitions, to highlight its operation. As shown in Figure 40a and Figure 40b, the selected day was quite windy and cloudy. To further reduce the impact of the solar harvesting subsystem, the PV panel size has been lowered to just 60 cm^2. The starting voltage across the supercapacitors at the output of the wind harvesting subsystem ($C_1 = 1\,\mathrm{F}$) and of the solar harvesting subsystem ($C_2 = 50\,\mathrm{F}$) have been set to unlikely values, i.e. rather lower than the voltage across C_0 (see the left of Figure 40e). V_i has been set to 2 V, while the system to be powered consumes 100 mW for 1 s every 30 s, and has a standby power of 0.1 mW.

The waveforms on Figure 40e permit to distinguish the changes in the harvester operation. At the start of the simulation, during T_1, C_1 and C_2 are quite discharged with respect to C_0, so they cannot provide any energy to the main reservoir. This causes the battery to activate, and to sustain alone the power consumption of the load: a steady current flows outside the battery (Figure 40d), and the battery discharges linearly (Figure 40f).

At the end of T_1 the wind appears, and C_1 recharges until when it can provide some energy to C_0. During T_2 only the power coming from the wind harvesting subsystem is present, but it is not enough to sustain alone the whole power needs of the load (indeed in Figure 40c the harvested power remains on average below the average output power level). So the battery intervention is still required and the battery continues discharging.

Before the end of T_2, the sun appears and C_2 starts charging. However, even if the total harvested power exceeds the output power, just a part of it can be relayed to C_0, because C_2 has not reached the level of C_0 yet. So, before the end of T_2, the harvested power going to C_0 is still coming from the wind subsystem only, and this determines the spike observable in Figure 40e around the 9th hour. During T_3, V_a increases because of significant wind flow: the wind energy is sufficient to keep V_a above V_i, so the battery stops delivering current. V_a continues increasing thanks to the wind flow until it reaches $V_B + 100\,\mathrm{mV}$: the recharge process starts and during T_4, C_0 keeps recharging the battery in a pulsed way. However, the average recharge current is low, because the energy excess provided by the wind subsystem is quite low.

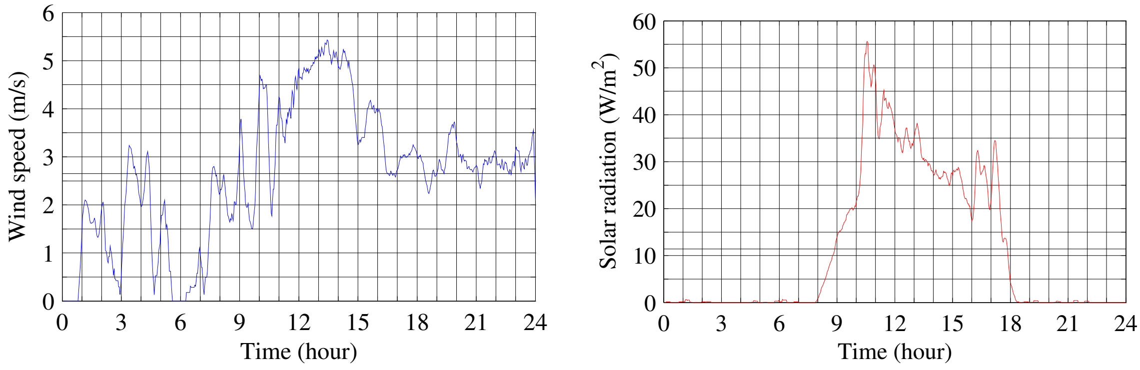

(a) Wind speed

(b) Solar radiation

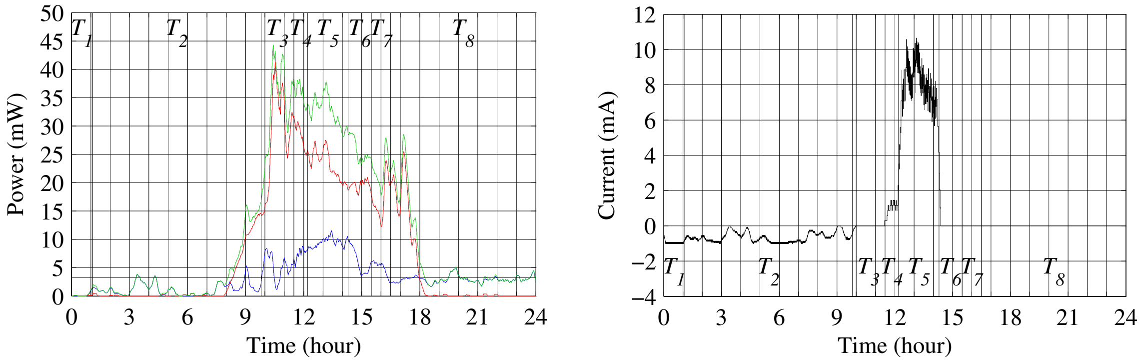

(c) Harvested power

(d) Battery charge current

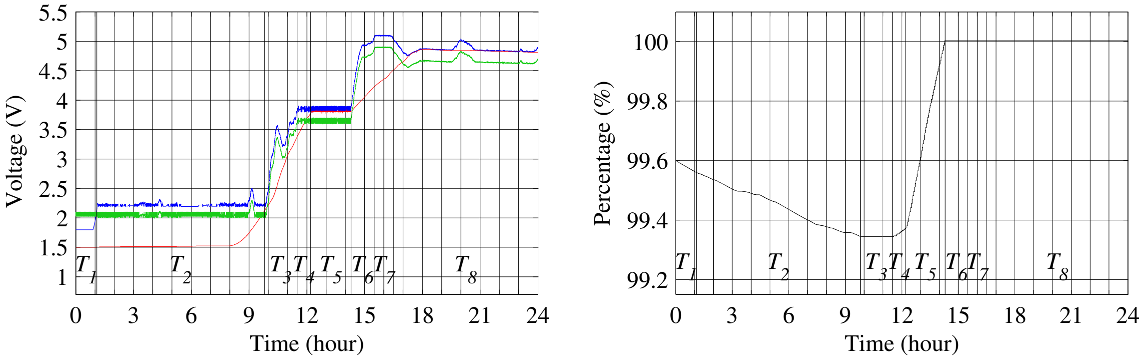

(e) Voltage across supercapacitors

(f) Battery charge

Figure 40. Plots resulting from the system simulation in Matlab. (a) Wind speed data collected on October 24, 2007 at the Grand-St-Bernard pass [62] (dashed: average value). (b) Solar radiation data collected on October 24, 2007 at the Grand-St-Bernard pass [62] (dashed: average value). (c) Power harvested by each of the two energy harvesting subsystem (blue: wind - red: solar), their sum giving the total harvested power (green), and the average output power consumed by the load (dashed). (d) Current flowing inside (outside) the battery, when positive (negative). (e) Waveforms of the voltages across the supercapacitors present in the system (blue: across C_1 (wind) – red: across C_2 (solar) – green: across C_0). (f) Battery charge, in percentage.

When C_2 reaches the level of C_0, both harvesters contribute to the recharge of the battery, during T_5. At the end of T_5, the battery is fully charged, and the overcharge protection circuit U_1 prevents the battery from further charging. For this reason, during T_6, V_a is free to increase above the battery level. At the start of T_7, V_a reaches the Zener diode threshold, so the energy in excess coming from the harvesting subsystems is wasted on D_0. Finally, during T_8, input and the output power levels are very similar, thus V_a remains quite steady.

5.6 CONCLUDING REMARKS

In this chapter we have presented an effective multi-source, multi-storage energy harvesting architecture. Its straightforward, fully analogue design based on ultra-low-power components makes it a very efficient and cost-effective solution to enable the autonomous operation of low power applications. Its modular design and power ORing strategy permits to harvest ambient energy from an arbitrary number of different sources through hot-pluggable harvesting subsystems. The possibility of collecting energy from a high number of different generators improves the system reliability by reducing the impact of the availability variations affecting each energy source. The system, based on supercapacitor, can also accommodate a rechargeable battery, to ensure a continuous power supply to the load system even during long periods of ambient energy shortage. The battery is protected from overcharges and undercharges, and is recharged when the operating environment provides more power than required by the load.

The implemented harvesting system has been presented along with an expressly developed simulation framework. It enables the designer to assess the harvester suitability to a certain application through simulating the system behavior in realistic operating conditions, specified for example by meteorological data or by the power profile of the system to be powered. Finally, this tool is also useful to evaluate the effects of different system parameters on the system overall performance.

6 GRID-ASSISTED PV POWER SUPPLY FOR GSHP SYSTEMS

In recent years the diffusion of distributed generation systems has undergone a considerable growth, driven by their increasing cost-effectiveness and by more stringent regulations on energetic efficiency of buildings. The study discussed in this chapter jointly addresses two major issues, affecting two of the highest-market-potential microgeneration technologies: the high running costs of ground-source heat pump (GSHP) systems, and the forthcoming unprofitability of feeding into the grid the electricity generated by small-sized photovoltaic (PV) arrays, frequently installed on residential and commercial buildings. To take advantage of the availability of both technologies in the same building, a novel power supply system is presented, aimed at fulfilling the GSHP electricity requirements by self-consuming all the energy generated by the solar array, and complementing it with mains electricity. After an in depth analysis of the supply system architecture and operation, power consumption profiles resulting from the simulation of a real GSHP are investigated. Beyond highlighting primary design issues of such integrated system, this study demonstrates the suitability of the proposed solution to enhance self-sustainability of GSHP systems, and its instrumentality in reducing the consumption of non-renewable energy for cooling purposes in tropical and subtropical climates.

6.1 INTRODUCTION

6.1.1 Ground-source heat pump systems

Ground-source heat pump (GSHP) systems constitute one of the most promising technologies to provide thermal comfort in an environmentally sustainable way. Space heating and cooling currently account for 68 % of the annual energy consumption of a European household, and about 88 % of this energy comes from non-renewable energy sources [63, 64]. In order to reduce the global ecological footprint, it is paramount to lower these figures through the adoption of greener heating, ventilation and air conditioning (HVAC) equipment, and the wide application of sustainable architecture principles.

Energy requirements of a GSHP system usually subdivide as follows: about 75 % of the energy is collected from the environment (i.e. from the ground), whereas the remaining 25 % must be provided as electric energy [65]. Supplying the latter through the conventional power grid has two major drawbacks. Firstly, just 20 % of electrical energy in Europe is produced by renewable energy sources, so the share of renewable primary energy in the consumption of a grid-powered GSHP system cannot exceed 80 % [66]. Besides, considering the electric power consumption of this kind of systems compared to common household appliances, powering a heat pump with grid electricity can be rather expensive. Pricing systems adopted by Italian electric companies, for example, penalize heavy household consumption (the price per kWh increases with increasing total consumption) with the view to discouraging energy wasting, without considering that large part of it may be due to the adoption of low environmental impact equipment such as heat pumps [67, 68].

In the light of these considerations, supplying a GSHP system with electricity locally produced by means of a microgeneration equipment becomes an attractive option, as it allows to cut down both the running costs and the environmental impact of this space conditioning solution.

6.1.2 PV electricity: current trends

In the context of residential and commercial buildings, photovoltaic (PV) systems are currently the most widespread technology for distributed generation of renewable electricity. Owing to the provisions of the incentive policies put into effect by many countries to promote the adoption of PV systems, most present PV installations are designed to feed into the grid either all of the produced energy, or just the portion exceeding local instantaneous consumption. Both these schemes use the grid as energy buffer, to temporally decouple the energy generation and consumption stages. At the present time, this approach is progressively losing its attractiveness, for both technical and economic reasons. From a technical standpoint, distributed production of renewable electricity from fluctuating environmental energy sources causes intermittent and rather unpredictable energy flows being fed into the grid: when the contributions of this kind grow beyond a certain threshold, serious imbalances between power supply and demand are likely to occur, jeopardizing grid stability [69, 70]. Besides, profitability of such schemes is strongly dependent on the relation between the price the utility pays for the fed-in energy, and the grid electricity rates. Due to the favorable feed-in tariffs introduced by many countries as part of

PV incentive policies, the value of fed-in energy currently exceeds that of the energy purchased from the grid. As a consequence, selling all the locally produced electricity to the electric utility is often the most convenient option, for the time being. However, the natural degression of feed-in tariffs combined with the steady rise in grid electricity rates are expected to reverse the relation between these values within a few years time span: Figure 41, which presents the progression of these quantities for the German case, clearly highlights this trends.

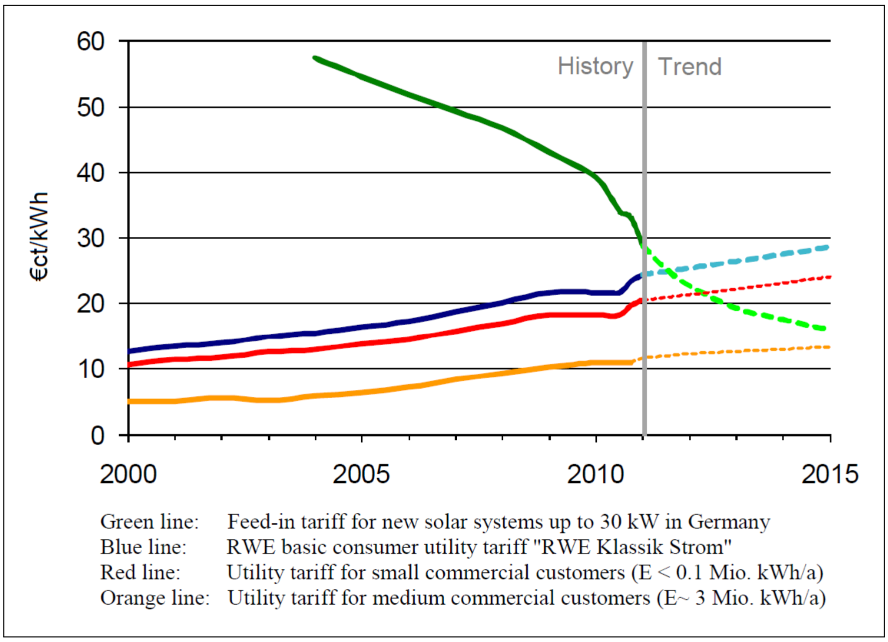

Figure 41. Comparison of utility rates and feed-in tariffs for solar electricity in Germany. Source: [71].

One of the most promising techniques to address both these issues is to shift the assignment of the energy buffering task from the utility grid to local energy storage devices (such as rechargeable batteries), embracing a paradigm typical of stand-alone systems. The advantage of this choice becomes evident when comparing the two plots in Figure 42. Both graphs report the typical power consumption profile of a four-person household in Germany, and the power generation profile of a 5 kWp PV plant [72]. Figure 42a shows how the power coming from the PV plant is employed in a classic grid-connected system. Just a fraction (approximately 30 %) of the PV power is consumed directly (so called *natural* self-consumption), while most of it is fed into the grid. Grid electricity then fulfills the household power needs during the consumption peak in the evening, and during the night.

Figure 42b shows instead how the PV power can be managed in presence of a local energy storage. During daylight hours, beyond

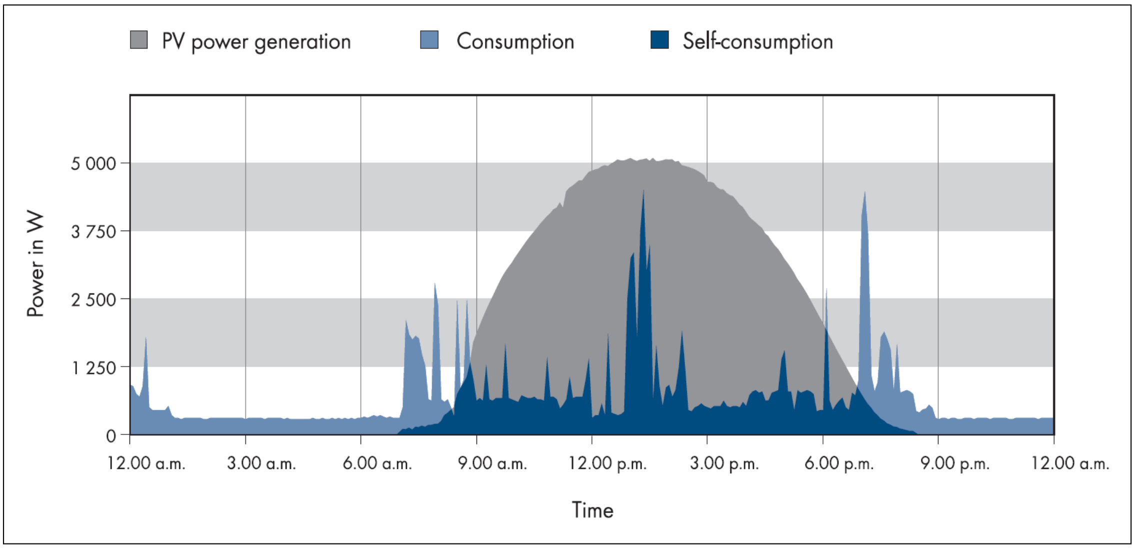

(a) Grid-connected PV system *without* local energy storage

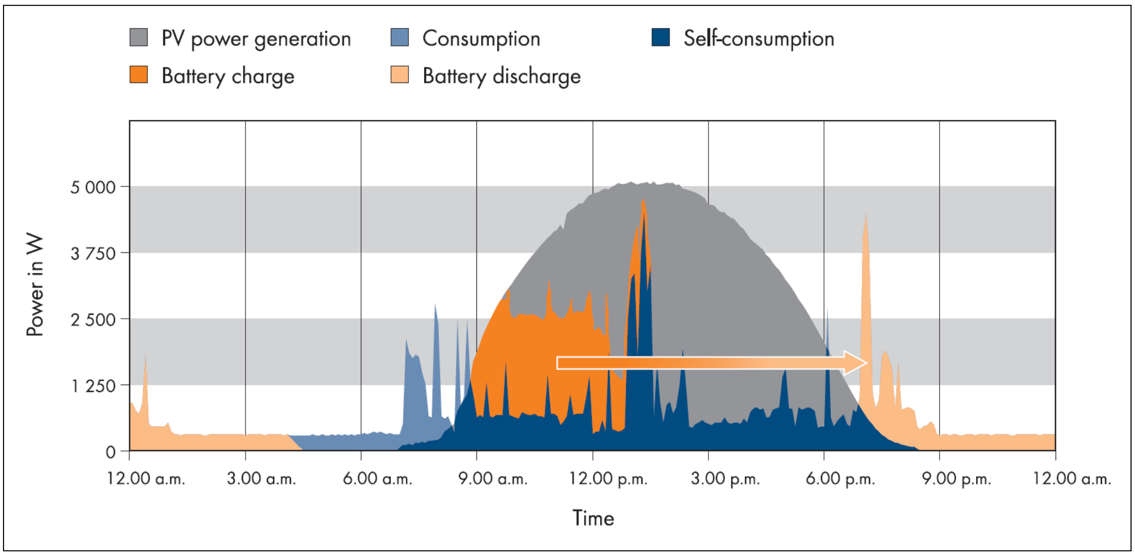

(b) Grid-connected PV system *with* local energy storage

Figure 42. Daily profiles of the power generated by a 5 kWp PV plant, and of the power consumed by a four-person household in Germany, highlighting the differences in the management of the PV energy in (a) absence or (b) presence of a local energy storage. Source: [72].

natural self-consumption, a significant part of the PV energy is now stored on the spot (the percentage depends on the capacity of the local storage), and can be employed to cover a large portion of the household power needs when the natural self-consumption is no more available. This allows to minimize the interactions with the utility grid, to keep the value of the locally generated energy always equal to that of grid electricity [73]. Thanks to these features, there is a growing interest in distributed generation solutions implementing self-consumption strategies, both in research and commercial fields [74, 75]. At present, few countries actively foster self-consumption of PV electricity through their incentive schemes, but more are expected to follow current trendsetters, which are Germany, Italy and United Kingdom [76, 77].

6.1.3 Contributions

This work investigates a novel integration strategy between GSHP and PV technologies, with the aim of making the most of their joint adoption within a single residential or commercial building. Focusing on this particular category of buildings and of inhabitants, it often happens that restrictions on physically accessible space or on available budget compel to install solar arrays of just few square meters. In this case, instead of setting up the PV system to feed the generated energy into the grid (which would require to enter into a contract with a local electric company, to certify the system compliancy to all relevant safety regulations, etc.), employing all produced electricity to supply a single, power-greedy domestic load, such as a GSHP system, can prove to be a cost-effective and straightforward solution.

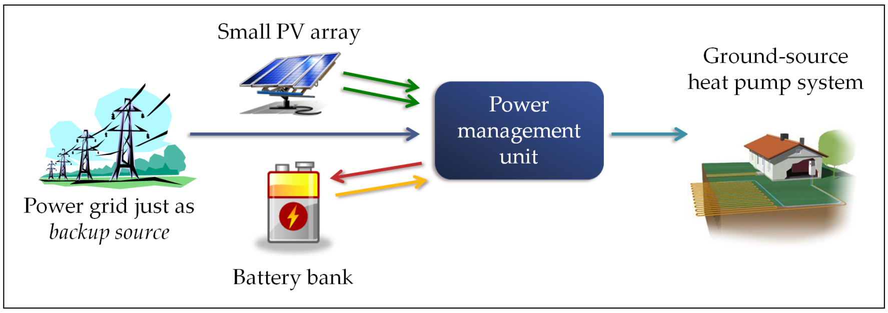

Figure 43. Qualitative diagram of the proposed power supply architecture.

This is precisely the purpose of the power supply system presented in this chapter, which has been designed to entirely fulfill the electricity requirements of a GSHP system by self-consuming all the energy generated by an on-site solar array, and complementing it with mains electricity. According to latest trends in distributed generation systems, all the energy produced by PV modules is either consumed directly or stored in a battery bank for usage at a later time: the proposed supply architecture, in its purest version, does not feed any energy into the grid, and behaves like a common electric load towards it (Figure 43). A multiple input, single output flyback converter has been chosen to efficiently combine the energy coming from the three energy sources (grid, solar array, and battery bank), which can thus contribute to the power supply of the GSHP system in an independent and concurrent way. The state machine implemented by the control circuit is designed to give the maximum priority to the usage of the energy coming from the PV array, while assigning a lower priority to the battery bank, and the lowest priority level to mains electricity. As a result, this system layout is able to combine the benefits of an enhanced self-consumption strategy with the reliability of conventional grid-powered supply systems.

In the following Section 6.2, an in depth analysis of the proposed architecture and of its operation modes will be presented, with focus on key design tradeoffs. Subsequently, the results of specific studies on power consumption profiles of real GSHP systems will be discussed in Section 6.3, to both verify the suitability of this power supply system to the intended scope of application and to highlight primary points of attention which should be taken into account during the preliminary design phase of such integrated space conditioning solution.

6.2 POWER SUPPLY SYSTEM

The diagram of the proposed power supply is shown in Figure 44.

6.2.1 Architecture

The system inputs are a single-phase ac line (common in residential and commercial buildings), a solar array, and a battery (or a battery bank). The system output is the electric system to be powered, which can be either a dc load (option 1) or an ac load (options 2 and 3). Before being fed to the following power processing block, the grid ac voltage is rectified by the rectification (ac/dc) and power factor correction (PFC) stage. This circuit can be implemented with passive or active devices, according to the power handling and efficiency requirements set by the specific application. The presence of this stage ensures a unidirectional energy flow, from the grid to the power supply.

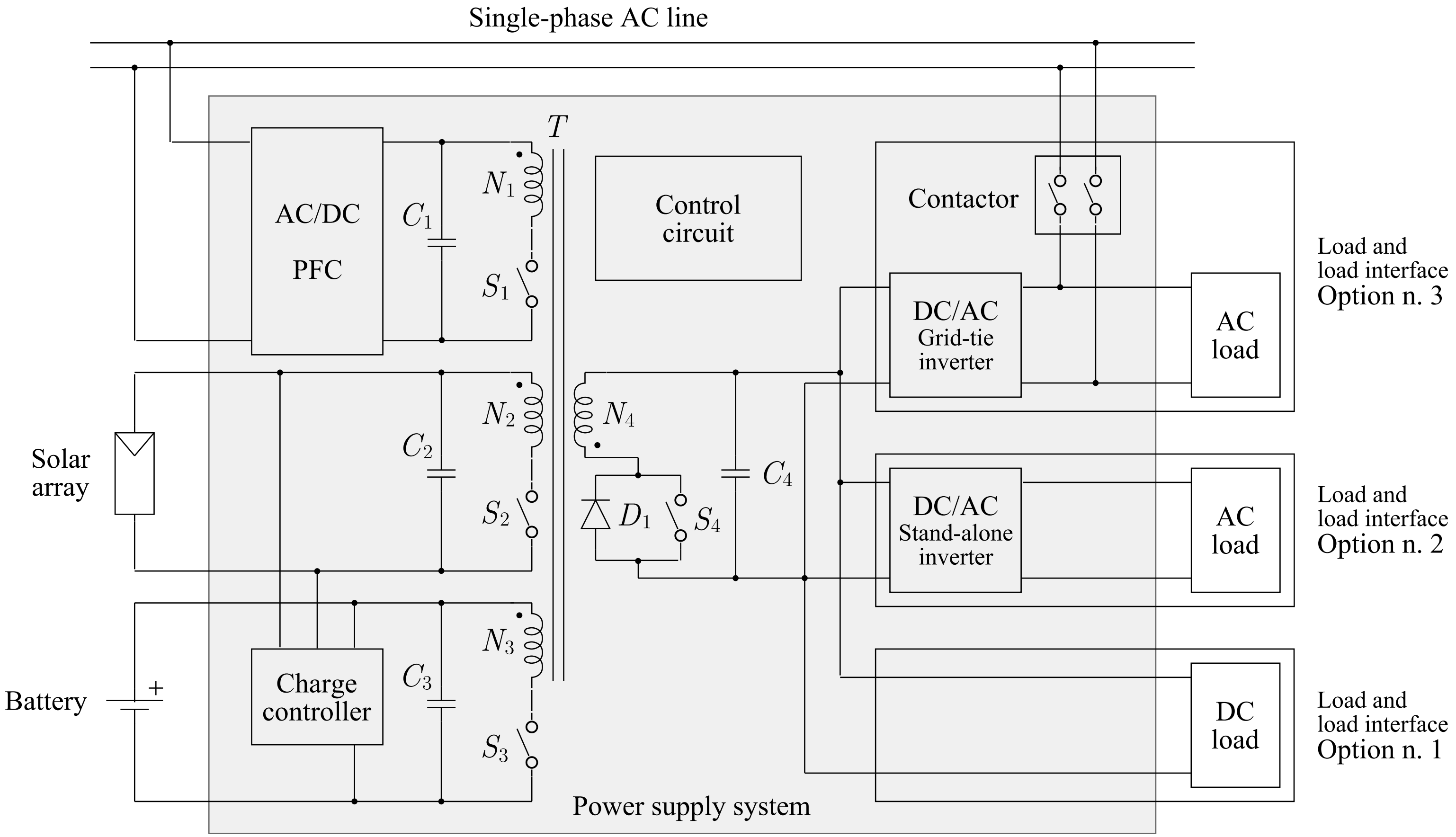

Figure 44. Schematic diagram of the proposed power supply system, with three alternatives for the load and the load interface.

The core functional block of the architecture is the multiple-input flyback converter. Each of the switch couples (S_1, D_1), (S_2, D_1), and (S_3, D_1) constitutes a conventional flyback converter, so the multiple-input converter can be thought as three single-input converters sharing the same secondary side. By driving each converter in an interleaved way with the others, all energy sources can potentially supply current to the load at each switching cycle of the multi-input converter, without interfering with each other. This topology allows to get energy from all sources at virtually the same time, regardless of how low the voltages on the primary sides can be. An in-depth analysis of the operation of such converter can be found in [78].

Switches S_1, S_2, S_3 and S_4 can be implemented with either MOSFETs or insulated-gate bipolar transistors (IGBTs): the choice must be done in relation to the power handling and switching frequency requirements set by the application. Switch S_4 is intended to work as a synchronous rectifier, so it must be activated when D_1 is on in order to reduce the diode conduction losses [79]. Capacitors C_1, C_2, C_3 and C_4 are needed to smooth out the steep current waveforms at all converter ports. Actual implementation of the converter probably requires a snubber circuit in parallel with each of the three windings on the transformer primary side. By properly selecting turn ratios N_1:N_4, N_2:N_4 and N_3:N_4 and the timings of the interleaved driving waveforms for switches S_1, S_2 and S_3, it is possible to accommodate solar arrays and batteries with various characteristics [80]. A charge controller can let the solar array to safely recharge the battery, when the power budget of the whole system allows it.

According to the specific application, there are three options for the load interface. 1) If the load operates on dc voltage and there is no need to feed surplus energy back to the grid, then a direct connection between the converter output and the load is the most efficient solution. 2) If the load operates on ac voltage and there is no need to feed surplus energy back to the grid, then a stand-alone inverter must be interposed between the converter output and the load. 3) If the load operates on ac voltage and feeding surplus energy back to the grid is desired, then a grid-tie inverter must be used to connect the converter output to the load, and a contactor must be added to let excess energy flow back to the grid. The choice of feeding the surplus energy back to the grid or not depends on the mismatch degree between the power generation profile of the solar array and power consumption profile of the load. Further details on this topic will be provided in the next section.

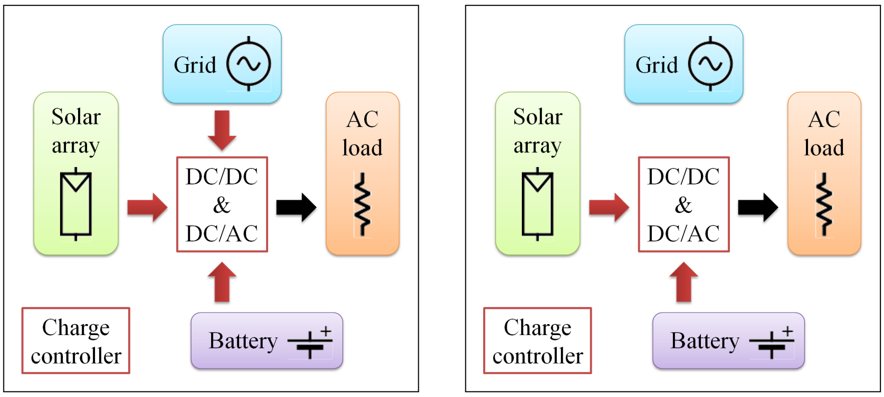

(a) Grid-assisted mode

(b) Self-sufficient mode

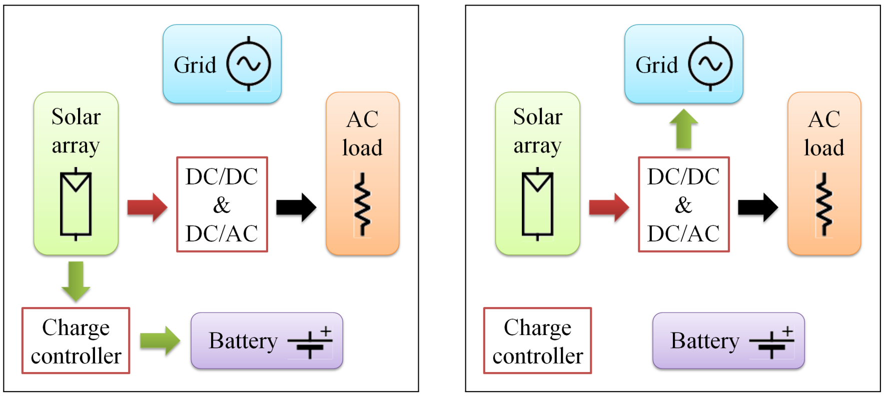

(c) Battery charging mode

(d) Grid supply mode

Figure 45. Schematic representation of power flows in the different operation modes of the proposed power supply. Grid supply mode is available only if the system adopts the load and load interface option n. 3 (see Figure 44).

The control block supervises the operation of each subcircuit, and manages the transitions between operating modes. Using voltage and current sensing devices, it can estimate in real-time the power generated by the solar array and that drawn by the load system, and adapt the circuit operation accordingly, calculating also how much energy must be taken from the grid and/or from the battery to regulate the output voltage on C_4. One of its tasks is to perform the maximum power point tracking (MPPT) of the solar array, by adjusting the switching time of S_2 and the activation time of the charge controller. If option n. 3 is selected for the load interface, the control block is also in charge of the inverter synchronization with the grid frequency, and of the contactor activation.

6.2.2 Operation

The operating modes of the proposed power supply are depicted in Figure 45. Let $p_L(t)$ be the instantaneous power consumed by the load system, $p_G(t)$ the instantaneous power supplied by the grid to the load, $p_{PV}(t)$ the instantaneous power generated by the solar array, $p_{BI}(t)$ the instantaneous power supplied to the battery by the solar array through the charge controller, and $p_{BO}(t)$ the instantaneous power supplied by the battery to the load system. Note that $p_{BI}(t)$ can never exceed a certain value $p_{BI}^{\max}(t)$: when the battery is not full, $p_{BI}^{\max}(t) = P_{BI}^{\max}$ due to the battery maximum charge rate; when the battery is full, $p_{BI}^{\max}(t) = 0$. Likewise, $p_{BO}(t)$ can never exceed a certain value $p_{BO}^{\max}(t)$: when the battery is not empty, $p_{BO}^{\max}(t) = P_{BO}^{\max}$ due to the battery maximum discharge rate; when the battery has no residual energy stored, $p_{BO}^{\max}(t) = 0$.

(a) *Grid-assisted mode*: when $p_{PV}(t) < p_L(t)$ and $p_{PV}(t) + p_{BO}^{\max}(t) < p_L(t)$, the grid must contribute providing the missing part of the energy needed to fulfill the load power consumption. In this mode the number of active energy sources can range from one (the grid alone) to three (if both the solar array and the battery can provide some energy).

(b) *Self-sufficient mode*: when $p_{PV}(t) < p_L(t)$ but $p_{PV}(t) + p_{BO}^{\max}(t) > p_L(t)$, the solar array and the battery can supply the load without the help of the grid. However, the energy coming from the solar array is not enough to recharge the battery. In this mode the active inputs to the converter can only be the solar array and the battery.

(c) *Battery charging mode*: as soon as $p_{PV}(t) > p_L(t)$, the solar array can supply the load alone. Besides, if the battery is not fully charged, it can recharge the battery with power $p_{BI}(t) = p_{PV}(t) - p_L(t)$. In case $p_{PV}(t) > p_L(t) + p_{BI}^{\max}(t)$, if load interface option n. 3 has been chosen, the contactor can be activated to let the excess PV energy flow into the grid. In this mode two of the three inputs of the converter are inactive, so the converter operation is identical to that of a single-input flyback converter.

(d) *Grid supply mode*: if option n. 3 is selected for the load interface, when the battery is fully charged and $p_{PV}(t)$ is still greater than $p_L(t)$, then the contactor can be activated, and the energy not consumed by the load is fed into the grid. In this mode the converter works exactly as in *Battery charging mode*.

6.3 CASE STUDY: GSHP SYSTEM

To verify the suitability of the proposed power supply system to the intended scope of application, assess its effectiveness, and identify primary design issues, a specific study on power consumption profiles of a real GSHP system has been made.

6.3.1 Simulation scenario

In order to get realistic data on this subject, the GSHP system simulation framework presented in [81] has been employed. Starting from data about the building, the geographical location, the space conditioning system and its activation policy, the program calculates the value over time (with a resolution of 1 h) of many parameters concerning the heat pump operation, during the year. Thanks to this software, the electricity consumption of the heat pump and of the circulating pump can be determined as well, with good accuracy.

In the considered simulation scenario, the building is a medium-sized house, with an indoor volume of 400 m^3, located in an Italian city with a humid subtropical climate. The house is supposed to have a very good energy performance, with a maximum energy requirement in heating around 13 kWh/(m^3 year) in the said location. The heat pump system is coupled to a closed-loop horizontal ground heat exchanger, and is programmed to ensure a preset indoor temperature of 20 °C during winter and of 26 °C during summer. The heat pump works according to a hourly schedule, which is different for workdays and for the weekend, consistently with the expected occupancy of the house. The full list of the values adopted for the simulation parameters is reported in Table 4.

6.3.2 Hourly profiles analysis

Two samples of the simulation results are shown in Figure 46 and Figure 47. The plots present the hourly power consumption of the GSHP system over a time span of two days, during heating operation in wintertime and cooling operation in summertime, respectively. The narrowness of the deviations of indoor temperature from the target values proves the suitability of the considered activation schedule, in both space conditioning modes. However, the intermittent activation of the heat pump causes slightly high peaks in electric power consumption, reaching 1.2 kW in winter and 450 W in summer. These values are fundamental to the design of the power supply system, as they set specific

Table 4. Simulation parameters for the considered scenario

Parameter	Value
Building	
Building type	Terraced house
Indoor building heated volume	$400\,\mathrm{m}^3$
Building surface for heat transfer to indoor building heated volume ratio (shape ratio)	$0.5\,\mathrm{m}^{-1}$
Full equivalent transmittance related to energy performance and climate zone of the building	$1\,\mathrm{W/(m^2\,K)}$
Indoor building heated volume to wall volume ratio	0.3
Wall density	$900\,\mathrm{kg/m^3}$
Wall specific heat capacity	$1200\,\mathrm{J/(kg\,K)}$
Indoor target temperature during wintertime	$20\,°\mathrm{C}$
Indoor target temperature during summertime	$26\,°\mathrm{C}$
Ground-source heat pump system	
Ground heat exchanger type	Closed loop, horizontal flat panel
Refrigerant	R-134a
Ground heat exchanger depth underground	$2.49\,\mathrm{m}$
Compressor irreversibility coefficient	80%
Condenser heat transfer coefficient	85%
Running COP (coefficient of performance)	$3.0 \div 4.8$
Morning operating hours, Monday to Friday	5 AM – 9 AM
Evening operating hours, Monday to Friday	5 PM – 10 PM
Operating hours, Saturday and Sunday	7 AM – 11 PM
Climate zone	
Location	Ferrara, Italy
Heating degree days	2326 degree days
Daily maximum temperature, yearly maximum	$38\,°\mathrm{C}$
Daily maximum temperature, yearly minimum	$6\,°\mathrm{C}$
Daily minimum temperature, yearly maximum	$28\,°\mathrm{C}$
Daily minimum temperature, yearly minimum	$-5\,°\mathrm{C}$
Underground temperature range (depth: $2.5\,\mathrm{m}$)	$10\,°\mathrm{C} \div 19\,°\mathrm{C}$
Heating operation period	Oct. 15th – Apr. 30th
Cooling operation period	Jul. 1st – Sep. 30th

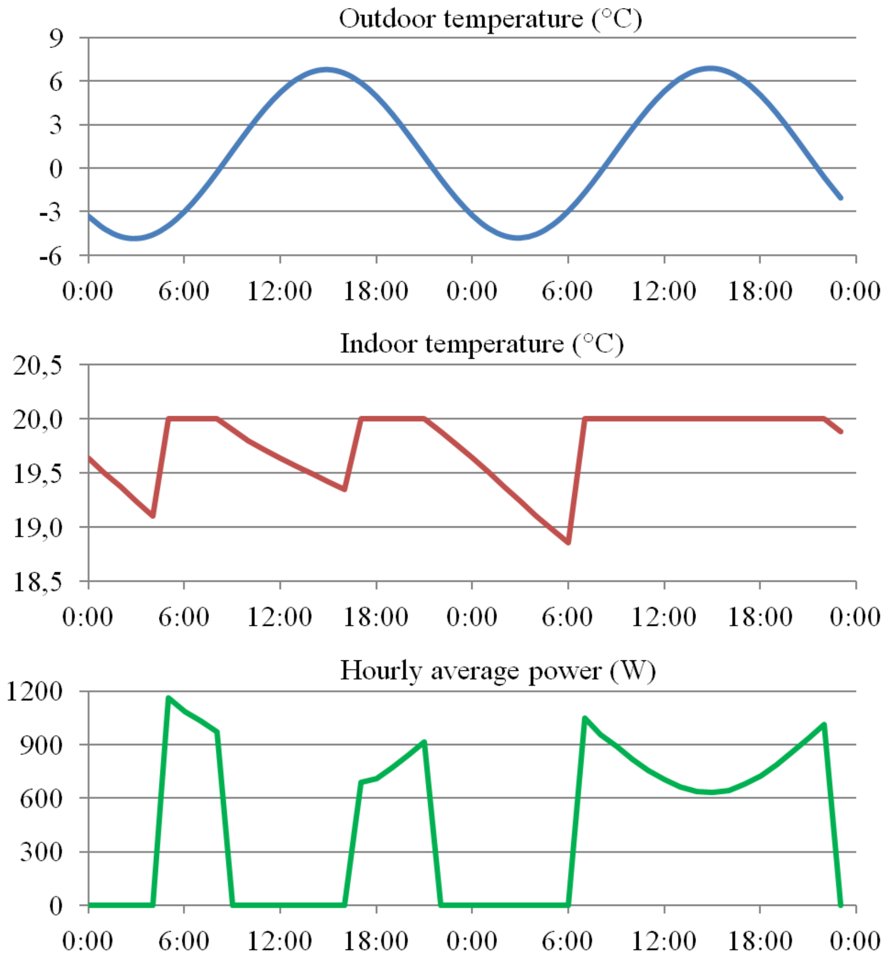

Figure 46. Simulation outcomes for two consecutive days (Friday and Saturday) during the coldest period of the year (end of January): outdoor temperature, indoor temperature, and hourly average power consumption of the considered GSHP system in heating mode.

requirements on the instantaneous power handling capabilities of the circuit.

6.3.3 Annual profile analysis

Further considerations on the sizing and the design of the power supply system can be made by comparing the annual power consumption profile of the GSHP system with that of a PV array installed on the same building served by the heat pump. These data are plotted in Figure 48. In the considered simulation scenario, heating proves to be the most power consuming operating mode, with daily peaks in energy usage up to 13 kWh during the coldest period of the year. In summer, daily

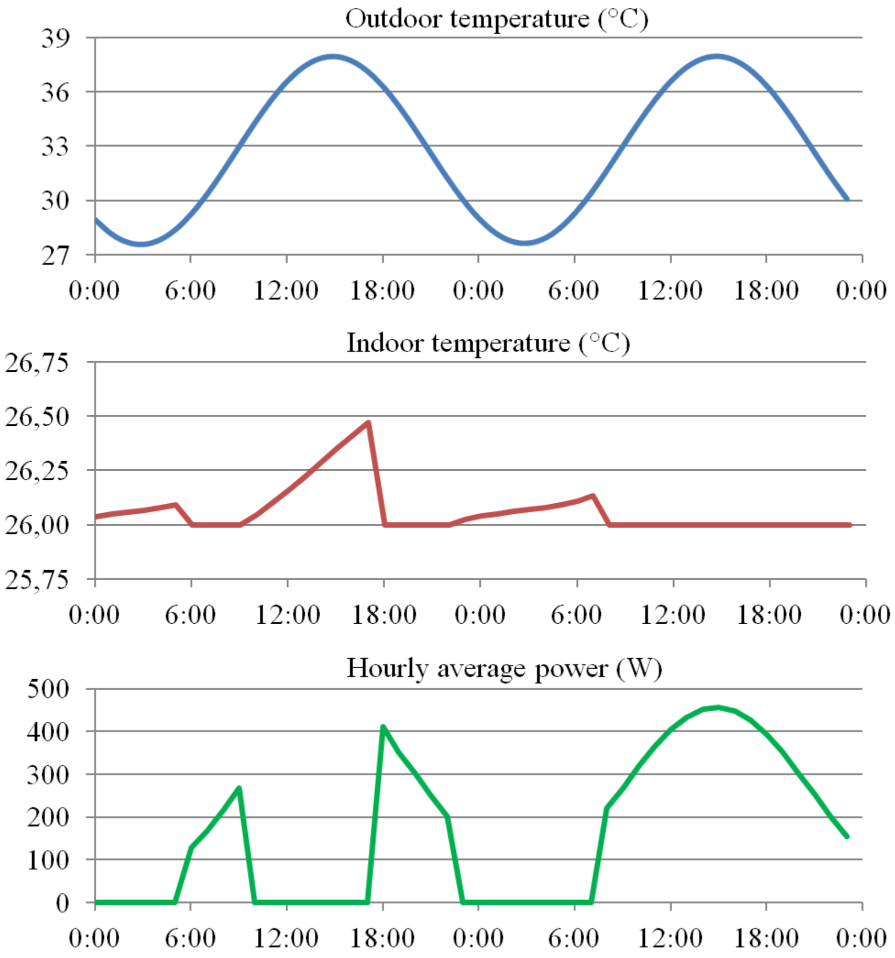

Figure 47. Simulation outcomes for two consecutive days (Friday and Saturday) during the hottest period of the year (beginning of July): outdoor temperature, indoor temperature, and hourly average power consumption of the considered GSHP system in cooling mode.

peaks are at least 50 % lower than in winter. The mismatch between generation and consumption curves turns out to be fairly considerable. The correspondence of the period of maximum generation with a local maximum in the consumption curve is a good feature, however two unfavorable circumstances can be identified: 1) throughout the winter, the solar array is able to supply just a fraction of the needed power, and 2) during spring and autumn the PV system generates much more energy than that required by the heat pump.

In such a situation, sizing the solar array to ensure it can supply the heat pump by itself during summer can be a cost-effective design choice, and suitable to allow the installation of the PV modules on the same building. Taking into account that energy demand is higher dur-

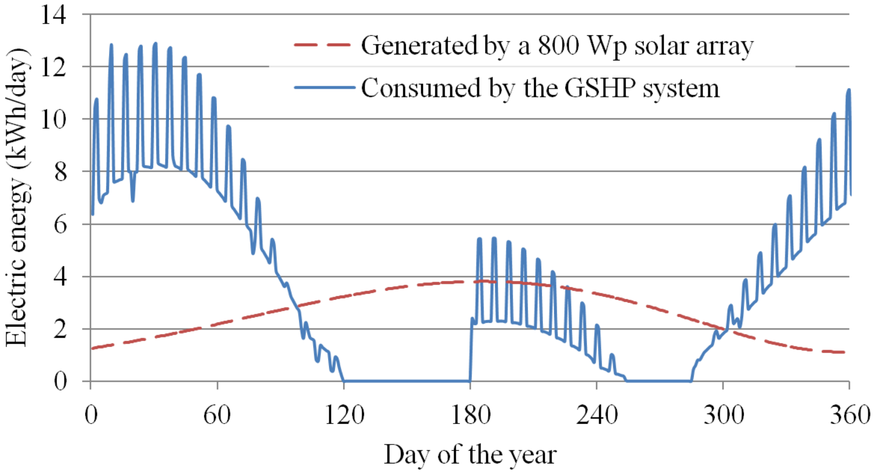

Figure 48. Comparison between the annual profile of the daily electricity consumption of the considered GSHP system, and the expected energy generation profile for a 800 Wp solar array (South oriented, tilt angle 30°) installed on the roof of the same building served by the GSHP system.

ing weekends, and for the purpose of keeping the cost of the PV array as low as possible, the weekly peak in electricity consumption can be considered as the reference value for the system sizing, instead of the daily one: this would require a slight increase in the capacity of the battery bank, to enable the storage of more energy throughout the week to build up a reserve for the weekend.

Focusing on the scenario considered for this simulation, for example, the maximum weekly energy consumption in summer occurs in the first week of July, when about 22.3 kWh are spent for air conditioning. To fully meet this weekly energy requirement, a 800 kWp solar array can suffice, as it would produce about 26.8 kWh in the same period: the generation of 20 % more energy than strictly necessary allows for the intrinsic losses of the power supply system. With an area requirement ranging between 7 m^2 and 8 m^2 (according to the technology of the PV panels), the implementation of a PV plant with such a size should be rather affordable, both in terms of initial investment and of compatibility with building-integrated photovoltaic (BIPV) solutions [82, 83].

There are two alternatives to make a profitable use of the electricity generated during the extended periods of heat pump inactivity, occurring in spring and autumn. One is to use the load interface option n. 3, as presented in the previous section: this enables to feed the energy not used by the heat pump into the grid of the building, where it can be consumed by other domestic appliances, or sold to the electric utility (this would require to enter into a contract with the electric utility). A more attractive alternative is to use this energy surplus to make the heat pump perform a so called *seasonal storage* of heat in the ground. It is possible for this systems to store energy in the ground over the summer months, when heating loads are minimal, and to retrieve this energy during the winter months, when higher loads occur. The energy stored in the ground increases the overall performance of the system, as well as the coefficient of performance of the heat pump [84, 85].

It is important to highlight that all relevant design choices presented so far are strictly related to the climate zone under investigation. According to the location of the building, the GSHP consumption profile can vary significantly, along with the relative repartition of heating and cooling loads. In countries belonging to subtropical or tropical regions, for example, cooling loads largely exceed heating ones: in those areas the power consumption profile of a heat pump would likely resemble the PV power generation curve, and nearly all the generated electricity could be consumed for air conditioning purposes, cutting down the annual demand for mains electricity.

6.4 CONCLUDING REMARKS

In this chapter a novel power supply system has been presented, aimed at reducing the running costs of a GSHP system by self-consuming all the renewable energy generated by a small-sized solar array, installed on the same building served by the heat pump. BIPV solutions are particularly suitable for this purpose.

Although the power supply architecture can be tailored to supply either an ac load or a dc load, working with the latter category allows to reach the maximum efficiency, as the inverter stage is not required in this circumstance. For the time being, there are very few heat pumps designed to operate on a dc power supply available on the market. However, with the progressive diffusion of dc microgrid implementations, more dc appliances are expected to appear.

The analysis of the electricity usage profiles resulting from the simulation of a real GSHP system has highlighted the most important design choices a designer should focus on. Hourly, daily and yearly energy consumption curves provide useful indications on the requirements of the power conversion circuit, the battery bank and the whole architecture, respectively.

The effectiveness of the proposed solution strongly depends on the considered climate zone. In tropical and subtropical regions, the joint adoption of GSHP systems and of this PV power supply system on a large scale could play a key role in cutting down the consumption of energy from non-renewable sources for air conditioning purposes. In case of significant mismatch between the annual generation and consumption curves, seasonal storage of thermal energy in the ground can prove a good solution to exploit all generated electricity.

CONCLUSIONS

The continuous advances in IC fabrication technologies, circuit design, and networking techniques enable the integration of an increasing number of functionalities in ever smaller devices. This trend determines the multiplication of possible application scenarios for tiny embedded systems such as wireless sensors, whose utilization has grown more and more pervasive. However, the operating life time of such systems, when placed in locations not allowing a wired connection to a dependable power supply infrastructure, is still heavily limited by the finite capacity of currently available accumulators, whose technology has not improved at the same pace of the electronic systems they supply.

Energy harvesting techniques constitute a real solution to power untethered computing platforms in this kind of spatially-distributed applications. By converting part of the energy freely available in the surrounding environment to electrical energy, the operating life of the system can be extended considerably, potentially for an unlimited time. In recent years an increasing number of researchers have investigated this possibility. The applications which can benefit from the implementation of energy harvesting techniques are very heterogeneous, as well as the topic of energetic self-sufficiency is of interest to a broad range of research fields. Thanks to the interdisciplinary vocation of the IMAMOTER-CNR institute which hosted me during the Ph.D. course, I had the opportunity to confront issues coming from various technical areas during my research activity, and to collaborate with several research institutions, universities and innovative companies at both national and international level.

In this dissertation we have discussed our results about the study and design of systems capable of harvesting energy from various regenerative sources. We started with the design of an airflow energy harvester, focusing on the optimization of its power generation and efficiency performances, and obtaining superior results with respect to similar works in literature. Then we dealt with the improvement of this architecture to implement a fully autonomous vibrational harvester, featuring uncommon in-the-field configuration capabilities. Afterwards we investigated the applicability of self-powered wireless sensor nodes to heavy duty and agricultural machinery, finding attractive vibration sources capable of providing enough power to sustain remarkable data transmission rates. To address remote monitoring applications with stringent needs in terms of power supply availability, we presented a truly flexible multi-source energy harvester, along with a simulation framework expressly developed to anticipate the harvester performance when placed in a specific operating environment. Furthermore, the design strategies allowing energy harvesters to fully exploit the locally generated power can be profitably applied in the field of distributed electricity generation from renewable energy sources, to enhance the self-consumption capabilities of microgeneration systems. Based on this motivation, we finally proposed a grid-assisted photovoltaic power supply to improve the self-sustainability of ground-source heat pumps, and analyzed original data on the consumption profiles of these innovative space-conditioning systems to assess the effectiveness of the design.

In conclusion, energy harvesting techniques have the potential to enable many cutting-edge applications, especially in remote sensing and pervasive computing areas, which can bring innovations in several fields of human activity. In this thesis we have contributed tackling some of the numerous open research challenges still hampering the widespread adoption of this technology.

A DIODE CONDUCTION LOSSES

Equation (15) has been proposed on page 29 to represent the conduction losses of the diode of a buck-boost dc/dc converter working in fixed-frequency discontinuous current mode (FF DCM), and is reported below for the reader's convenience.

$$P_{D,\text{cond}} = \frac{n\,V_t\,L\,I_{PK}^2}{2\,T\,V_O}\left[\ln\left(\frac{I_{PK}}{I_S}\right) - \frac{1}{2}\right] \tag{15}$$

This appendix details the original derivation of this equation.

A.1 ANALYTICAL MODEL

As shown in Figure 8, during T_2 time interval the diode is turned on and the current flowing through it decreases linearly over time (supposing that the V_O output voltage does not change during this time interval). This behavior can be expressed analytically with the following equation:

$$i_D(t) = I_{PK} - \frac{V_O}{L}t \tag{27}$$

The instantaneous power consumed by the diode is given by

$$p_D(t) = v_D(t)\,i_D(t) \tag{28}$$

When the diode is forward-biased, the relationship between diode voltage and current can be properly approximated with the following equation:

$$i_D(t) = I_S(e^{\frac{v_D(t)}{nV_t}} - 1) \tag{29}$$

where I_S is the reverse bias saturation current, $V_t = \frac{kT}{q}$ is the thermal voltage, and n is a constant whose value depends on the material and the physical structure of the diode [86]. From this equation the inverse relationship can be obtained:

$$v_D(t) = nV_t \ln\left(\frac{i_D(t)}{I_S} + 1\right) \tag{30}$$

which expresses the diode voltage as a funtion of the diode current.

Considering Equation (27) as the shape of the diode current, and using the just found relationship, the instantaneous power can be rewritten as

$$p_D(t) = nV_t \ln\left(\frac{I_{PK} - \frac{V_O}{L}t + I_S}{I_S}\right)\left[I_{PK} - \frac{V_O}{L}t\right] \quad (t \in T_2) \tag{31}$$

For the purpose of studying the power losses of the converter presented in Section 2.5.1 on page 26, the average power consumed by the diode during the switching period T is the most relevant quantity to determine. By definition, this is given by

$$P_{D,av} = \langle p_D(t)\rangle_T \triangleq \frac{1}{T}\int_{t_0}^{t_0+T} p_D(\tau)\,\mathrm{d}\tau \quad \text{with arbitrary } t_0 \tag{32}$$

By neglecting the power losses occurring when the diode is reverse biased (which are much smaller than those occurring when the diode is turned on), the latter equation can be reduced to

$$P_{D,av} \cong \frac{1}{T}\int_{T_2} p_D(\tau)\,\mathrm{d}\tau = \frac{1}{T}\int_{t_1}^{t_2} p_D(\tau)\,\mathrm{d}\tau \tag{33}$$

A good approximation of the dependance of the average power on the parameters of both the circuit and the device can be obtained by substituting the Equation (31) of the instantaneous power inside Equation (33):

$$P_{D,av} \cong \frac{1}{T}\int_{t_1}^{t_2} nV_t \ln\left(\frac{I_{PK} - \frac{V_O}{L}\tau + I_S}{I_S}\right)\left[I_{PK} - \frac{V_O}{L}\tau\right]\mathrm{d}\tau \tag{34}$$

The integration can now be performed. After applying the substitution

$$\alpha = I_{PK} - \frac{V_O}{L}\tau \qquad\qquad \mathrm{d}\alpha = -\frac{V_O}{L}\mathrm{d}\tau$$

it is possible to integrate by parts:

$$\begin{aligned}
P_{D,av} &\cong \frac{nV_t}{T}\int_{I_{PK}}^{0} \ln\left(\frac{\alpha + I_S}{I_S}\right)\alpha\left(-\frac{L}{V_O}\,\mathrm{d}\alpha\right) \\
&= \underbrace{-\frac{nV_tL}{TV_O}}_{=K}\int_{I_{PK}}^{0} \ln\left(\frac{\alpha + I_S}{I_S}\right)\alpha\,\mathrm{d}\alpha \\
&= K\left[\ln\left(\frac{\alpha + I_S}{I_S}\right)\frac{\alpha^2}{2}\right]_{I_{PK}}^{0} - K\int_{I_{PK}}^{0}\frac{\alpha^2}{2}\left(\frac{1}{\alpha + I_S}\right)\mathrm{d}\alpha \\
&= \underbrace{K\left[-\ln\left(\frac{I_{PK} + I_S}{I_S}\right)\frac{I_{PK}^2}{2}\right]}_{=G} - \frac{K}{2}\int_{I_{PK}}^{0}\frac{\alpha^2}{\alpha + I_S}\,\mathrm{d}\alpha
\end{aligned}$$

The following additional substitution can be applied

$$x = \alpha + I_S \qquad\qquad \mathrm{d}x = \mathrm{d}\alpha$$

to proceed with the integration:

$$\begin{aligned}
P_{D,av} &\cong G + \frac{K}{2}\int_{I_S}^{I_S+I_{PK}} \frac{x^2 + I_S^2 - 2xI_S}{x}\,\mathrm{d}x \\
&= G + \frac{K}{2}\left\{\left[\frac{x^2}{2} + I_S^2 \ln x\right]_{I_S}^{I_S+I_{PK}} - 2I_S(I_S + I_{PK} - I_S)\right\} \\
&= G + \frac{K}{2}\left\{\frac{I_S^2 + I_{PK}^2 + 2I_S I_{PK}}{2} - \frac{I_S^2}{2} + I_S^2\left[\ln(I_S + I_{PK}) - \ln I_S\right] - 2I_S I_{PK}\right\} \\
&= G + \frac{K}{2}\left[\frac{I_{PK}^2}{2} - I_S I_{PK} + I_S^2 \ln\left(\frac{I_{PK} + I_S}{I_S}\right)\right]
\end{aligned}$$

The substitution of the constant G with its expanded expression leads to

$$\begin{aligned}
P_{D,av} &\cong -K\frac{I_{PK}^2}{2}\ln\left(\frac{I_{PK} + I_S}{I_S}\right) + \frac{K}{2}\frac{I_{PK}^2}{2} - \frac{K}{2}I_S I_{PK} + \frac{K}{2}I_S^2 \ln\left(\frac{I_{PK} + I_S}{I_S}\right) \\
&= -\frac{K}{2}\left[\ln\left(\frac{I_{PK} + I_S}{I_S}\right)(I_{PK}^2 - I_S^2) - \frac{I_{PK}^2}{2} + I_S I_{PK}\right]
\end{aligned}$$

and by doing the same with constant K the final result can be obtained:

$$P_{D,av} \cong \frac{nV_t L}{2TV_O}\left[\ln\left(\frac{I_{PK} + I_S}{I_S}\right)(I_{PK}^2 - I_S^2) - \frac{I_{PK}^2}{2} + I_S I_{PK}\right] \tag{35}$$

This equation provides a good approximation of the power consumed on average by the diode of the converter described on page 26 as a function of the operating point of the circuit (determined by parameters T, L, V_O, I_{PK}, and V_t) and of the device characteristics (parameters n and I_S). The next section presents a method to determine the value of the latter two parameters for a real, specific device.

Finally, Equation (35) can be further simplified by taking into account that $I_S \ll I_{PK}$ in our application[1]

$$\begin{aligned}
P_{D,av} &\simeq \frac{nV_t}{2T}\underbrace{\frac{LI_{PK}}{V_O}}_{T_2} I_{PK}\left[\ln\left(\frac{I_{PK}}{I_S}\right) - \frac{1}{2}\right] \\
&= \frac{nV_t}{2}\frac{T_2}{T} I_{PK}\left[\ln\left(\frac{I_{PK}}{I_S}\right) - \frac{1}{2}\right]
\end{aligned} \tag{36}$$

and this is precisely the form of Equation (15) as presented on page 29.

---

[1] Typical I_S values are in the hundreds of nanoamperes (an example will be shown in the next section), whereas typical I_{PK} values in our application are in the tens of milliamperes. For example, considering an air flow speed of just 8.6 km/h and using the values $L = 330\,\mu\text{H}$ and $T_1 = 6.5\,\mu\text{s}$ resulting from the simulations presented in Section 2.5.1 on page 30, a value of about 20 mA can be calculated for I_{PK} with Equation (7) on page 28.

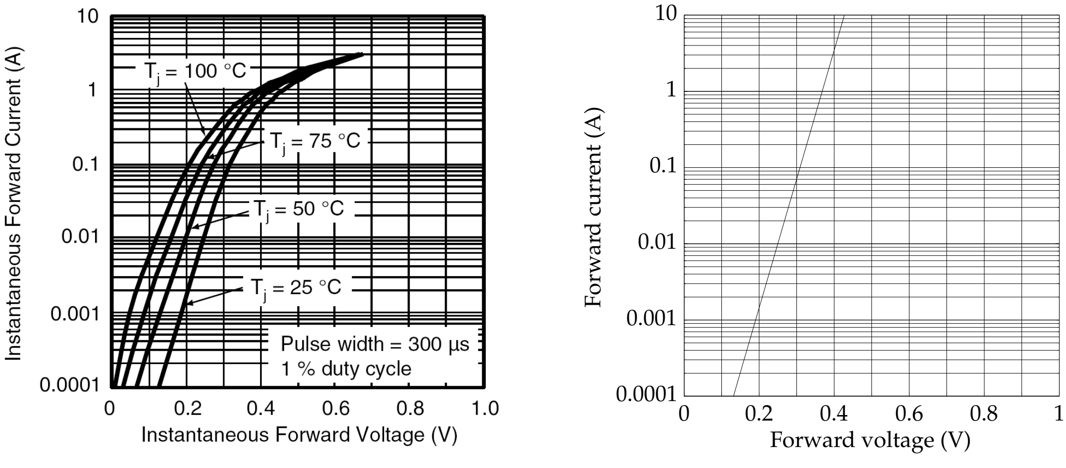

(a) Datasheet **(b)** Model

Figure 49. Comparison between (a) the forward *I-V* characteristics of a SL03 Schottky diode by Vishay as reported on the device datasheet [87], and (b) the plot of the i_D-v_D relationship modeled by Equation (29), with $n = 1$ and $I_S = 600\,\text{nA}$ as parameter values. For currents below 70 mA and junction temperatures around 25 °C, this model allows to accurately reproduce the behavior of the real device.

A.2 MODEL FITTING

The value of parameters n and I_S for a specific diode can be derived from the information provided by the device datasheet.

On the datasheet of diode devices it is very common to find a semi-log plot reporting the typical forward *I-V* characteristics of the diode for different junction temperatures, like the one shown in Figure 49a. It can be observed that each curve is linear up to a certain current value, and then it exhibits a saturation effect for higher currents, which is caused by the intrinsic series resistance of the device and by the high injection level [88]. The model provided by Equation (29) is valid for relatively low values of current density (which are those of interest in our application), and it is indeed suitable to describe the linear piece of the curve. This becomes clear by rewriting Equation (29) as

$$\ln\big(i_D(t) + I_S\big) \cong \ln i_D(t) = \frac{v_D(t)}{nV_t} + \ln I_S \quad \text{when } i_D(t) \gg I_S \tag{37}$$

which highlights that the logarithm of the forward current has a linear dependence on the forward voltage.

In order to estimate parameters n and I_S, it is sufficient to find the couple of values which enable to obtain the same graph (for the linear portion only) appearing on the datasheet once they are inserted in the previous equation. This can be easily accomplished with the help of a numerical computing environment such as Matlab, which allows to plot the i_D-v_D relationship on a semi-log graph with the same axes of the one on the datasheet, and to observe how a change in the value of a parameter graphically affects the position of the line on the chart. After a series of tries and subsequent adjustments, the couple of values for n and I_S which make the Matlab plot appearance identical to the linear portion of the datasheet characteristic, can be eventually spotted.

Figure 49 shows an application example of this parameter estimation methodology. The aim is to obtain the value of n and I_S for a SL03 Schottky diode by Vishay, when its junction temperature is around 25 °C. The typical forward I-V characteristics of this device as reported by its datasheet are shown in Figure 49a. Considering that the SL03 is a Schottky diode and that the currents of interest are in the range of milliamperes or tens of milliamperes, the value of the ideality factor n is expected to be 1, according to the physics of this device [88]. A Matlab script has been prepared to plot Equation (29) on a semi-log graph with the same axes of Figure 49a, considering $n = 1$ and arbitrary I_S. After some trials with different I_S values, the plot shown in Figure 49b was obtained using $I_S = 600\,\text{nA}$. This chart provides a perfect match with the linear portion of the I-V curve shown on the device datasheet for a junction temperature of 25 °C, and consequently values $n = 1$ and $I_S = 600\,\text{nA}$ can be considered to model the behavior of this specific diode.

Finally, it is important to remind that both Equation (15) and the parameter estimation methodology presented in this section build on the hypothesis that the forward I-V characteristic of the diode is described by Equation (29). For this reason, the results provided by Equation (15) are valid just as long as the forward current remains below the limit value beyond which this model starts losing accuracy (about 70 mA in the example above), and just as long as the junction temperature keeps close to the one considered during parameter estimation (25 °C in the example above).

BIBLIOGRAPHY

[1] Paul D. Mitcheson, Eric Morgan Yeatman, G. Kondala Rao, Andrew S. Holmes, and Timothy C. Green. "Energy Harvesting From Human and Machine Motion for Wireless Electronic Devices". In: *Proceedings of the IEEE* 96.9 (Sept. 2008), pp. 1457–1486 (cit. on pp. 7, 54, 77).

[2] Vehbi C. Gungor and Gerhard P. Hancke. "Industrial Wireless Sensor Networks: Challenges, Design Principles, and Technical Approaches". In: *IEEE Transactions on Industrial Electronics* 56.10 (Oct. 2009), pp. 4258–4265 (cit. on pp. 7, 39, 57).

[3] Thad E. Starner. "Human-powered wearable computing". In: *IBM Systems Journal* 35.3-4 (1996), pp. 618–629 (cit. on p. 8).

[4] Shad Roundy, Paul K. Wright, and Jan M. Rabaey. *Energy Scavenging for Wireless Sensor Networks. With Special Focus on Vibrations.* Boston (MA, USA): Kluwer Academic Publishers, 2003 (cit. on pp. 8, 80).

[5] Sujesha Sudevalayam and Purushottam Kulkarni. "Energy Harvesting Sensor Nodes: Survey and Implications". In: *IEEE Communications Surveys & Tutorials* 13.3 (2011), pp. 443–461 (cit. on p. 8).

[6] J. Ahola, T. Ahonen, V. Sarkimaki, A. Kosonen, et al. "Design Considerations for Current Transformer Based Energy Harvesting for Electronics Attached to Electric Motor". In: *Proc. 19th International Symposium on Power Electronics, Electrical Drives, Automation and Motion (SPEEDAM 2008).* June 2008, pp. 901–905 (cit. on p. 8).

[7] Pai H. Chou and Sehwan Kim. "Techniques for Maximizing Efficiency of Solar Energy Harvesting Systems". In: *Proc. 5th International Conference on Mobile Computing and Ubiquitous Networking (ICMU 2010).* Apr. 2010. (Cit. on p. 10).

[8] A. Khaligh, Peng Zeng, and Cong Zheng. "Kinetic Energy Harvesting Using Piezoelectric and Electromagnetic Technologies – State of the Art". In: *IEEE Transactions on Industrial Electronics* 57.3 (Mar. 2010), pp. 850–860 (cit. on p. 15).

[9] Lauric Garbuio, Mickaël Lallart, Daniel Guyomar, Claude Richard, and David Audigier. "Mechanical Energy Harvester With Ultralow Threshold Rectification Based on SSHI Nonlinear Technique". In: *IEEE Transactions on Industrial Electronics* 56.4 (Apr. 2009), pp. 1048–1056 (cit. on pp. 16, 40).

[10] A. Nasiri, S. A. Zabalawi, and G. Mandic. "Indoor Power Harvesting Using Photovoltaic Cells for Low-Power Applications". In: *IEEE Transactions on Industrial Electronics* 56.11 (Nov. 2009), pp. 4502–4509 (cit. on p. 16).

[11] Chunhua Liu, K. T. Chau, and Xiaodong Zhang. "An Efficient Wind-Photovoltaic Hybrid Generation System Using Doubly Excited Permanent-Magnet Brushless Machine". In: *IEEE Transactions on Industrial Electronics* 57.3 (Mar. 2010), pp. 831–839 (cit. on pp. 16, 80).

[12] Robert Myers, Mike Vickers, Hyeoungwoo Kim, and Shashank Priya. "Small scale windmill". In: *Applied Physics Letters* 90.5, 054106 (2007) (cit. on pp. 16, 18, 22, 24).

[13] Michael A. Weimer, Thurein S. Paing, and Regan A. Zane. "Remote area wind energy harvesting for low-power autonomous sensors". In: *Proc. 37th IEEE Power Electronics Specialists Conference (PESC 2006)*. June 2006, pp. 1–5 (cit. on pp. 16, 18, 22).

[14] Chulsung Park and Pai H. Chou. "AmbiMax: Autonomous Energy Harvesting Platform for Multi-Supply Wireless Sensor Nodes". In: *Proc. 3rd IEEE Communications Society on Sensor and Ad Hoc Communications and Networks (SECON 2006)*. Vol. 1. Sept. 2006, pp. 168–177 (cit. on pp. 16, 78, 80).

[15] *WindLab Junior webpage*. Jointiff Limited. URL: `http://jointiff.com/wind-turbines/windlab-junior/` (visited on 02/28/2013) (cit. on p. 16).

[16] Raul Morais, Samuel G. Matos, Miguel A. Fernandes, António L. G. Valente, et al. "Sun, wind and water flow as energy supply for small stationary data acquisition platforms". In: *Computers and Electronics in Agriculture* 64.2 (Dec. 2008), pp. 120–132 (cit. on pp. 16, 78, 80).

[17] *Introducing the microWindbelt*. Humdinger Wind Energy LLC, 2008. URL: `http://www.humdingerwind.com/pdf/microBelt_brief.pdf` (visited on 02/28/2013) (cit. on pp. 17, 24).

[18] Ahmadreza Tabesh and Luc G. Fréchette. “A Low-Power Stand-Alone Adaptive Circuit for Harvesting Energy From a Piezoelectric Micropower Generator”. In: *IEEE Transactions on Industrial Electronics* 57.3 (Mar. 2010), pp. 840–849 (cit. on pp. 17, 40).

[19] Denis Dondi, Alessandro Bertacchini, Davide Brunelli, Luca Larcher, and Luca Benini. “Modeling and Optimization of a Solar Energy Harvester System for Self-Powered Wireless Sensor Networks”. In: *IEEE Transactions on Industrial Electronics* 55.7 (July 2008), pp. 2759–2766 (cit. on p. 17).

[20] Geffrey K. Ottman, Heath F. Hofmann, A. C. Bhatt, and George A. Lesieutre. “Adaptive piezoelectric energy harvesting circuit for wireless remote power supply”. In: *IEEE Transactions on Power Electronics* 17.5 (Sept. 2002), pp. 669–676 (cit. on pp. 17, 18).

[21] Geffrey K. Ottman, Heath F. Hofmann, and George A. Lesieutre. “Optimized piezoelectric energy harvesting circuit using step-down converter in discontinuous conduction mode”. In: *IEEE Transactions on Power Electronics* 18.2 (Mar. 2003), pp. 696–703 (cit. on pp. 17, 18).

[22] Thurein S. Paing and Regan A. Zane. “Resistor Emulation Approach to Low-Power Energy Harvesting”. In: *Proc. 37th IEEE Power Electronics Specialists Conference (PESC 2006)*. June 2006, pp. 1–7 (cit. on pp. 18, 28, 29).

[23] Elie Lefeuvre, David Audigier, Claude Richard, and Daniel Guyomar. “Buck-Boost Converter for Sensorless Power Optimization of Piezoelectric Energy Harvester”. In: *IEEE Transactions on Power Electronics* 22.5 (Sept. 2007), pp. 2018–2025 (cit. on pp. 18, 28, 40, 43, 45).

[24] A. M. Rahimi and A. Emadi. “Discontinuous-Conduction Mode DC/DC Converters Feeding Constant-Power Loads”. In: *IEEE Transactions on Industrial Electronics* 57.4 (Apr. 2010), pp. 1318–1329 (cit. on p. 18).

[25] Arvindh Rajasekaran, Abhiman Hande, and Dinesh Bhatia. “Buck-boost converter based power conditioning circuit for low excitation vibrational energy harvesting”. In: *Proc. 3rd Austin Conference on Integrated Systems & Circuits (ACISC 2008)*. May 2008. (Cit. on pp. 18, 40, 43).

[26] David A. Howey, A. Bansal, and Andrew S. Holmes. “Design and performance of a centimetre-scale shrouded wind turbine

for energy harvesting”. In: *Smart Materials and Structures* 20.8, 085021 (2011) (cit. on pp. 22–24).

[27] C. C. Federspiel and J. Chen. “Air-powered sensor”. In: *Proc. 2nd IEEE International Conference on Sensors (SENSORS 2003)*. Vol. 1. Oct. 2003, pp. 22–25 (cit. on pp. 22, 24).

[28] Rodolfo Pallabazzer. *Sistemi eolici*. Soveria Mannelli (IT): Rubettino Editore, 2004 (cit. on pp. 23, 25).

[29] David Rancourt, Ahmadreza Tabesh, and Luc G. Fréchette. “Evaluation of Centimeter-Scale Micro Wind Mills: Aerodynamics and Electromagnetic Power Generation”. In: *Proc. 7th IEEE International Workshops on Micro and Nanotechnology for Power Generation and Energy Conversion Applications (PowerMEMS 2007)*. Nov. 2007, pp. 93–96. (Cit. on p. 24).

[30] F. J. Xu, F. G. Yuan, J. Z. Hu, and Y. P. Qiu. “Design of a miniature wind turbine for powering wireless sensors”. In: *Proceedings of SPIE* 7647, 764741 (Mar. 2010): *Sensors and Smart Structures Technologies for Civil, Mechanical, and Aerospace Systems 2010* (cit. on p. 24).

[31] Dibin Zhu, Stephen P. Beeby, M. John Tudor, Neil M. White, and Nick R. Harris. “A novel miniature wind generator for wireless sensing applications”. In: *Proc. 9th IEEE International Conference on Sensors (SENSORS 2010)*. Nov. 2010, pp. 1415–1418 (cit. on p. 24).

[32] Sebastian Pobering and Norbert Schwesinger. “Power supply for wireless sensor systems”. In: *Proc. 7th IEEE International Conference on Sensors (SENSORS 2008)*. Oct. 2008, pp. 685–688 (cit. on p. 24).

[33] D. St. Clair, A. Bibo, V. R. Sennakesavababu, M. F. Daqaq, and G. Li. “A scalable concept for micropower generation using flow-induced self-excited oscillations”. In: *Applied Physics Letters* 69.14, 144103 (2010) (cit. on p. 24).

[34] Marian K. Kazimierczuk. *Pulse-width Modulated DC–DC Power Converters*. Chichester (UK): John Wiley & Sons, Ltd, 2008 (cit. on p. 28).

[35] Robert W. Erickson and Dragan Maksimović. *Fundamentals of Power Electronics*. 2nd ed. New York (NY, USA): Springer Science+Business Media, 2001 (cit. on pp. 28, 42).

[36] *ICM7555, ICM7556 General Purpose Timers*. Datasheet. Intersil, Aug. 2006. URL: `http://www.intersil.com/data/fn/fn2867.pdf` (visited on 02/28/2013) (cit. on p. 35).

[37] Winston K. G. Seah, Zhi Ang Eu, and Hwee-Pink Tan. "Wireless sensor networks powered by ambient energy harvesting (WSN-HEAP)-Survey and challenges". In: *Proc. 1^{st} International Conference on Wireless Communication, Vehicular Technology, Information Theory and Aerospace & Electronic Systems Technology (Wireless VITAE 2009)*. IEEE, 2009, pp. 1–5 (cit. on p. 39).

[38] Mickaël Lallart, Daniel Guyomar, Yves Jayet, Lionel Petit, et al. "Synchronized switch harvesting applied to self-powered smart systems: Piezoactive microgenerators for autonomous wireless receivers". In: *Sensors and Actuators A: Physical* 147.1 (Sept. 2008), pp. 263–272 (cit. on p. 39).

[39] Kimberly Ann Cook-Chennault, Nithya Thambi, and A. M. Sastry. "Powering MEMS portable devices — a review of non-regenerative and regenerative power supply systems with special emphasis on piezoelectric energy harvesting systems". In: *Smart Materials and Structures* 17.4, 043001 (Aug. 2008) (cit. on p. 39).

[40] Stephen P. Beeby, M. John Tudor, and Neil M. White. "Energy harvesting vibration sources for microsystems applications". In: *Measurement Science and Technology* 17.12 (2006), R175–R195 (cit. on pp. 39, 54, 55).

[41] Alper Erturk and Daniel J. Inman. *Piezoelectric Energy Harvesting*. Chichester, UK: John Wiley & Sons, Ltd, 2011 (cit. on p. 39).

[42] Ning Wang, Naiqian Zhang, and Maohua Wang. "Wireless sensors in agriculture and food industry — Recent development and future perspective". In: *Computers and Electronics in Agriculture* 50.1 (2006), pp. 1–14 (cit. on p. 51).

[43] Luis Ruiz-Garcia, Loredana Lunadei, Pilar Barreiro, and Ignacio Robla. "A Review of Wireless Sensor Technologies and Applications in Agriculture and Food Industry: State of the Art and Current Trends". In: *Sensors* 9.6 (2009), pp. 4728–4750 (cit. on p. 51).

[44] Tae-Hwan Kang and Yutaka Kaizu. "Vibration analysis during grass harvesting according to ISO vibration standards". In: *Computers and Electronics in Agriculture* 79.2 (2011), pp. 226–235 (cit. on pp. 52, 54).

[45] Stefano Scorcioni, Alessandro Bertacchini, Denis Dondi, Luca Larcher, Paolo Pavan, and Gino Mainardi. "A vibration-powered wireless system to enhance safety in agricultural machin-

ery". In: *Proc. 37th Annual Conference of the IEEE Industrial Electronics Society (IECON 2011)*. Nov. 2011, pp. 3510–3515 (cit. on pp. 55, 56, 70).

[46] Gerhard Müller, Thomas Rittenschober, and Andreas Springer. "A wireless sensor network using energy harvesting for agricultural machinery". In: *Elektrotechnik und Informationstechnik* 127.3 (2010), pp. 39–46 (cit. on pp. 55, 57, 58, 70).

[47] Hsin-Mu Tsai, W. Viriyasitavat, O. K. Tonguz, C. Saraydar, T. Talty, and A. MacDonald. "Feasibility of In-car Wireless Sensor Networks: A Statistical Evaluation". In: *Proc. 4rd IEEE Communications Society on Sensor and Ad Hoc Communications and Networks (SECON 2007)*. June 2007, pp. 101–111 (cit. on p. 57).

[48] John G. Winterton. "Component identification of gear-generated spectra". In: *Orbit* (June 1991), pp. 11–14. (Cit. on p. 60).

[49] *PMG17 Vibration Energy Harvester*. Technical Datasheet. Perpetuum Ltd, May 2010. URL: `http://www.perpetuum.com/resources/PMG17%20Datasheet.pdf` (visited on 02/28/2013) (cit. on p. 64).

[50] ISO TC 23/SC 2. "Agricultural wheeled tractors and field machinery — Measurement of whole-body vibration of the operator". International Standard ISO 5008:2002. Geneva, Switzerland: International Organization for Standardization, 2002. (Cit. on p. 65).

[51] *P-876 DuraAct Patch Transducer*. Technical Datasheet. PI Ceramic GmbH, June 2012. URL: `http://www.piceramic.com/datasheet/P876_Datasheet.pdf` (visited on 02/28/2013) (cit. on p. 66).

[52] Birgit Schulze. *Energy Harvesting Uses the Piezo Effect. DuraAct Piezo Transducer Plus Matching Electronics*. White paper. PI Ceramic GmbH. July 2011. URL: `http://piceramic.com/download/Energy_Harvesting.pdf` (visited on 02/28/2013) (cit. on pp. 67, 68).

[53] Denis Dondi, Alessandro Bertacchini, Stefano Scorcioni, Luca Larcher, and Paolo Pavan. "Enhancing Safety in Vehicles with Implement or Trailer using an Autonomous Wireless Sensor Network System". In: *IEEE International Conference on Vehicular Electronics and Safety (ICVES 2012)*. July 2012, pp. 234–240 (cit. on pp. 70, 71).

[54] Davide Bruni, Luca Benini, and Bruno Riccò. "System lifetime extension by battery management: An experimental work". In: *Proc. CASES'02*. Oct. 2002, pp. 232–237 (cit. on pp. 77, 78).

[55] Alexander S. Weddel, Michele Magno, Geoff V. Merret, Davide Brunelli, Bashir M. Al-Hashimi, and Luca Benini. "A Survey of Multi-Source Energy Harvesting Systems". In: *Proc. Design, Automation and Test in Europe (DATE 2013)*. Mar. 2013. (Cit. on p. 78).

[56] S. Saggini and P. Mattavelli. "Power management in multi-source multi-load energy harvesting systems". In: *Proc. 13th European Conference on Power Electronics and Applications (EPE 2009)*. Sept. 2009, pp. 1–10. (Cit. on p. 78).

[57] Chien-Ying Chen and Pai H. Chou. "DuraCap: a Supercapacitor-Based, Power-Bootstrapping, Maximum Power Point Tracking Energy-Harvesting System". In: *Proc. International Symposium on Low Power Electronics and Design (ISLPED 2010)*. Aug. 2010. (Cit. on p. 78).

[58] *EH-Link™ Technical Product Overview*. MicroStrain Inc. 2009. URL: `http://www.microstrain.com/energy-harvesting/eh-link` (visited on 02/28/2013) (cit. on p. 79).

[59] Davide Brunelli, Clemens Moser, Lothar Thiele, and Luca Benini. "Design of a Solar-Harvesting Circuit for Batteryless Embedded Systems". In: *IEEE Transactions on Circuits and Systems—Part I: Regular Papers* 56.11 (Nov. 2009), pp. 2519–2528 (cit. on pp. 80, 84).

[60] Davide Brunelli, Denis Dondi, Alessandro Bertacchini, Luca Larcher, Paolo Pavan, and Luca Benini. "Photovoltaic scavenging systems: Modeling and optimization". In: *Microelectronics Journal* 90.9 (2008), pp. 1337–1344 (cit. on p. 80).

[61] Martin Patoka. *Fundamentals of power system ORing*. Texas Instruments. Mar. 2007. URL: `http://www.eetimes.com/design/power-management-design/4012155/Fundamentals-of-power-system-ORing` (visited on 02/28/2013) (cit. on p. 83).

[62] *Meteorological data gathered during the Grand-St-Bernard Deployment*. SensorScope. 2007. URL: `http://lcav.epfl.ch/page-86035-en.html` (visited on 02/28/2013) (cit. on p. 87).

[63] Bruno Lapillonne, Carine Sebi, and Karine Pollier. "Energy efficiency trends for households in the EU-27". Tech. rep. Enerdata for the ODYSSEE-MURE project, Mar. 2012. (Cit. on p. 89).

[64] Nikolaos Roubanis, Carola Dahlström, and Patricia Noizette. "Renewable energy statistics". In: *Statistics in focus – Eurostat* 56 (Nov. 2010), pp. 1–8. (Cit. on p. 89).

[65] Karl Ochsner. "Heat pump benefits". Presentation at the *Dinner Debate in the European Parliament* held in Brussels (BE) on Nov. 9th, 2009. URL: `http://www.ehpa.org/uploads/media/20091109_Pres_Benefits_HP_technology_Energy_savings_climate_goals_EN_20091109_OCK_EHPA_Dinner_debate.pdf` (visited on 02/28/2013) (cit. on p. 90).

[66] *Electricity production by fuel (ENER 027) – Assessment*. European Environment Agency. Apr. 2012. URL: `http://www.eea.europa.eu/data-and-maps/indicators/electricity-production-by-fuel-1/ds_resolveuid/7f23f82b-353c-4a63-94aa-e0b9b410a27d` (visited on 02/28/2013) (cit. on p. 90).

[67] G. Manfroi, M. Maistrello, and L.C. Tagliabue. "Synergy of geothermal heat pumps and PV plant for buildings block". In: *Proc. International Conference on Clean Electrical Power (ICCEP 2011)*. June 2011, pp. 466–473 (cit. on p. 90).

[68] "Libro Bianco sulle Pompe di Calore". Italian. White paper. Gruppo Italiano Pompe di Calore, Mar. 2010. (Cit. on p. 90).

[69] G. M. S. Islam, A. Al-Durra, S. M. Muyeen, and J. Tamura. "Low voltage ride through capability enhancement of grid connected large scale photovoltaic system". In: *Proc. 37th Annual Conference of the IEEE Industrial Electronics Society (IECON 2011)*. Nov. 2011, pp. 884–889 (cit. on p. 90).

[70] Tomoki Ehara. "Overcoming PV grid issues in urban areas". Tech. rep. IEA-PVPS T10-06:2009. Mizuho Information & Research Institute for the Photovoltaic Power Systems Programme of the International Energy Agency (IEA PVPS), Oct. 2009. (Cit. on p. 90).

[71] Ulrich Boeke, Matthias Wendt, and Lennart Yseboodt. "Combined Solar and AC Mains Powered LED Lighting System". In: *Proc. 14th European Conference on Power Electronics and Applications (EPE 2011)*. Sept. 2011, pp. 1–8. (Cit. on p. 91).

[72] SMA Solar Technology AG. *Increased Self-Consumption – Sunny Backup / Sunny Home Manager*. SBU_HoMan-PL-UEN123013 Version 1.3. Planning Guidelines. 2012. URL: `http://files.sma.de/dl/4720/SBU_HoMan-PL-UEN123013.pdf` (visited on 02/28/2013) (cit. on pp. 91, 92).

[73] Michael Bragard, Nils Soltau, Stephan Thomas, and Rik W. De Doncker. "The Balance of Renewable Sources and User Demands in Grids: Power Electronics for Modular Battery Energy Storage Systems". In: *IEEE Transactions on Power Electronics* 25.12 (Dec. 2010), pp. 3049–3056 (cit. on p. 93).

[74] Manfred Dittmer, Armin U. Schmiegel, Jean-François Cousseau, and Michael Lippert. "Demand Driven Integrated PV-System with Lithium-Ion Batteries for Storage to Boost Self Consumption". In: *Proc. 24th European Photovoltaic Solar Energy Conference (EU PVSEC 2009)*. 2009, pp. 3280–3284 (cit. on p. 93).

[75] Nico Kreutzer. "Self-Supply System Based On PV". Presentation at the *IEC SMB SG4 Workshop on LVDC*, held in Dresden (DE) in Sept. 2011. URL: `http://www.vde.com/en/dke/dkework/newsfromthecommittees/2011/documents/1%204.pdf` (visited on 02/28/2013) (cit. on p. 93).

[76] Jochen Hauff and Dennis Rendschmidt. "Enabling the European consumer to generate power for self-consumption". Tech. rep. A. T. Kearney Berlin for SunEdison LLC, 2011. (Cit. on p. 93).

[77] Mark Bost, Bernd Hirschl, and Astrid Aretz. "Effects of self-consumption and grid parity of photovoltaic systems". German. Tech. rep. Berlin (DE): Institute for Ecological Economy Research (IÖW), 2011. (Cit. on p. 93).

[78] Hirofumi Matsuo, Wenzhong Lin, Fujio Kurokawa, Tetsuro Shigemizu, and Nobuya Watanabe. "Characteristics of the multiple-input DC-DC converter". In: *IEEE Transactions on Industrial Electronics* 51.3 (June 2004), pp. 625–631 (cit. on p. 96).

[79] Ionel Dan Jitaru. "High efficiency flyback converter using synchronous rectification". In: *Proc. 17th Annual IEEE Applied Power Electronics Conference and Exposition (APEC 2002)*. Vol. 2. Mar. 2002, pp. 867–871 (cit. on p. 96).

[80] Kimiyoshi Kobayashi, Hirofumi Matsuo, and Yutaka Sekine. "Novel Solar-Cell Power Supply System Using a Multiple-Input DC–DC Converter". In: *IEEE Transactions on Industrial Electronics* 53.1 (Feb. 2006), pp. 281–286 (cit. on p. 96).

[81] Michele Bottarelli and Laura Gabrielli. "Payback Period for a Ground-Source Heat Pump System". In: *International Journal of Heat and Technology* 29.2 (2011), pp. 145–150. (Cit. on p. 99).

[82] Deutsche Gesellschaft für Sonnenergie (DGS). *Planning and Installing Photovoltaic Systems. A Guide for Installers, Architects and Engineers*. 2nd ed. London (UK): Earthscan, 2008 (cit. on p. 103).

[83] Simon Roberts and Nicolò Guariento. *Building Integrated Photovoltaics. A Handbook*. Basel (CH): Birkhäuser Verlag, 2009 (cit. on p. 103).

[84] David Banks. *An Introduction to Thermogeology. Ground Source Heating and Cooling*. 2nd ed. Chichester (UK): Wiley-Blackwell, 2012 (cit. on p. 104).

[85] Ayon M. Shahed and Stephen J. Harrison. "Preliminary Review of Geothermal Solar Assisted Heat Pumps". In: *Proc. 4th Canadian Solar Buildings Conference*. June 2009. (Cit. on p. 104).

[86] Adel S. Sedra and Kenneth C. Smith. *Microelectronic circuits*. 4th ed. New York (NY, USA): Oxford University Press, 1998 (cit. on p. 109).

[87] *SL02, SL03, SL04 Schottky Rectifier Surface Mount*. Datasheet. Vishay Semiconductors, Aug. 2011. URL: `http://www.vishay.com/docs/85687/sl02.pdf` (visited on 02/28/2013) (cit. on p. 112).

[88] Simon Min Sze. *Semiconductor Devices: Physics and Technology*. New York (NY, USA): John Wiley & Sons, 1985. (Cit. on pp. 112, 113).

AUTHOR'S PUBLICATIONS

PROCEEDINGS OF INTERNATIONAL CONFERENCES

[C1] Davide Carli, Davide Brunelli, Davide Bertozzi, and Luca Benini. "A High-Efficiency Wind-Flow Energy Harvester Using Micro Turbine". In: *Proc. 20th International Symposium on Power Electronics, Electrical Drives, Automation and Motion (SPEEDAM 2010)*. (Pisa, IT). June 2010, pp. 778–783 (cit. on pp. 22, 24).

[C2] Davide Carli, Davide Brunelli, Luca Benini, and Massimiliano Ruggeri. "An Effective Multi-Source Energy Harvester for Low Power Applications". In: *Proc. Design, Automation and Test in Europe (DATE 2011)*. (Grenoble, FR). Mar. 2011.

[C3] Davide Carli, Marco Cerigato, and Massimiliano Ruggeri. "Improved Piezoceramic Energy Harvesting Circuit for Self-Powered Wireless Sensor Nodes". In: *Proc. 3rd IEEE International Conference on Microwaves, Communications, Antennas and Electronic Systems (COMCAS 2011)*. (Tel-Aviv, IL). Nov. 2011.

[C4] Davide Carli, Denis Dondi, Alessandro Bertacchini, Luca Larcher, and Massimiliano Ruggeri. "Self Powered Wireless Sensors for Chassis, Powertrain, Working Equipment and Trailed Implements". In: *Proc. 12th European Regional Conference of the International Society for Terrain-Vehicle Systems (ISTVS)*. (Pretoria, ZA). Sept. 2012.

[C5] Davide Carli, Massimiliano Ruggeri, Michele Bottarelli, and Massimo Mazzer. "Grid-Assisted Photovoltaic Power Supply to Improve Self-Sustainability of Ground-Source Heat Pump Systems". In: *Proc. IEEE International Conference on Industrial Technology (ICIT 2013)*. (Cape Town, ZA). Feb. 2013.

Under peer review

[C6] Davide Carli, Massimiliano Ruggeri, Michele Bottarelli, and Massimo Mazzer. "Photovoltaic Power Supply Enhancing Self-Consumption for Autonomous Ground-Source Heat Pump Systems". Provisionally accepted for the inclusion in the program of the *4th International Conference on Clean Electrical Power (ICCEP 2013)*, which will be held in Alghero (IT) in June 2013.

INVITED SPEECHES AT INTERNATIONAL SEMINARS

[S1] Davide Carli, Massimiliano Ruggeri, and Massimo Mazzer. "Microgenerator Integration — A Step Closer to Self-Sustainable Ground-Source Heat Pump Systems". Speech at the international seminar *Ground-Source Heat Pump Systems*, held in Ferrara (IT) on Jan. 17th, 2012.

WORKING PAPERS

[W1] Davide Carli, Davide Brunelli, and Luca Benini. "A High-Efficiency Wind Energy Harvester for Autonomous Embedded Systems". Submitted to *IEEE Transactions on Industrial Electronics*, to be resubmitted.